2011

Measurement of the Target-Normal Single-Spin Asymmetry A(n,y) in the Deep Inelastic Region from the Reaction Helium-3 (e,e')

Joseph M. Katich
College of William & Mary - Arts & Sciences

Measurement of the Target-Normal Single-Spin Asymmetry A_y^n in the Deep Inelastic Region from the Reaction $^3\mathrm{He}^\uparrow(e,e')$

Joseph M. Katich

Williamsburg, Virginia

Master of Science, College of William and Mary, 2005
Bachelor of Science, Westminster College, 2003

A Dissertation presented to the Graduate Faculty
of the College of William and Mary in Candidacy for the Degree of
Doctor of Philosophy

Department of Physics

The College of William and Mary
January 2011

APPROVAL PAGE

This Dissertation is submitted in partial fulfillment of
the requirements for the degree of

Doctor of Philosophy

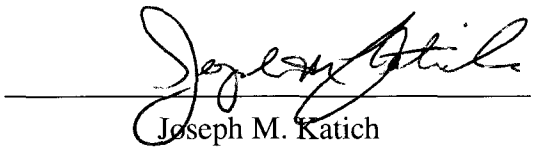

Joseph M. Katich

Approved by the Committee, September 2010

Committee Chair
Professor Todd Averett, Physics
The College of William & Mary

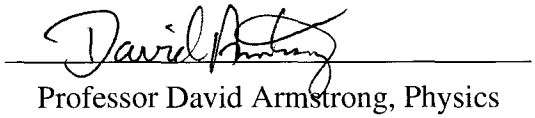

Professor David Armstrong, Physics
The College of William & Mary

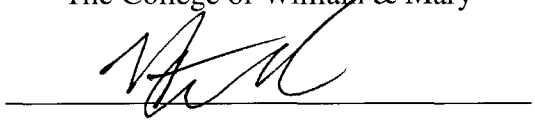

Assistant Professor William Detmold, Physics
The College of William & Mary

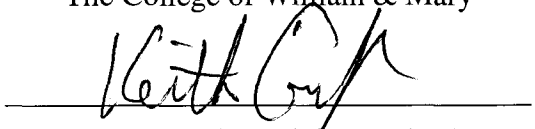

Professor Keith Griffioen, Physics
The College of William & Mary

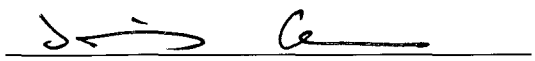

Dr. Jian-Ping Chen, Hall A Staff Scientist
Thomas Jefferson National Accelerator Facility

ABSTRACT PAGE

A first measurement of the inclusive target single-spin asymmetry, A_y^n, has been performed in deep-inelastic scattering of electrons from a ^{3}He target polarized normal to the electron scattering plane. This asymmetry is void of contributions at the Born level, and thus is a direct observable for two-photon physics. The experiment was performed in Hall A at Thomas Jefferson National Accelerator Facility from October 2008 through early February 2009.

The measurement is the first from a polarized neutron target. The final overall precision is several times better than previously existing SLAC proton data, and significantly extends the kinematic range over which the asymmetry has been measured. The asymmetry was measured at five kinematic points in the deep inelastic scattering region covering $Q^2 = 1 - 3$ GeV^2 and $x_B = 0.16 - 0.41$. The asymmetry varied from 0.006 to 0.071 with a statistical precision at the 10^{-2} level.

TABLE OF CONTENTS

To my parents, Ron and Kathy
without whom, I never would have made it to graduate school

and to my wife, Rita
without whom, I never would have finished.

ACKNOWLEDGMENTS

First and foremost, my sincere gratitude must be expressed to my advisor and friend, Todd Averett. Throughout the entire journey towards my PhD, Todd has been a seemingly endless source of patient knowledge and encouragement. Todd's enthusiasm, sense of humor and green Helmoltz coils are what originally got me excited about this kind of physics. Even through the toughest of times in graduate school, Todd never failed in rejuvenating that excitement in me.

I also thank the rest of my W&M committee members - David Armstrong, Keith Griffioen and Will Detmold. Their efforts have made this document a success. I must also acknowledge two other faculty members: Carl Carlson has provided me with many hours of thought-provoking theoretical discussion without which this thesis would be lacking. The late Mike Finn was one of the most encouraging people I have met. His positive comments kept me going when I failed to believe in my ability. He is greatly missed. The secretarial staff at W&M is second to none, and for that I thank Paula Perry, Sylvia Stout and Carol Hankins.

Special thanks are in order to my 'JLab advisor', Jian-Ping Chen, who is an excellent role-model for any young scientist. His work ethic as well as his respect for the integrity of science is unsurpassed by anyone I have met. Spokesmen Tim Holmstrom and Xiaodong Jiang have also played a large role in both the success of E07-013 and my completion of this thesis.

Many thanks are due to the entire E07-013 collaboration, in particular, my fellow graduate students, Kalyan Allada, Chiranjib Dutta, Jin Huang, Xin Qian, Youcai Wang and Yi Zhang. While any graduate student has control over their choice of advisor, none can chose the many graduate students that they collaborate with. I consider myself extremely fortunate to have ended up working with such an intelligent, dedicated group of students.

So many folks in the Hall A collaboration were instrumental in making E07-013 a success. Thanks to Kees de Jager for his support of the ^{3}He program and Bob Michaels for dedicating numerous hours of his time to teaching me the luminosity monitor DAQ. The entire Hall A technical staff was a pleasure to work with. I am lucky to have met Ed Foltz, Todd Ewing, Heidi Fansler, Jack Segal and Scot Spiegel, all of whom did an incredible job in the hall. I would like to thank Al Gavalya, Joyce Miller and Susan Esp for target design meetings that were enlightening, enjoyable and full of chocolate candy.

There are a few young scientists that I must thank for the countless hours they selflessly spent passing on their knowledge to me. Aidan Kelleher and Yi Qiang have taught me so much about the ^{3}He target. Vince Sulkosky got me started with data analysis and showed me how to use the Hall A analyzer. Bryan Moffit taught me nearly everything I know about programming. At times I would approach these people with so many questions that I'm embarrassed to think of how annoying I was. And yet, each of these people patiently answered every single question with a smile.

To all of the wonderful friends that I have met here in Williamsburg over the years, thank you for sharing great times with me. It would have been impossible to get to the end of graduate school without all of the long lunches, flag-football touchdown celebrations and Green Leafe pitchers. One of the hardest parts of graduate school is making the greatest friends you've had, only to have everyone move away at the end. May we all keep in touch.

To attempt to put into words the love that my family has provided throughout graduate school is futile. But still I try. I have been given unwavering support from my parents, despite how hard it is for them to have me so far from home. They are my heros. My siblings have remained as close to me as they ever have been, despite only seeing them a few times per year. They are my best friends. I cannot have a single conversation with my grandparents without them telling me how proud they are of what I am doing. This has gotten me through many tough times. My new family, the Schneiders, have treated me as their own son and brother. I will greatly miss my father-in-law, Leo.

Finally, to my wife, Rita - thank you. You have given me unconditional love, support and encouragement every day. You have motivated me to succeed. You have reminded me of my accomplishments when I was down, and reminded me to graduate when I was too proud. You are the best part of these past seven years. When I started all of this, it was for me. Now, I do it all for you.

LIST OF TABLES

LIST OF FIGURES

MEASUREMENT OF THE TARGET-NORMAL SINGLE-SPIN ASYMMETRY A_y^n IN THE DEEP INELASTIC REGION FROM THE REACTION $^3\mathrm{He}^\uparrow(e,e')$

CHAPTER 1

An Introduction to Nuclear Physics

1.1 The Birth of Nuclear Physics

It is widely accepted that the very first *nuclear* scattering experiment was performed in 1910 by Ernest Rutherford at Manchester University [1]. Rutherford's goal was to study the atom by scattering alpha particles from a piece of gold foil, then detect the scattered alpha particle (Figure 1.1). At this point in time, the existence of electrons, as well as negative and positive charge in the atom, were well known. However, the picture of the atom was that of J.J. Thomson's 'plum pudding' model [2], where negative electrons were embedded in a positively charged clump of matter, with the positive charge being evenly spread out over the entire clump (Figure 1.2). With this understanding of the atom, Rutherford expected the scattering alpha particles to experience only the slightest of deflections as it passed through the gold foil. Indeed, many of the alpha particles were only mildly deflected. What came as a shock was that a very small fraction of the particles would scatter through a very large angle - some even directly back toward the

alpha source. It was as if they had struck a concentration of positive charge so massive that they were repelled back in the direction from which they came. This was the discovery of the nucleus. From these results, Rutherford would propose an entirely new picture of the atom, which consisted of a tiny, yet massive positively charged nucleus that was orbited by several (even smaller) negatively charged electrons, much like a tiny solar system. The atom was made up almost entirely of empty space. While there are flaws with this picture, it was a huge step forward from the previous one, and quite possibly remains the most significant result of any single scattering experiment.

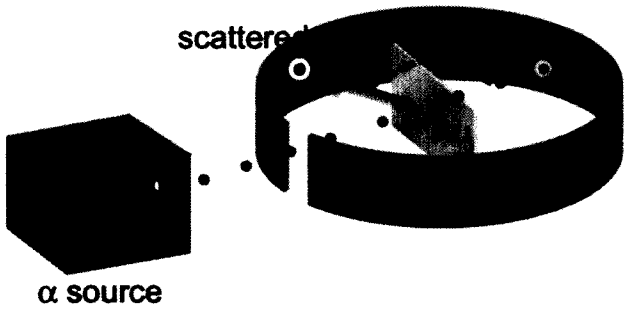

FIG. 1.1: Rutherford's gold foil experiment.

Rutherford's results triggered the beginning of an entire field of physics - the study of the structure of the atomic nucleus. Rutherford continued his investigation of the nucleus, scattering alpha particles from a number of other elements. He recognized that the one common link in all of this scattering was the emission of hydrogen nuclei [3]. This led him to postulate that the positive charge within *any* nucleus could be pieced together with an integer number of hydrogen nuclei. The term 'proton' was given to the nucleus of hydrogen, and physics had its first nucleon.

Seemingly, one could now describe any known atom simply by introducing more and

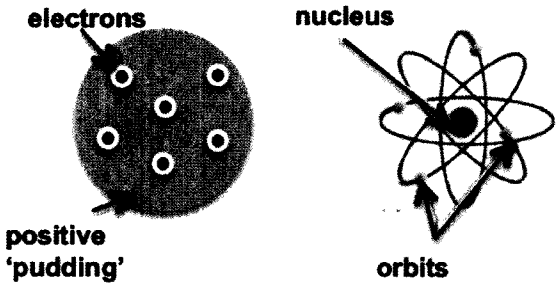

FIG. 1.2: Early atomic pictures: J.J. Thomson's 'plum pudding' model (left) and Rutherford's orbiting model (right).

more protons to the nucleus. These protons would account for all of the atom's positive charge, and most of its mass (sans the tiny electron masses). If a hydrogen atom has one proton, one unit of positive charge and one unit of mass, then a helium atom would have two protons, two units of positive charge and two units of mass. While the addition of proton charge proved correct, the mass calculation did not. This lead Rutherford to postulate the existence of yet another nucleon - the 'neutron', which would account for the missing mass of more complicated atoms. Finally, in 1932 James Chadwick verified the existence of this particle [4].

The discovery of the proton and neutron gave science something very close to the picture of the nucleus that we have today. However, a disturbing conundrum remained: how could so many protons of positive charge remain so close together without repelling each other apart via the electromagnetic force? Apparently there existed another force - one much stronger than the electromagnetic one - that bound them together. Aside from its enormous strength, it would also have to act only over very short distances, otherwise it would have been evident on a larger scale. This was the advent of the 'strong' force - one of the four fundamental forces in the universe (gravity, electromagnetic, strong and weak). Hideki Yukawa was the first to propose a theory of the strong force. He concluded

that, due to the short range of the force, it must be mediated by something very massive. His calculations put its mass somewhere between the electron and proton, thus naming it the 'meson' (for "middle"). Just a few years later, mesons were detected for the first time experimentally.

Again, it seemed as though the picture of subatomic physics was nearing completion. Atoms were made of protons, neutrons and electrons. The protons and neutrons made up the tiny nucleus via the strong force, while the electrons orbited around it due to the electromagnetic force. Could these be the elementary building blocks of the world around us? The rather quick discovery of several other particles would lead to a resounding 'no'. In fact, so many new particles were discovered that it became disturbingly complicated to think that they could all be 'elementary' particles. In 1964, Murray Gell-Mann and George Zweig both independently came up with the idea of quarks - elementary particles that bind together via the strong force to form the growing list of particles that were being seen in labs. It is now believed that the quarks, along with leptons (the electron, muon, tau and neutrinos) are the true fundamental constituents of the universe.

One final piece is needed to make the list complete: all of the four fundamental forces must somehow be communicated between interacting particles. Werner Heisenberg first proposed that electrons and protons communicated the electromagnetic (EM) force by bouncing photons of light between them [5]. All of this occurred on an extremely short time scale, meaning these 'exchange' photons could not be detected. Hence, they were termed 'virtual' photons. This is the basis of what is called Quantum Electrodynamics (QED), which describes all electromagnetic interactions.

Each fundamental force is associated with its own exchange particle which is analogous to the photon. The weak force is transmitted by charged $W^{+(-)}$ or neutral Z^0 bosons and the strong force by gluons. Gravity is mediated by the graviton, which has yet to be

detected. All of these interactions occur with some probability, and the goal of science is to be able to predict how and when these interactions will happen. Richard Feynman became famous for formulating a simple visual method for calculating the probability of different types of interactions, now called 'Feynman Diagrams'.

1.2 Cross Sections and Feynman Diagrams

The goal of physics, regardless of the subdivision, is to develop the theoretical framework to predict the outcome of an experiment, given some set of initial conditions. In scattering experiments, this can be posed as the following question: If a particle of mass m and energy E_1 passes through area $d\sigma$, what is the probability that, through interaction with a target particle (of mass M and energy E_2), it then scatters through solid angle $d\Omega$?

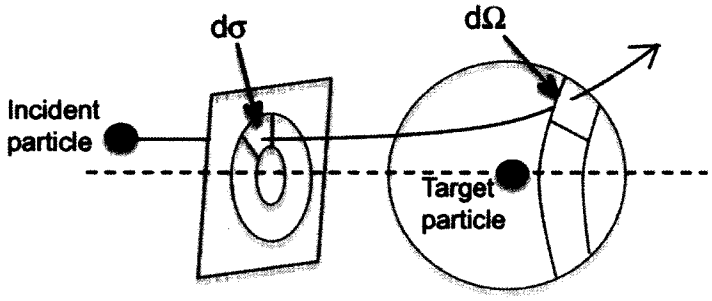

FIG. 1.3: Scattering area $d\sigma$ and solid angle $d\Omega$

This depends on several factors, for example, the type of incident and target particle involved and the interaction potentials. The ratio $d\sigma/d\Omega$ is called the 'differential cross-section' for the reaction, and is related to the likelihood of the occurrence mentioned above. In the case of Rutherford, the cross-section can be calculated classically for an

electron and nucleus of charge Ze and is easily shown to be [6]

$$\left(\frac{d\sigma}{d\Omega}\right)_{\text{Ruth}} = \left(\frac{Z\alpha}{4E\ \sin^2\left(\frac{\theta}{2}\right)}\right)^2$$

where Z is the number of protons in the nucleus, α is the fine structure constant and E is the incoming electron energy. While this formula was an excellent advancement in its time, it is lacking in that it is non-relativistic and neglects any sort of nuclear structure.

In general, calculation of the cross-section requires a robust method. Start by writing the cross-section in the form

$$\frac{d\sigma}{d\Omega} \propto |T_{fi}|^2 = |\mathcal{M}|^2 \cdot \Phi.$$

Here, T_{fi} represents the probability for a particle in initial state ϕ_i to scatter into final state ϕ_f, such that

$$T_{fi} = -i \int d^4x \phi_f^*(x) V(x) \phi_i(x) \tag{1.1}$$

and $V(x)$ is the interaction potential. $\mathcal{M}$ is called the 'matrix element' for the process, and Φ is a phase-space factor, which is nothing more than kinematic information. It is this matrix element that Richard Feynman gave us a beautifully simple way to calculate. He proposed that one can simply draw a 'stick figure' of the process, then associate certain pre-determined mathematical terms with each part of the diagram. For instance, two electrons which interact via the electromagnetic force could be represented as in Figure 1.4.

For this thesis, the diagram is read with time flowing from left to right. Each external

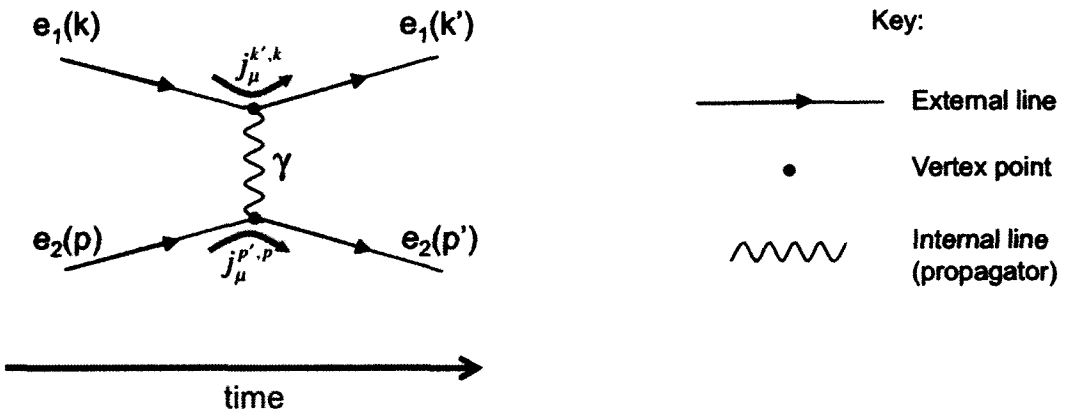

FIG. 1.4: A simple Feynman diagram representing electron-electron scattering. Here, 'k' and 'p' represent the kinematic properties of the particle.

line represents an incoming or outgoing electron. They are connected by an internal line, the exchange photon, which mediates their electromagnetic interaction (internal lines are called propagators). Forming the matrix element, $\mathcal{M}$, for this picture would consist of assigning a mathematical term to each external line, propagator and vertex. External lines would simply be represented by some wavefunction that describes that particle's initial and final state, $\phi_{1(2)} = u_{1(2)}(k)e^{-ip\cdot x}$. Propagators are described by their mass, spin and the momentum they carry away from an external line. The meat of the process is described at the vertices. which contain information about the strength of the interaction occurring - called the coupling constant. The matrix element can then be written in the form (lepton 1) $\times$ (propagator) $\times$ (lepton 2):

$$\begin{aligned}\mathcal{M} &= (\ell_1^{\text{in}} \cdot \text{vertex}_1 \cdot \ell_1^{\text{out}}) \times \text{propagator} \times (\ell_2^{\text{in}} \cdot \text{vertex}_2 \cdot \ell_2^{\text{out}}) \\ &= (-e_1 \bar{\phi}_1^{out} \cdot \gamma^\mu \cdot \phi_1^{in}) \times \left(\frac{i}{(k-k')^2}\right) \times (-e_2 \bar{\phi}_2^{out} \cdot \gamma^\mu \cdot \phi_2^{in}) \\ &= j_1^\mu \left(\frac{i}{(k-k')^2}\right) j_2^\mu\end{aligned} \tag{1.2}$$

where $j^{\mu}_{1(2)} = -e\bar{\phi}_{k'(p')}\gamma_{\mu}\phi_{k(p)}$ is called the 'current' of the electron. Using this current, the term T_{fi} in Equation 1.1 can be written

$$T_{fi} = -i \int j^{(1)}_{\mu}(x) \left(\frac{-1}{(k-k')^2} \right) j^{\mu}_{(2)} d^4x. \tag{1.3}$$

The square of the matrix element is written as

$$\left\langle |\mathcal{M}|^2 \right\rangle = \frac{e^4}{q^4} L^{\mu\nu}_{\mathrm{e}_1} L^{\mathrm{e}_2}_{\mu\nu}. \tag{1.4}$$

Here, $q = (k - k')$ is the 4-momentum transfered by the propagator from particle 1 to particle 2 and the L's are called the leptonic tensor [7]:

$$L^{\mu\nu}_{e_1} = \frac{1}{2} \sum_{\text{spins}} \left[\bar{u}_1(k)\gamma^{\mu}u_1(k') \right] \left[\bar{u}_1(k')\gamma^{\nu}u_1(k) \right]^*$$

$$= L^{S}_{\mu\nu}(k;k') + iL^{A}_{\mu\nu}(k,s;k') + L'^{S}_{\mu\nu}(k,s;k',s') + iL'^{A}_{\mu\nu}(k;k',s')$$

where S and A indicate symmetric and anti-symmetric tensor parts and s is spin.

The formalism which has been laid out describes the framework for calculating a cross-section. However, it is still rather general, and lacking in several ways. First, it describes only point particle scattering, which disallows the ability to calculate scattering of an electron from say, a proton. A calculation involving these particles requires a complete description of how its constituents are bound together, as well as how the virtual photon interacts with the collection of particles.

Introduction of particle structure leads to a second deficiency. Once a particle has structure, one must then ask, "At what level is the exchange photon interacting with the target?" With only a moderate amount of incident energy, the photon will distribute its

momentum amongst all constituents within the target, whereas a photon with large energy could interact with just a single constituent. The level at which the photon 'probes' the target as the energy spectrum is traversed is defined by several scattering regions.

Finally, the above assumes that particles interact solely via the exchange of a single mediator. This is incorrect. In fact, particles can and *do* communicate by the exchange of multiple mediating particles. Fortunately, the more internal photons that a Feynman diagram includes, the less significant it becomes to the overall cross-section.

1.3 Scattering from Particles with Structure

1.3.1 Elastic Scattering

Elastic scattering is defined as a process in which the same two particles that exist in the initial state also exist in the final state. In other words, the target particle is probed at the most superficial level, and no excitations occur. Momentum transfer of the photon is distributed amongst all constituents of the target. A Feynman diagram for elastic scattering is shown in Figure 1.5.

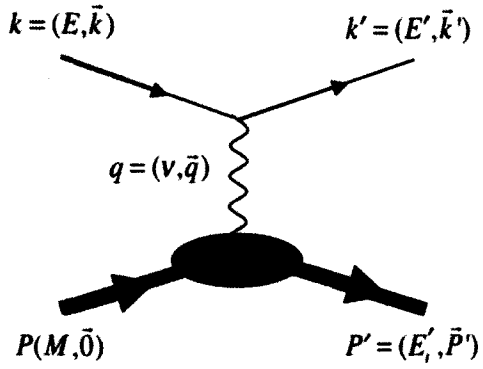

FIG. 1.5: Elastic scattering of an electron from a target with structure

Each of the terms $A = (E, \vec{A})$ represents the relativistic four-momentum of the particle in the laboratory frame. The masses of the electron and target are given by m and M, respectively. The process can be characterized by several kinematic variables:

- $Q^2 = -q^2 \approx 4EE'\sin^2\left(\frac{\theta}{2}\right)$ where $q = k - k'$ is called the 'virtuality' of the exchange photon, or simply the 4-momentum transfer squared. If the electron is viewed as a probe of nuclear structure, Q^2 describes the resolution of the probe.
- $\nu = E - E' = \frac{Q^2}{2M}$ is the energy transfered from the lepton to the target.
- $W = \sqrt{(P+q)^2} = \sqrt{M_T^2 + 2M_T\nu - Q^2}$ is the invariant mass of the residual hadronic system.
- $x = \frac{Q^2}{2P\cdot q} = \frac{Q^2}{2M\nu}$ is the Bjorken scaling variable (to be discussed later).
- $y = \frac{\vec{q}\cdot\vec{P}}{\vec{p}\cdot\vec{P}} = \frac{\nu}{E}$ is the fraction of lepton energy loss.

For elastic scattering, the energy of the outgoing electron is constrained by conserving initial and final four-momentum squared:

$$P'^2 = (k + P - k')^2$$

$$M^2 = M^2 + (E - E')^2 - E^2 - E'^2 + 2EE'\cos\theta + 2M(E - E')$$

$$E'(E + M - E\cos\theta) = ME$$

solving for E':

$$E' = \frac{E}{1 + \frac{E}{M}(1 - \cos\theta)} = \frac{E}{1 + \frac{2E}{M}\left(\sin^2\frac{\theta}{2}\right)}$$

Adding structure to the target makes writing down the matrix element much trickier, since there is no longer a simple vertex on the target side of the diagram. One needs the

appropriate 'hadronic current', J^{μ}, analogous to j^{μ} in Equation 1.2 in order to proceed. This is accomplished by replacing γ^{μ} by a more general form. It consists of two independent terms, γ^{μ} *and* $i\sigma^{\mu\nu}q_{\nu}$. Each of these terms will have coefficients that are functions of q^2:

$$\gamma^{\mu} \rightarrow \left[F_1(q^2)\gamma^{\mu} + \frac{\kappa}{2M}F_2(q^2)i\sigma^{\mu\nu}q_{\nu}\right]$$

Here, κ is the anomalous magnetic moment, $\sigma^{\mu\nu} = \frac{1}{2}i\left[\gamma^{\mu}, \gamma^{\nu}\right]$ and F_1 and F_2 are called Dirac form factors, which include all of the information to describe the structure of the target. The hadronic current can now be written as:

$$J^{\mu} = -e\bar{\psi}(p')\left[F_1(q^2)\gamma^{\mu} + \frac{\kappa}{2M}F_2(q^2)i\sigma^{\mu\nu}q_{\nu}\right]\psi(p) \tag{1.5}$$

and Equation 1.3 reflects this:

$$T_{fi} = -i\int j_{\mu}^{(1)}(x)\left(\frac{-1}{q^2}\right)J_{(2)}^{\mu}d^4x. \tag{1.6}$$

Finally, the cross-section for elastic scattering can be written as:

$$\frac{d\sigma}{d\Omega} = \frac{\alpha^2}{4E^2}\left(\frac{\cos^2\frac{\theta}{2}}{\sin^4\frac{\theta}{2}}\right)\frac{E'}{E}\left[\left(F_1^2 - \frac{\kappa^2q^2}{4M^2}F_2^2\right) - \frac{q^2}{2M^2}\left(F_1 + \kappa F_2\right)^2\tan^2\frac{\theta}{2}\right]$$

Everything outside of the square brackets is called the 'Mott' cross-section:

$$\left(\frac{d\sigma}{d_{\Omega}}\right)_{\text{Mott}} = \frac{\alpha^2}{4E^2}\left(\frac{\cos^2\frac{\theta}{2}}{\sin^4\frac{\theta}{2}}\right)\frac{E'}{E}$$

which is nothing more than Rutherford's cross-section, modified to include electron spin

(the 'cos' term), target recoil (E'/E) and relativity (simply by the use of four-vectors).

For elastic scattering, one typically uses the Sachs form factors, which describe the electric and magnetic distributions of the nucleon [7]:

$$G_E = F_1 + \frac{\kappa q^2}{4M^2} F_2$$

$$G_M = F_1 + \kappa F_2$$

and the cross-section for unpolarized elastic scattering (called the 'Rosenbluth' cross-section) can be written as:

$$\left(\frac{d\sigma}{d\Omega}\right)_{\text{Rosen}} = \left(\frac{d\sigma}{d\Omega}\right)_{\text{Mott}} \left(\frac{G_E^2 + \tau G_M^2}{1+\tau} + 2\tau G_M^2 \tan^2\frac{\theta}{2}\right) \tag{1.7}$$

in which $\tau = -\frac{q^2}{4M^2}$.

1.3.2 Quasi-Elastic Scattering

A simple approximation that can be used to describe the nucleus is a Fermi gas, such that it is a set of quasi-free nucleons bound in a potential. When the energy transfered, ν, is larger than this binding energy, the nucleus will not remain intact. The electron will be elastically scattered from one of the nucleons, ejecting it from the nucleus. Due to Fermi motion, the quasi-elastic peak is smeared about $\nu = Q^2/(2M)$ where M is the mass of the nucleon. Quasi-elastic scattering implies scattering from a nucleon *within* the target, thus there is no quasi-elastic peak when the target *is* a nucleon. The invariant mass, W, for quasi-elastic scattering has the same form as elastic scattering, with $M_T \rightarrow M_{nucleon}$.

1.3.3 Resonance Region Scattering

The resonant scattering region is the first which is considered 'inelastic'. As the energy and momentum transfer increase, quarks within the nucleons begin to absorb virtual photons. This can cause an excitation of the nucleon to a higher 'resonant' state. The existence of these states is clear evidence of structure within the nucleon. The resonance region is typically given as $1.0 < W < 2.0$ GeV/c^2. Further, for inelastic scattering, $W > M$ such that $2M\nu - Q^2 > 0$. It is at this point that Bjorken scaling is introduced as a means of describing the ratio of momentum transfer squared and energy transfer, $x = \frac{Q^2}{2M\nu}$. This variable describes the inelasticity of a process. Elastic scattering is defined as $x = 1$, regardless of whether that elastic scattering is from a nucleus, nucleon or a quark within the nucleon. Values of $x < 1$ describe inelastic scattering from the target.

1.3.4 Deep Inelastic Scattering

Deep inelastic scattering (DIS) is usually defined as $W > 2$ GeV/c^2 and $Q^2 > 1$ (GeV/c)^2. The virtual photon strikes a quark within the nucleon, which, at large Q^2, can be considered free. At this level individual resonances of the nucleon are no longer discernible, and scattering becomes an incoherent sum over all of the nucleon's constituents.

In inelastic scattering, one must consider *all* possible final hadronic states. Figure 1.6 shows a Feynman diagram representing inelastic scattering. The process is written

$$e(k) + N(P) \rightarrow e(k') + X(P')$$

where $X(P')$ includes all possible final states of the hadronic system (for inclusive scattering, these are undetected).

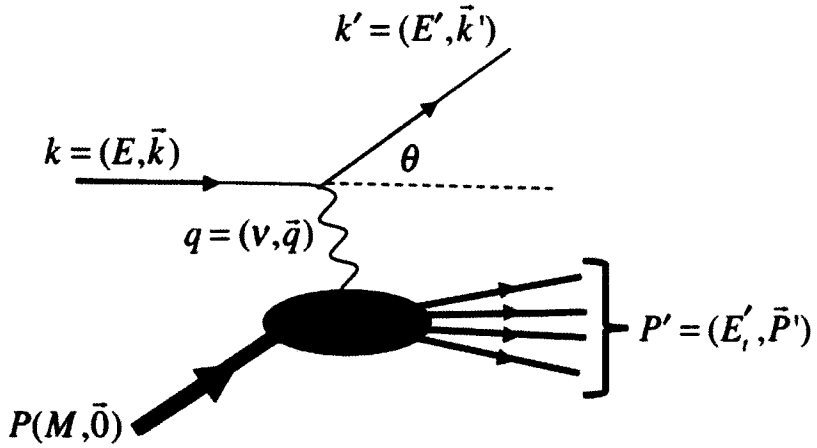

FIG. 1.6: An electron scattering from a nucleon, which has structure

Because the final state of the hadronic system is no longer well-defined, it cannot be represented by $\bar{\psi}(p')$ in Equation 1.5. This is remedied by writing the cross-section in the same form as 1.4, with the second leptonic tensor replaced by a hadronic tensor:

$$\frac{d\sigma}{d\Omega} \propto L_{\mu\nu} W^{\mu\nu} \tag{1.8}$$

and the goal now is to specify an appropriate form for $W^{\mu\nu}$. At this point, it will also be convenient to introduce the spin degree of freedom. This will allow for calculations that include a polarized target. The hadronic tensor which includes all possible states $X(P')$ is formally written as [8]:

$$W_{\mu\nu} = \frac{\pi^2}{M} \sum_X \langle N_s(P)|J_\mu(0)|X(P')\rangle\langle X(P')|J_\nu(0)|N_s(P)\rangle \cdot \delta(q + P - P'). \tag{1.9}$$

Using completeness of the state $|X\rangle$ gives:

$$W_{\mu\nu} = \frac{1}{4\pi M} \int d^4\zeta e^{iq\cdot\zeta} \langle N_s(P)|J_\mu(\zeta)J_\nu(0)|N_s(P)\rangle$$

where ζ is the spatial four-vector, s is the nucleon spin. The tensor can be decomposed into its symmetric and antisymmetric parts $W_{\mu\nu} = W^S_{\mu\nu} + W^A_{\mu\nu}$, which are given as [7]

$$W^S_{\mu\nu} = W_1\left(\nu, Q^2\right)\left(\frac{q_\mu q_\nu}{q^2} - g_{\mu\nu}\right) + \frac{W_2\left(\nu, Q^2\right)}{M^2}\left(P_\mu - \frac{P\cdot q}{q^2}q_\mu\right)\left(P_\nu - \frac{P\cdot q}{q^2}q_\nu\right)$$

and

$$W^A_{\mu\nu} = i\epsilon_{\mu\nu\alpha\beta}q^\alpha\left[G_1\left(\nu, Q^2\right)S^\beta + \frac{G_2\left(\nu, Q^2\right)}{M^2}\left(S^\beta P\cdot q - P^\beta S\cdot q\right)\right]$$

where $S^\mu = \bar{u}(P)\gamma^\mu\gamma_5 u(P)/2M$ is the hadronic spin vector. The functions W_1, W_2, G_1 and G_2 are called 'structure functions' and describe the internal structure of the hadron. They are commonly written as dimensionless functions which are dependent on Q^2 and x (defined above):

$$F_1(x, Q^2) = MW_1(\nu, Q^2)$$

$$F_2(x, Q^2) = \nu W_2(\nu, Q^2)$$

$$g_1(x, Q^2) = M\nu G_1(\nu, Q^2)$$

$$g_2(x, Q^2) = \nu^2 G_2(\nu, Q^2)$$

Notice that only the anti-symmetric part of the hadronic tensor is dependent on S^μ. Ergo, g_1 and g_2 are called 'spin structure functions' while F_1 and F_2 are 'spin-independent

structure functions'.

The cross-section for inclusive unpolarized DIS is written in terms of the structure functions F_1 and F_2 [7];

$$\frac{d^2\sigma}{d\Omega dE'} = \left(\frac{d\sigma}{d\Omega}\right)_{\text{Mott}} \left[\frac{1}{\nu}F_2(x,Q^2) + \frac{2}{M}2F_1(x,Q^2)\tan^2\frac{\theta}{2}\right]$$

In the case where the lepton and target are polarized, things are much more complicated. The cross-section also then depends on the angle, β, between the incident electron momentum ($\vec{k}$) and target spin ($\vec{S}$), as well as the angle between the outgoing electron momentum (k') and target spin, defined as $\cos\Theta = \sin\theta\sin\beta\cos\phi + \cos\theta\cos\beta$. Here, θ is the usual lab scattering angle defined by $k \times k'$ and ϕ is the angle between $\vec{k'}$ and $\vec{S}$.

Typical experimental values of β are $0°$ and $90°$. The former implies a target polarization that is parallel or anti-parallel to the incoming lepton momentum. This is called longitudinal polarization. The latter is referred to as transverse target polarization. Polarized cross-sections are functions of g_1 and g_2, and can be experimentally accessed by measuring the difference of scattering with target polarization $\vec{S}$ and $-\vec{S}$.

In the case where both the lepton and target are longitudinally polarized ($\beta = 0$ and $\Theta = \theta$), one has [9]

$$\frac{d^2\sigma_{\uparrow,\Uparrow}}{d\Omega dE'} - \frac{d^2\sigma_{\uparrow,\Downarrow}}{d\Omega dE'} = \frac{4\alpha^2 E'}{\nu E Q^2}\left[(E + E'\cos\theta)g_1(x,Q^2) - 2Mxg_2(x,Q^2)\right].$$

Here, a single-line arrow, $\uparrow$ ($\downarrow$), represents the lepton's spin direction and a double-line arrow, $\Uparrow$ ($\Downarrow$), is the orientation of target polarization. For a target that is polarized trans-

versely,

$$\frac{d^2\sigma_{\uparrow,\Rightarrow}}{d\Omega dE'} - \frac{d^2\sigma_{\uparrow,\Leftarrow}}{d\Omega dE'} = \frac{4\alpha^2 E'}{\nu E Q^2}\sin\theta \left[g_1(x,Q^2) + \frac{2ME}{\nu} g_2(x,Q^2) \right].$$

The case where both lepton and target spins are longitudinal is dominated by the g_1 term. When the target is transverse, the contributions of g_1 and g_2 are more evenly distributed.

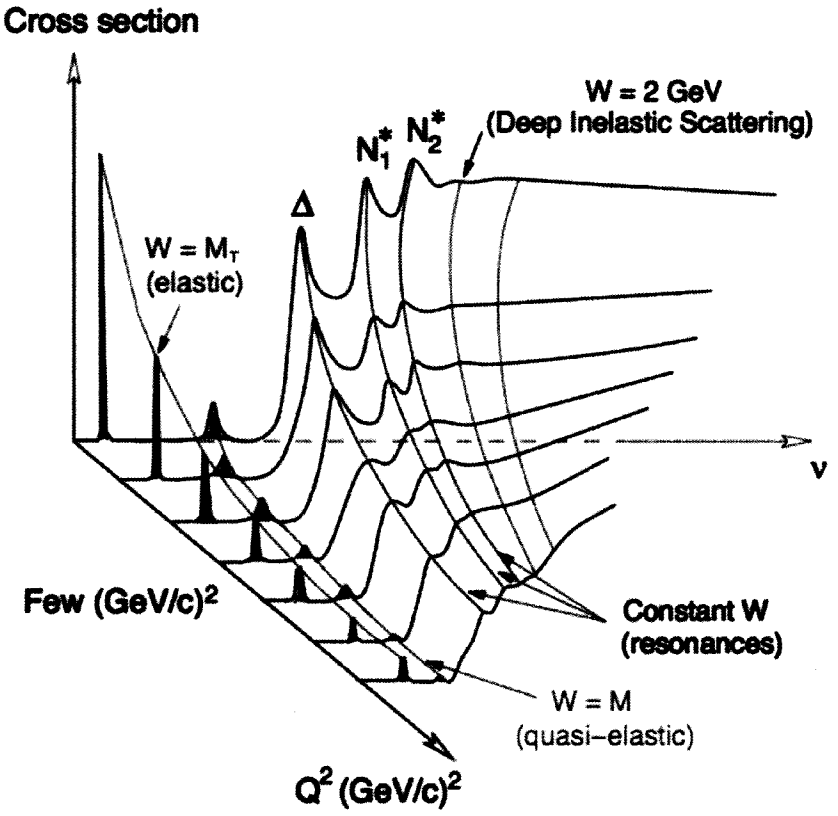

FIG. 1.7: Generic representation of the inclusive electron scattering cross-section as a function of both Q^2 and ν.

Regardless of scattering region, the cross-section has a clear dependence on the momentum and energy transfered from the electron to the target. As one traverses from one

end of the scattering regions to the other, the scattering cross-section evolves to reflect the level at which the target is being investigated (see Figure 1.7).

1.4 Operator Product Expansion and Twist

In 1969, Kenneth G. Wilson introduced the Operator Product Expansion (OPE) as a substitute for quantum field theory [10]. It is advantageous in that it provides model-independent QCD predictions for moments of structure functions via sum rules. This is achieved by separating the perturbative and non-perturbative parts of two operators. In the limit that $d \rightarrow 0$, the product of two operators can be written as

$$\lim_{d\rightarrow 0} \sigma_a(d)\sigma_b(0) = \sum_k C_{abk}(d)\sigma_k(0), \tag{1.10}$$

where C_{abk} are Wilson coefficients, which contain the perturbative part and can be calculated in QCD perturbatively. The operators σ_k contain the non-perturbative part and thus cannot be calculated in perturbative QCD. The formalism is used in DIS to develop a product of currents on a local operator basis. The contribution of these operators to the cross-section is of the order

$$x^{-n}\left(\frac{M}{Q}\right)^{\tau-2} \tag{1.11}$$

where $Q = \sqrt{Q^2}$ and $\tau = D - n$ is called the 'twist'. Here, D is the dimensionality (in powers of mass or momentum) of the operator and n is its spin. The lowest possible value for τ is twist-2. At large values of Q^2, higher twist terms are suppressed by increasing powers of $\frac{M}{Q}$. Theoretical predictions in Chapter 2 will relate the results of this thesis to

effects that are considered to be 'higher-twist'.

1.5 The Quark Parton Model of the Nucleon

The quark parton model (QPM) is an attempt to create a physical connection between the previously mentioned structure functions and the quark constituents that make up the nucleon. The key ingredient to the model is the assumption that at large Q^2 and ν, the viritual photon interacts incoherently with a collection of non-interacting ('free') constituent quarks. This assumption is valid so long as $Q^2 \gg M^2$, a condition that is true for DIS. This also implies a reference frame such that the transverse momentum of quarks within the nucleon go to zero. In this picture, the Bjorken variable x can be interpreted as the fraction of the nucleon's momentum that is carried by the quark which is struck by the virtual photon. An extremely interesting consequence of this "Bjorken limit" is that $Q^2 \to \infty$, $\nu \to \infty$ and $x \nrightarrow \infty$, the structure functions will only very weakly depend on Q^2, allowing them to be written as , $F_1(x)$, $F_2(x)$, $g_1(x)$ and $g_2(x)$. The structure functions can then be related to the probability of finding a parton carrying fraction x of the target's momentum [7]:

$$\begin{aligned} F_1(x) &= \frac{1}{2}\sum_f e_f^2 q_f(x) \\ F_2(x) &= \frac{1}{2}\sum_f x e_f^2 q_f(x) \end{aligned} \tag{1.12}$$

where $q(x)$ is called the unpolarized quark (parton) distribution function. Each term in the sum is weighted by the charge of the particular quark, e_f.

If one wishes to introduce spin-dependence to the QPM, the parton distribution func-

tions are redefined as:

$$\begin{aligned} q(x) &= q^{+}(x) + q^{-}(x) \\ \Delta q(x) &= q^{+}(x) - q^{-}(x) \end{aligned} \tag{1.13}$$

where $+$ and $-$ indicate helicity states in a longitudinally polarized nucleon. $q(x)$ is summed over all quark spins, and thus Equations 1.12 remain unchanged. The *polarized* structure function g_1 can be related to the helicity distribution function, $\Delta q(x)$ as:

$$g_1(x) = \frac{1}{2}\sum_f e_f^2 \Delta q_f(x)$$

The structure function g_2 is zero in the QPM since it describes the transverse spin of the quarks.

1.5.1 Transverse Momentum in the Nucleon

Since the momentum transfered to the target is never truly infinite, it is incorrect to totally neglect the possibility that the quarks have some non-zero transverse momentum, $\vec{p}_T$. At leading twist, there are eight different quark distribution functions that depend on $\vec{p}_T$. If one integrates over this momentum while enforcing time-reversal invariance, only three will survive (the first two of which were seen in Equation 1.13) [11]:

$$q(x) = \int d^2\vec{p}_T q(x, p_T^2) \tag{1.14}$$

$$\Delta q(x) = \int d^2\vec{p}_T \Delta q(x, p_T^2) \tag{1.15}$$

$$\delta q(x) = \int d^2\vec{p}_T \{h_{1T}^q + \frac{p_T^2}{2M} h_{1T}^{\perp q}(x, p_T^2)\} = \int d^2\vec{p}_T q(x, p_T^2) \tag{1.16}$$

The function $\delta q(x)$ is called the 'transversity' distribution function, as it describes the transverse momentum distribution of the quarks within the nucleon. If time-reversal invariance is *not* enforced, two more distribution functions will survive the integration over $\vec{p}_T$ [12]. These are both T-odd distribution functions, $f_{1T}^{\perp}$ ('Sivers function') and $h_1^{\perp}$ ('Boer-Mulders function'). The Sivers function gives the probability of finding a unpolarized quark within a transversely polarized nucleon. The Boer-Mulders function gives the probability of finding a transversely polarized quark within an unpolarized nucleon.

1.6 Higher Order Feynman Diagrams

Figure 1.4 shows the basic means by which two electrons can interact. However, one of the most important things that Feynman showed is that a process can not be represented by one diagram alone. In fact, there are an infinite number of diagrams needed to fully describe even the simple interaction of electron-electron scattering:

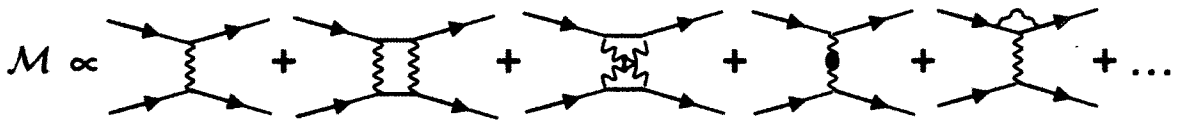

FIG. 1.8: The first five of an infinite number of Feynman diagrams that are needed to fully describe an electromagnetic scattering process.

This problem has a fortunate solution in Quantum Electrodynamics: the coupling constant corresponding to each photon is $\alpha \simeq 1/137$. This means that as the Feynman diagrams become more complicated (meaning more and more vertices are present), they also become less significant to the overall cross-section.

Obviously, if one wishes to use Feynman's calculus to calculate a cross-section, an appropriate cut-off must be made with regard to the number of diagrams to include. Quite typically, one will only use the very first diagram (called the lowest order diagram). This is sufficient in many instances, as the next-to-leading-order diagram includes an extra factor of alpha, and thus contributes at a level that is typically several orders of magnitude smaller.

1.6.1 The Born Approximation

The Born Approximation is a method for calculating scattering processes which truncates Figure 1.8 after the very first Feynman diagram. This assumes all higher-order processes contribute an insignificant amount to the cross-section in question, and they are viewed as radiative corrections. From an experimental standpoint, this was a valid assumption for the past several decades. However, advancements in technology and experimental techniques have pushed the precision of experimental results to a point where even the tiny influence of higher-order diagrams has now become significant.

Nearly all of the cross-section formalism which was presented previously is only valid in the Born Approximation. If one wishes to include higher order diagrams, terms such as the hadronic tensor, $W_{\mu\nu}$, must be modified to reflect this.

1.6.2 Next-to-Leading Order

The next-to-leading order diagrams in Figure 1.8 represent the exchange of two photons. In the past, contributions from these diagrams were considered very small or even negligible to the overall systematic uncertainty of a typical measurement. However, recent experiments have shown that this is no longer the case. The development of two-photon

exchange theory has become an essential step towards a more complete description of e-N interactions. It is imperative that a direct observable be found such that the size of two-photon effects can be measured. Perhaps the most enticing observable than can be related to two-photon physics is the single-spin asymmetry of an unpolarized electron scattering from a target which is polarized normal to the scattering plane. The goal of this thesis is to measure the aforementioned quantity, A_y^n, in the DIS region using a polarized ^{3}He target as an effective polarized neutron.

CHAPTER 2

Two Photon Physics

2.1 The Importance of Two-Photon Physics

It has become increasingly clear over the last decade that the inclusion of two-photon (2γ) physics is necessary to understand experimental results at their current precision. While there are several examples of its significance [13], perhaps the most glaring is the discrepancy between two independent methods of measuring the form factors G_E and G_M in Equation 1.7. It has been proposed ([14], [15]) that this inconsistency can be partially reconciled by accounting for 2γ contributions to the elastic e-N cross-section.

These two methods of measuring the Sachs form factors are called the 'Rosenbluth Method' and the 'Polarization method'. The Rosenbluth method relies on the Born cross-section, which is linear with respect to photon polarization, ϵ:

$$d\sigma_R = C_B(Q^2, \epsilon)\left[G_M^2(Q^2) + \frac{\epsilon}{\tau}G_E^2(Q^2)\right] \tag{2.1}$$

where $C_B(Q^2, \epsilon)$ is simply a phase space factor that is irrelevant to this argument [15]. The virtual photon's polarization parameter is defined as:

$$\epsilon = \frac{\nu^2 - M^4\tau(1+\tau)}{\nu^2 + M^4\tau(1+\tau)}$$

and so at fixed Q^2, ϵ is equivalent to ν [16]. This being the case, one can measure $d\sigma_R$ at fixed Q^2 while varying ϵ and extract values of G_E and G_M. The linearity of Equation 2.1 can be interpreted as a test of the validity of the Born approximation.

One can also access the Sachs form factors using a polarized electron beam combined with either a polarized target, or recoil polarimetry of the target. In the case of a target which is initially polarized, one measures longitudinal and perpendicular asymmetries that are related to the ratio G_E/G_M [17]:

$$A_\perp = -\frac{G_E}{G_M} \cdot \frac{2\sqrt{\tau(1+\tau)}\tan\frac{\theta}{2}}{(G_E/G_M)^2 + (\tau + 2\tau(1+\tau)\tan^2\frac{\theta}{2})}$$

and

$$A_\parallel = -\frac{2\tau\sqrt{1+\tau+(1+\tau)^2\tan\frac{\theta}{2}}\tan\frac{\theta}{2}}{(G_E/G_M)^2 + (\tau + 2\tau(1+\tau)\tan^2\frac{\theta}{2})}$$

The recoil polarization method uses a slightly different approach. In the one-photon approximation, the component of the recoiling target particle's polarization which is along its momentum vector (P_l) is proportional to the magnetic form factor, G_M. The transverse component (P_t) is proportional to the product, $G_E G_M$. A measure of the ratio of P_t to P_l

is proportional to the ratio of electric and magnetic form factors as:

$$\frac{P_t}{P_l} = -\sqrt{\frac{2\epsilon}{\tau(1+\epsilon)}}\frac{G_E}{G_M} \tag{2.2}$$

The Rosenbluth and polarization methods are roughly in agreement at low momentum transfer squared. However, as one surpasses about $Q^2 = 2$ GeV^2, they begin to deviate from each other (Figure 2.1).

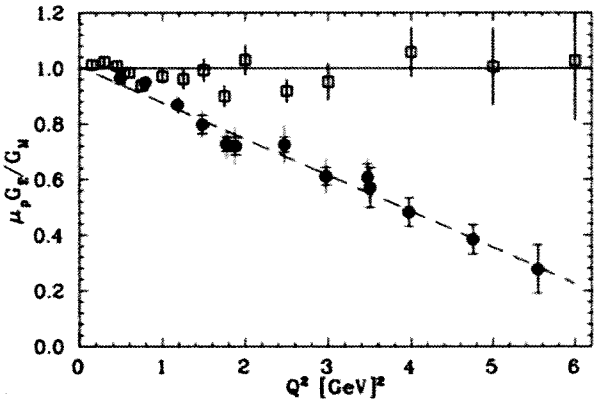

FIG. 2.1: Rosenbluth (blue) and Polarization Transfer (red) measurements of G_E/G_M. Figure is from [18] of data from [19], [20] and [21].

A possible reconciliation of these two methods can be achieved by inclusion of higher order diagrams. This requires that one develop Equations 2.1 and 2.2 such that they reflect the presence of 2γ exchange. Thus, the hadronic current must be written in its most general form. If one neglects the mass of the electron and respects Lorentz, parity and charge conjugation invariance, the T-matrix includes three structure functions (one more than Equation 1.7) [15]:

$$T = \frac{e^2}{Q^2}\bar{u}(k')\gamma_\mu u(k) \times \bar{u}(p')\left(\tilde{G}_M\gamma^\mu - \tilde{F}_2\frac{P^\mu}{M} + \tilde{F}_3\frac{\gamma\cdot K P^\mu}{M^2}\right)u(p) \tag{2.3}$$

Here, the terms $\tilde{G}_M$, $\tilde{F}_2$ and $\tilde{F}_3$ are *complex* functions which carry the structure information of the target. Evidently, when returning to the Born approximation, one should recover the usual Born form factors, and so

$$\tilde{G}_M(\nu, Q^2) = e^{i\phi_M}|\tilde{G}_M| = G_M^{\text{Born}}(Q^2) + \delta\tilde{G}_M$$
$$\tilde{F}_2(\nu, Q^2) = e^{i\phi_2}|\tilde{F}_2| = F_2^{\text{Born}}(Q^2) + \delta\tilde{F}_2$$
$$\tilde{F}_3(\nu, Q^2) = e^{i\phi_3}|\tilde{F}_3| = 0 + \delta\tilde{F}_3$$

where the δ terms indicate the contribution from multi-photon exchange.

The Rosenbluth and Polarization Transfer expressions can now be written in terms of these multi-photon form factors [15]:

$$\sigma_R = G_M^2\left(1 + 2\frac{\mathcal{R}(\delta\tilde{G}_M)}{G_M}\right) + \epsilon\left\{\frac{1}{\tau}G_E^2\left(1 + 2\frac{\mathcal{R}(\delta\tilde{G}_E)}{G_E}\right) + 2G_M^2\left(1 + \frac{1}{\tau}\frac{G_E}{G_M}\right)\frac{\nu}{M^2}\frac{\mathcal{R}(\tilde{F}_3)}{G_M}\right\}$$

and

$$\frac{P_t}{P_l} = -\sqrt{\frac{2\epsilon}{\tau(1+\epsilon)}}\frac{G_E}{G_M}\left\{\left(1 - \frac{\mathcal{R}(\delta\tilde{G}_M)}{G_M}\right) + \frac{\mathcal{R}(\delta\tilde{G}_E)}{G_M} + \left(1 - \frac{2\epsilon}{1+\epsilon}\frac{G_E}{G_M}\right)\frac{\nu}{M^2}\frac{\mathcal{R}(\tilde{F}_3)}{G_M}\right\}$$

where the notation $\tilde{G}_E \equiv \tilde{G}_M - (1+\tau)\tilde{F}_2 = G_E(\nu, Q^2) + \delta\tilde{G}_E$ has been used. The symbol '$\mathcal{R}$' implies that one is taking the *real* part of the amplitude. Due to the size of the kinematic coefficients, the two-photon correction is much more significant in the Rosenbluth method than in the Polarization Transfer method. Application of the correction appears to bring the two methods into better agreement. Figure 2.2 shows an example

of a theoretical calculation which incorporates 2γ exchange [13].

A more complete understanding of the structure of nucleons clearly requires knowledge of the 2γ exchange process. Experimental measurements which probe this effect are of paramount importance to increasing the precision to which structure functions are known. However, it is non-trivial to make a measurement of 2γ physics, as its effects are typically overwhelmed by Born level processes. This raises the question: Is there an observable which is sensitive purely to 2γ physics?

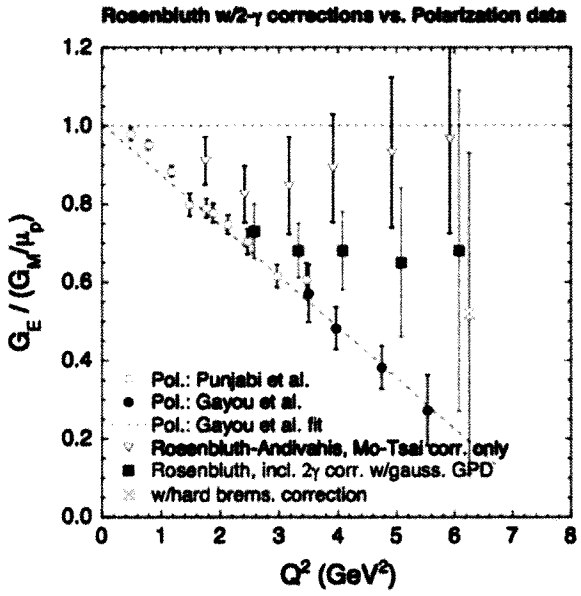

FIG. 2.2: Calculation by Carlson *et al* [13] with 2γ correction applied. Blue is Rosenbluth (uncorrected), black is polarization transfer and green is Rosenbluth corrected for 2γ exchange.

2.2 Experimental Observable for 2γ Exchange

The idea of an observable sensitive to 2γ exchange was first proposed by N. Christ and T. D. Lee in 1966 [22]. The original motivation for their proposal was a test of

charge and time-reversal invariance of the electromagnetic interaction. Specifically, they noted that a systematic study of T invariance could be made by considering the reaction $\ell + N \rightarrow \ell + \Gamma$ where Γ is any final state such that $\Gamma \neq N$. The test is performed by using a polarized target nucleus, and by measuring the correlation function $\vec{S} \cdot \left(\vec{k} \times \vec{k}'\right)$ where $\vec{S}$ is the polarization vector of the initial nucleus and $\vec{k}$ and $\vec{k}'$ are the initial and final momentum of the lepton, respectively. For an unpolarized beam, where the mass of the lepton is neglected, the cross-section for 1γ approximation is given as:

$$\frac{d^2\sigma}{dk' d\cos\theta} = \frac{2\pi\alpha^2 E'}{q^2 k E m_\Gamma} \times \left\{ 2W_1 + W_2 \cot^2\frac{\theta}{2} + \left[\vec{S} \cdot \left(\vec{k} \times \vec{k}'\right)\right] \frac{(E^2 - E'^2)}{m_N^2} W_3 \cot^2\frac{\theta}{2} \right\},$$

where $W_{1,2,3}$ are real, dimensionless functions. An asymmetry is then defined as

$$A_y = \frac{d\sigma^\uparrow - d\sigma^\downarrow}{d\sigma^\uparrow + d\sigma^\downarrow} \tag{2.4}$$

which, when written in terms of cross-sections, is clearly maximized with $\vec{S} \parallel \left(\vec{k} \times \vec{k}'\right)$:

$$A_y = \frac{\left(\frac{E^2 - E'^2}{m_N^2}\right) W_3 \cot\frac{\theta}{2}}{2W_1 + W_2 \cot^2\frac{\theta}{2}}.$$

Christ and Lee showed that if parity conservation and time-reversal invariance hold, then the term $W_3 = 0$ and the asymmetry is identically zero in the Born Approximation. Subsequent theoretical and experimental investigation showed that the Cabbibo-Kobayashi-Maskawa (CKM) theory accurately describes all known cases of CP violation [23]. Thus, 1γ exchange contributes nothing to the target single spin asymmetry. However, it is noted by Christ and Lee that the correlation $\vec{S} \cdot \left(\vec{k} \times \vec{k}'\right)$ is also generated by the interference of one- and two-photon exchange, without violating $T-$invariance. Hence, any non-zero

value for the target single-spin asymmetry (SSA) would be a direct measurement of a two-photon exchange process, being completely void of a Born level contribution.

Further, it can be shown (Appendix A) that for a target polarized normal to the scattering plane, the asymmetry is proportional to the *imaginary* part, $\mathcal{I}$, of the interference of 1γ and 2γ exchange as:

$$A_y = \frac{2\mathcal{I}\{T_{if}\mathcal{A}_{fi}\}}{|T_{if}|^2} \tag{2.5}$$

This is in contrast to the 2γ correction to the ratio of form factors, G_E and G_M, which is sensitive to the *real* part of the interference. However, the asymmetry in Equation 2.5 is significant in that it is not contaminated by large Born contributions, making it an ideal observable to investigate the 2γ process.

2.2.1 Defining Up and Down

In order to compare theoretical predictions and experimental results, it is imperative that a clear definition of 'up' and 'down' be given as it applies to Equation 2.4. The scattering plane is defined by the incoming and outgoing electron momentuma, $\vec{k}$ and $\vec{k'}$. Spin 'up', which is normal to the scattering plane, will then be defined as

$$\hat{S}^{\uparrow} = -\left(\hat{k} \times \hat{k'}\right)$$

while spin 'down' is defined as

$$\hat{S}^{\downarrow} = \left(\hat{k} \times \hat{k'}\right)$$

'Up' and 'down' are meant to be associated with the spin of the target ^{3}He atom (Chapter 4). Thus, spin 'up' means that *both* the ^{3}He atoms AND their magnetic holding field are pointing toward the ceiling of the experimental hall, while 'down' implies that both the atoms and field are pointing toward the floor of the hall.

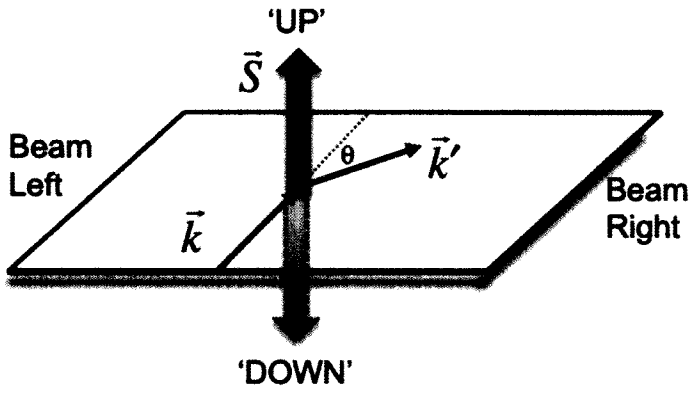

FIG. 2.3: 'Up' and 'down' as defined in this thesis. The target arrow represents the spin direction of the target ^{3}He atom.

2.3 Formalism of 2γ Exchange for a SSA

The goal now is to write down an expression for the cross-section in order to estimate the size of the asymmetry. This requires that the leptonic and hadronic tensors be modified to reflect the fact that the next-to-leading order diagram is being included. Following the formalism laid out in Chapter 1, the matrix element $\mathcal{M}$ is proportional to the Feynman diagrams for the process. For one photon exchange, this can be expressed graphically as depicted in Figure 2.4. Here, each place where an internal propagator touches the lepton (hadron) line is given a 'book keeping' index; in this case, either μ or ν. For 2γ exchange, the matrix element is the sum of the two Feynman diagrams being considered. Thus, the

cross-section is proportional to the square of the sum of the two terms (Figure 2.5)

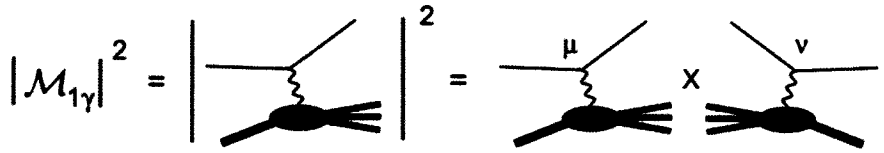

FIG. 2.4: 1γ exchange. Each vertex along the lepton (nucleon) line is represented by an index.

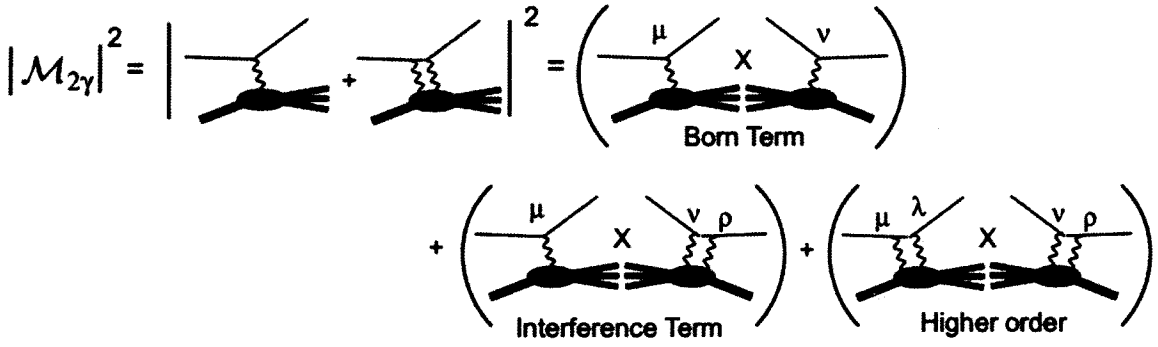

FIG. 2.5: 2γ exchange. Extra indices are needed to keep track of the number of propagators.

It is now clear that the leading contribution to the 2γ asymmetry is the interference between the 1γ and 2γ process. Even though the effect is a sole consequence of 2γ exchange, the Born term amplifies it due to the fact that it only includes one factor of the coupling constant, α. The introduction of the extra photon in the interference term leads to a third book-keeping index, ρ. It follows that the Leptonic and Hadronic tensors for this process will be $L_{\mu\nu\rho}$ and $W_{\mu\nu\rho}$, respectively. The cross-section is given in a form similar to Equation 1.8:

$$\frac{d\sigma}{d\Omega} \propto L_{\mu\nu\rho} W^{\mu\nu\rho}$$

and the tensors are defined as [24]:

$$L_{\mu\nu\rho} = \frac{1}{2} Tr\left(\not{k}\gamma^{\mu}\not{k}'\gamma^{\nu}\not{\ell}\gamma^{\rho}\right)$$

and

$$W^{\mu\nu\rho} = \sum_{q} e_q^3 \frac{Mx}{4\pi Q^2} \frac{1}{(p+k-\ell)^2 + i\epsilon} g_T^q(x) Tr\left(\gamma_5 \not{S}\gamma^{\mu}(\not{p}+\not{k}-\not{k}')\gamma^{\nu}(\not{p}+\not{k}-\not{\ell})\gamma^{\rho}\right)$$

where g_T^q is the twist-3 quark distribution and the shorthand notation $\not{a} = a^{\mu}\gamma_{\mu}$ has been used. Here, 'Casmir's Trick' has been used to write the terms in the form of the trace of a matrix. An explanation of Casmir's trick can be found in any Elementary Particle text book, in particular, [6]. Momenta associated with each particle are shown in Figure 2.6. In principal, the task now is to contract the two tensors and perform an integral to obtain the cross-section, which has the form [24]:

$$\begin{aligned} k'^0 \frac{d\sigma}{d^3\vec{k}'} = & \frac{4\alpha^3}{Q^8} \frac{Mx^2 y}{1-y} \epsilon_{\mu\nu\rho\sigma} S^{\mu} P^{\nu} k^{\rho} k'^{\sigma} \\ & \times \int d^2\vec{p}_T H\left(p_T^2\right) \sum_q e_q^3 \left(x g_T^q(x,\vec{p}_T) - \frac{p_T^2}{2M^2} g_{1T}^q(x,p_T^2) \right) \end{aligned}$$

Here, $\vec{p}_T$ is the transverse momentum of the quarks within the nucleon and g_T and g_{1T} are parton distribution functions. Unfortunately, the function $H(p_T^2)$ is associated with an IR divergence and so the integral cannot be performed. It is currently believed that the inclusion of quark-gluon-quark correlators could possibly lead to an IR finite result [24]. However, one must currently find another means by which to estimate the expected size of the asymmetry. The two currently available examples of estimates are discussed in the next section.

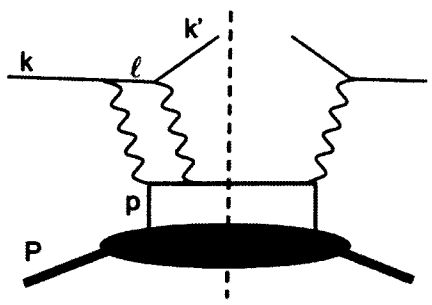

FIG. 2.6: Interference of 1γ and 2γ exchange with momenta defined.

2.4 Theoretical Predictions

To date, only two quantitative prediction of the size of A_y have been produced in the inelastic region. The first was R. N. Cahn and Y. S. Tsai in 1970 [25]. The second was by A. Afanasev, M. Stickman and C. Weiss in 2007 [26]. This section will summarize how each of these predictions were arrived at, as well as some physics implications.

2.4.1 Cahn and Tsai Prediction

The work done by Cahn and Tsai was motivated by experiments that were performed at both the Stanford Linear Accelerator Laboratory (SLAC) and Cambridge Electron Accelerator (CEA) as tests of Time-Reversal Invariance. Their focus was inelastic scattering of electrons from a polarized proton, and they only considered the hadronic final state which consists of one pion plus one nucleon. Further, while their intent was to allow intermediate states of a proton, various N^*'s and continuum states, they stated that the only intermediate state which can be handled reliably is a proton. This is the only case which they treated. In their kinematic region of interest ($Q^2 = 0.6$ GeV^2), the final state $N + \pi$ is dominated by the formation of $\Delta^*(1232)$ and the non-resonant S-wave part.

They ignore the S-wave part, as well as magnetic multipole transitions which contribute to the cross-section. Once these assumptions are made, the cross-sections are calculated for target states up and down, and the asymmetry is formed as in Equation 2.4. The final value is $A_y^p \sim 7.5 \times 10^{-3}$.

2.4.2 Afanasev, Strickman and Weiss Prediction

The recent investigation of 2γ effects in the DIS region, performed by A. Afanasev, M. Stickman and C. Weis, is the first that attempts to relate A_y to the quark structure of the nucleon [26]. This is done via multiple steps. They begin with a study of transverse-spin dependent cross-sections of point-like spin-$\frac{1}{2}$ particles and show that this case exhibits IR-finiteness. This is then extended to transverse spin dependence in DIS in QCD. They argue that this process would be dominated by scattering from a single quark. This leads to two possible contributions to an asymmetry - one which is helicity-conserving and one where quark helicity is flipped. They then formulate a composite nucleon approximation where the helicity-flip contribution dominates, and can be calculated in a relativistic constituent quark model, leading to numerical estimates.

The matrix element for the point-like proton cross-section, in terms of its dependence on initial proton polarization, must be of the form:

$$|\mathcal{M}|^2 = X_U - \frac{SN}{\sqrt{-N^2}} X_N \tag{2.6}$$

where S is the polarization 4-vector of the initial proton state and N is the normal 4-vector characterizing the scattering process. X_U and X_N represent unpolarized and normal-polarization contributions to the matrix element. The transverse target spin asymmetry is

then given as:

$$A_N = \frac{d\sigma(S_y = -1) - d\sigma(S_y = +1)}{d\sigma(S_y = -1) + d\sigma(S_y = +1)} = \frac{X_N}{X_U} = -A_y \tag{2.7}$$

where the proton polarization is chosen to be along the y-axis. It is important to note that the predictions given by Afanasev *et al.* are for A_N, and this experiment measures A_y. Thus, their predictions must be multiplied by -1 before comparing to the experimental results of this thesis. The X terms in Equation 2.6 can be written as:

$$X_U = \frac{1}{2}\left[|\mathcal{M}(y-)|^2 + |\mathcal{M}(y+)|^2\right]$$
$$X_N = \frac{1}{2}\left[|\mathcal{M}(y-)|^2 - |\mathcal{M}(y+)|^2\right]$$

It is revealing to write these terms in a frame where the proton moves in the positive z-direction, where the helicity eigenstates $|\pm>$ coincide with the eigenstates of S_z such that the relation $|y\pm>=(|+>\pm i|->)/\sqrt{2}$ holds. One can then write the X terms as:

$$X_U = \frac{1}{2}\left[|\mathcal{M}(-)|^2 + |\mathcal{M}(+)|^2\right]$$
$$X_N = \mathcal{I}\left[\mathcal{M}^*(-)\mathcal{M}(+)^2\right]$$

Thus, Equation 2.7 becomes:

$$A_N = \frac{2\mathcal{I}\left[\mathcal{M}^*(-)\mathcal{M}(+)^2\right]}{|\mathcal{M}(-)|^2 + |\mathcal{M}(+)|^2}$$

just as in Equation 2.5. Using standard expressions for the spin density matrices of the electron and proton spinors, the full forms of the X terms can be calculated, and the

normal spin asymmetry for a point-like proton is found to be:

$$A_N = -\frac{\alpha M}{2\sqrt{s}} \frac{\sin^3(\theta_{cm}/2)\cos(\theta_{cm}/2)}{\cos^2(\theta_{cm}/2) + \frac{1}{2}\sin^4(\theta_{cm}/2)}. \tag{2.8}$$

This expression for the asymmetry can already give a rough estimate for the asymmetry, albeit neglecting structure. For Mandelstam variable $s = 10$ GeV (which corresponds approximately to values reached at JLab with 6 GeV beam) and at scattering angle of $125°$, the asymmetry is on the order of several times 10^{-4}.

In order to extend this to the quark level, Afanasev *et al.* first argue that the transverse spin-dependent cross-section can be described in a 'parton-like' picture in which the reaction happens predominantly with a single quark. In this case, there are two contributions, defined by whether the quark helicity is conserved or flipped. For quarks of low virtuality, the helicity-flipping amplitudes will dominate due to chiral symmetry breaking [26]. This contribution is of the order of a typical constituent quark mass, $M_q \approx 300$MeV, multiplied by the twist-2 quark transversity distribution, which is given as:

$$h_f(=\delta q) = \int \frac{dz^-}{8\pi} e^{i\eta p^+ z^-/2} \times < pS_T|\bar{\psi}_f(0)\gamma^+\gamma^5\hat{S}\psi_f(z)|pS_T >_{z_\perp=0,z^+=0}$$

where $z^\pm \equiv z^0 \pm z^3$ and $z_\perp$ are light cone vector components and $\bar{\psi}, \psi$ are quark fields with f denoting their flavor. $h_f = \delta q$ is the same function as in Equation 1.16, the quark transversity parton density. The result for the transverse spin asymmetry in inclusive DIS in the composite nucleon approximation is then expressed as:

$$A_N(s, Q^2, x)_{comp} = R(\xi) A_N(s, Q^2)_{point}$$

where $A_N(s, Q^2)_{point}$ is the asymmetry for a point proton, given in 2.8, and

$$R(\xi) \equiv \frac{\sum_f e_f^3 h_f(\xi)}{\sum_f e_f^2 q_f(\xi)} \tag{2.9}$$

with q_f being the unpolarized parton density as in Equation 1.14.

Arriving at a numerical estimate for the asymmetry requires specification of the spin/flavor wavefunction of the nucleon. The two simple models that are considered by Afanasev *et. al.* are '$SU(6)$ spin/flavor wave function' and 'Transversity = helicity distributions'. In the $SU(6)$ model, the probabilities $P_{f\sigma}$ for finding a quark in the neutron wave function with flavor f and spin projection $\sigma = +, -$ along the direction of the transverse neutron spin, are:

$$P_{u+} = \frac{1}{9}, \quad P_{u-} = \frac{2}{9}, \quad P_{d+} = \frac{5}{9}, \quad P_{d-} = \frac{1}{9}$$

with $\sum_{f\sigma} P_{f\sigma} = 1$. Neglecting the effect of spin on the quark momentum distributions, one obtains:

$$R = \frac{e_u^3(P_{u+} - P_{u-}) + e_d^3(P_{d+} - P_{d-})}{e_u^2(P_{u+} - P_{u-}) + e_d^2(P_{d+} - P_{d-})} \tag{2.10}$$

which, for a neutron, yields $R = -0.22$.

In the 'Transversity = helicity distributions' model, one is dealing with a weakly bound nucleon where sea quarks are neglected and valence quark transversity is assumed to be equal to helicity distributions. The ratio in Equation 2.9 can then be evaluated using phenomenological parameterizations for the unpolarized and helicity parton densities. Afanasev *et al.* reports that for $Q^2 \sim$ a few GeV^2, $R \approx -0.2$ for the neutron. Finally,

estimates of the target normal single spin asymmetry are attainable. Their predictions, shown in Figure 2.7, are on the order of a couple times 10^{-4} for the neutron. It is noted by the authors that these results are mostly valid around $x \sim 0.3$. As $x \rightarrow 1$, correlations between the constituents in the wave function become important, and the picture of the composite nucleon is no longer applicable.

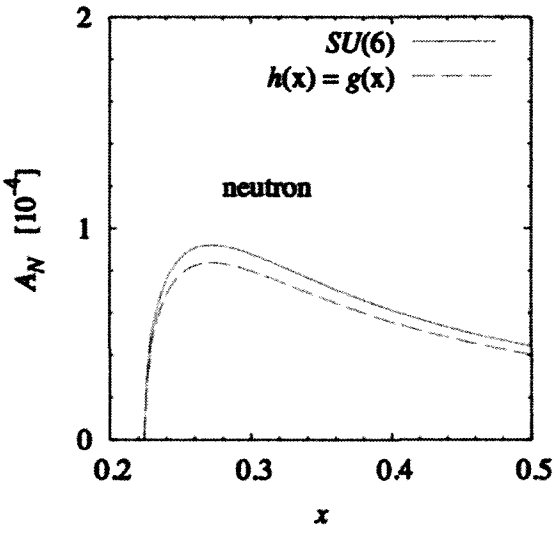

FIG. 2.7: Predictions by A. Afanasev *et al.* for the target normal single-spin asymmetry, $A_N = -A_y^n$, in deep inelastic scattering. The neutron predictions for A_N are positive, meaning they expect a negative A_y^n.

2.5 Existing Data

Only three previous experiments have attempted to measure the target single-spin asymmetry, A_y in the *inelastic* scattering region. Two were performed at the previously mentioned CEA and SLAC and the third was done at HERMES, which is located at the DESY laboratory in Hamburg, Germany.

2.5.1 CEA Data

The first measurement of A_y was done at CEA in 1968 [27] using a $92\% - 8\%$ alcohol-water target which contained protons polarized normal to the scattering plane. Average target polarization was approximately 22% before exposure to the electron beam. The scattered electron energies corresponded to the excitations of the 1236, 1512 and 1688 MeV nucleon resonances with Q^2 between 0.2 and 0.7 GeV^2.

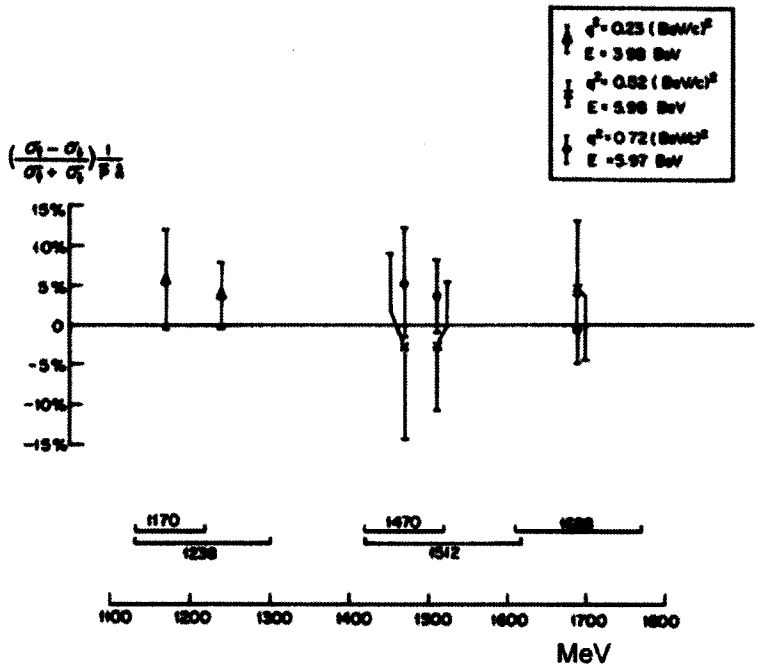

FIG. 2.8: Target single-spin asymmetry data from inelastic electron-proton scattering taken at CEA in 1968.

For each kinematic region, 180 3-minute runs were taken with target polarization being reversed in the pattern uddudduud in order to reduce systematic effects. The asymmetry is

defined as:

$$A = \frac{\sigma_\uparrow - \sigma_\downarrow}{\sigma_\uparrow + \sigma_\downarrow} \frac{1}{\vec{p} \cdot \hat{n}}$$

where $\vec{p} \cdot \hat{n}$ indicates polarization which is normal to the electron scattering plane. Results are shown in Figure 2.8. The experimenters concluded that no signal was seen within their error bars.

2.5.2 SLAC Data

A measurement of A_y^p was performed at SLAC in 1969 [28]. This experiment used an incident electron beam of 15 and 18 GeV, as well as a positron beam of 12 GeV. The positron beam is interesting, as an asymmetry due to time-reversal invariance should be insensitive to lepton charge, whereas a 2γ effect is proportional to charge cubed. Thus, a change in asymmetry sign when going from electron to positron beam would indicate a 2γ signal.

The polarized target consisted of a mixture of 95% 1-butanol and 5% water, saturated with an additional 2% of polyphyrexide. The average target polarization was about 20%. Electrons were detected by a ten-element scintillation-counter hodoscope and identified by the pulse heights in a total-absorption lead-scintillator shower counter. The pion contamination in the data was less than 0.2%. Results are shown in Figure 2.9.

The experimenters concluded that no sign of T-violation was seen. However, it was noted that the positron data, when averaged over the $\Delta(1232)$ resonance, suggests an asymmetry with opposite sign as compared with the electron data. Thus, there exists a possibility of an effect due to the interference of 1γ and 2γ exchange. They note that their

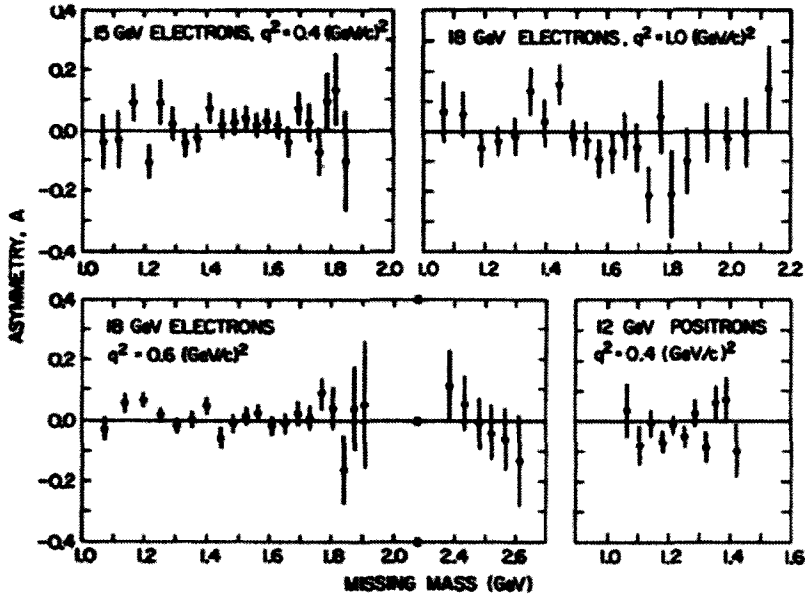

FIG. 2.9: Target single-spin asymmetry data from inelastic electron-proton scattering taken at SLAC in 1969.

elastic data of electrons scattering from polarized protons does not show any asymmetry. Hence, to interpret the inelastic data as a 2γ effect requires a mechanism for enhancing the magnitude of 2γ effects in the region just above the inelastic threshold.

2.5.3 HERMES Data

The most recent attempt at measuring the target single-spin asymmetry, A_y, was performed at DESY in Hamburg, Germany using the HERMES detector [29]. Data acquisition occurred between 2002 and 2005. As an incident beam, this experiment collected data using both an electron and positron beam, each with an energy of 27.6 GeV. Since the asymmetry is sensitive to lepton charge cubed, the asymmetry should experience a sign change when going from one beam to another. The target used was transversely

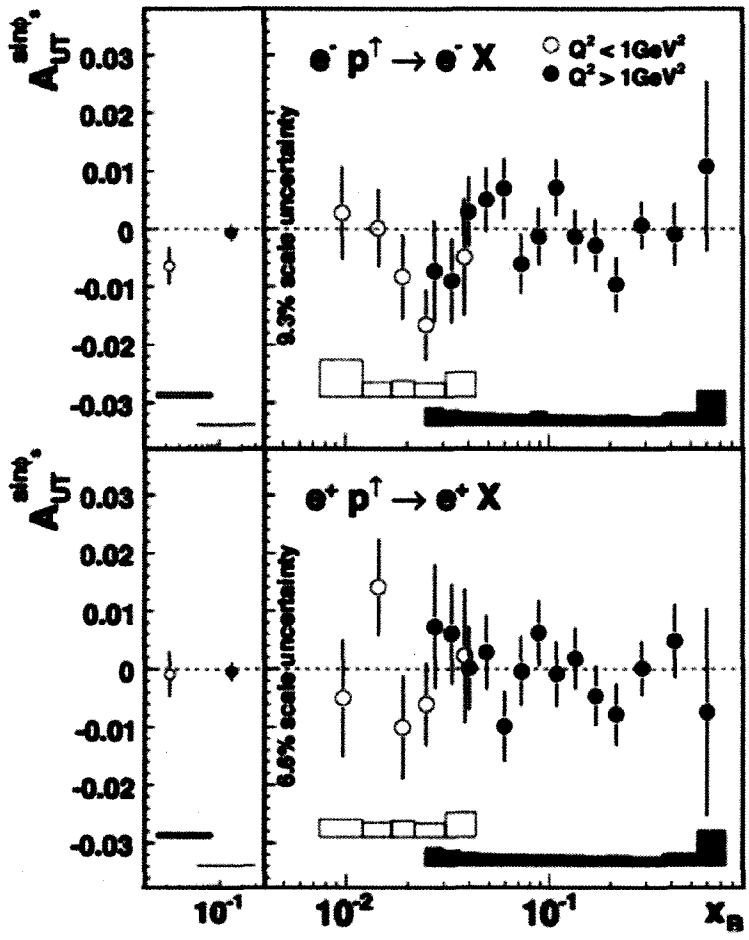

FIG. 2.10: HERMES data (2002-2005) using both electron (top) and positron (bottom) beams scattered from a proton target. Shown is the x_B dependence of the target-normal asymmetry, $A_{UT}^{\sin\phi_S}$, where $U(T)$ indicates unpolarized (polarized) beam (target). Open (closed) circles are $Q^2 < 1$ (GeV/c)^2 ($Q^2 > 1$ (GeV/c)^2). Error bars are statistical uncertainty and boxes are systematic uncertainty. The asymmetries averaged over x_B are shown in the left panel.

(out-of-plane) polarized gaseous hydrogen which is internal to the HERA storage ring at DESY. The direction of the polarization was reversed in 1-3 minute intervals in order to reduce systematic effects. Average target polarization was about 75%. Particle identification was performed using a combination of a transition-radiation detector, scintillating preshower counter, dual-radiation ring-imaging Cherenkov detector and an electromagnetic calorimeter. Hadron contamination was limited to a level of less than 2×10^{-4} and lepton efficiency was 94%.

The kinematic range was $0.007 < x_B < 0.9$ and $0.25 < Q^2 < 20$ (GeV/c)^2. Data were grouped into two regions of $Q^2 < 1$ (GeV/c)^2 and $Q^2 > 1$ (GeV/c)^2. All asymmetry amplitudes were found to be consistent with zero within their uncertainties (10^{-3}), with the exception of the low-Q^2 electron sample, which shows an asymmetry $\sim 1.9\sigma$ from zero. However, there is no indication of a non-zero result for the low-Q^2 positron sample, which must show an asymmetry of opposite sign in order for the result to be interpreted as a 2γ effect.

2.6 Jefferson Lab E07-013

The thesis is a report on the most recent measurement of A_y in the deep inelastic scattering region, which is also the first ever measurement from the neutron. It was performed in Hall A at Jefferson Laboratory in Newport News, VA. The remainder of this document will give a detailed report on all aspects of the experiment, as well as the analysis of the data and its results.

CHAPTER 3

Experimental Apparatus

E07-013 was performed in Hall A of the Thomas Jefferson National Accelerator Facility (TJNAF, a.k.a. JLab) in Newport News, VA. The experiment ran from October 2008 to February 2009. The goal of the experiment was to make a precision measurement of the target single-spin asymmetry from the reaction $n^{\uparrow}(e,e')$ in the deep inelastic scattering region using a polarized ^{3}He target. The reaction was accessed by scattering JLab's continuous electron beam from the Hall A polarized ^{3}He target system, which was polarized normal to the scattering plane. The measurement was inclusive, meaning only the scattered electron was detected. The detection was performed using the Hall A 'Big-Bite' large acceptance spectrometer at an angle of 30°. As an attempt to monitor false asymmetries, the Hall A luminosity monitors were used.

This chapter will discuss the generation of the electron beam, beamline components which monitor beam position and current, the Big-Bite detector package and luminosity monitors. The polarized ^{3}He target will be discussed in detail in the following chapter.

3.1 The Electron Beam Accelerator

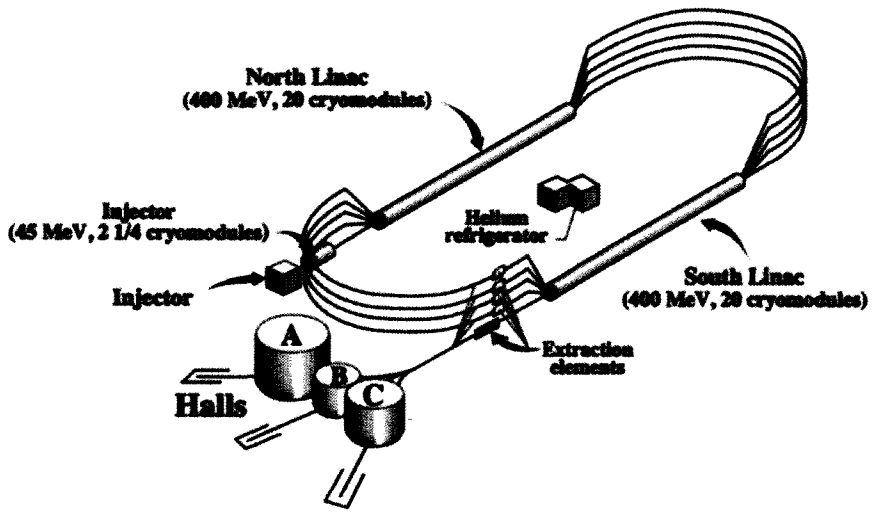

FIG. 3.1: TJNAF accelerator schematic

The main pieces of the accelerator facility at JLab consist of an injector, two linear accelerators ('linacs'), and two recirculation (ARC) magnets. The injector acts as the source of electrons for the entire system. It is made of a strained gallium arsenide (GaAs) cathode which is struck by circularly polarized laser light. Electrons are ejected from the crystal, initially accelerated to 45 MeV and injected into the north linac. The linac is composed of super-conducting cavities that further accelerate the electron up to 570MeV. These cavities are held at 2.0K via a liquid helium bath. Electron acceleration is achieved by a 1497 MHz RF field.

Once the end of the first linac is reached, the electron is bent by a recirculation magnet and travels around an arc. It is then accelerated by a second linac. At the end of this cycle the electron has two options. It can be picked from the accelerator by the extraction element and delivered to one of three experimental halls (A,B or C) or it can

continue around the accelerator as many as four more times to reach a total of ~6 GeV. The 1497 MHz electrons are divided into 3 groups of 499 MHz so that each hall can operate at its desired beam energy.

3.1.1 Beam Generation

The electron beam is generated by shining circularly polarized laser light onto a strained GaAs cathode. The cathode consists of several layers of GaAs, some of which are doped with phosphorus (Figure 3.2). The strain on the GaAs is caused by the shorter lattice spacing of the P-doped layers [30] and removes the degeneracy of the valence band of the GaAs (Figure 3.3) according to electron spin. The amount of splitting between the valence energy levels is roughly proportional to the size of the strain.

The wavelength of the circularly polarized laser light is tuned such that it matches the energy gap, E_G, between the $P_{3/2}$ and $S_{1/2}$ energy levels. As long as the wavelength tuning is precise enough such that it falls between E_G and $E_G + \delta$, angular momentum selection rules will only allow the transitions shown in Figure 3.3. These electrons can escape the conduction band via a negative work function in the surface, which is brought on by the addition of a cesium-flouride layer [31]. The cathode is held at a negative voltage so as to generate an initial acceleration of the ejected electron. It is then injected into the north linac.

The nature of this process means that the electron beam will be polarized when leaving the injector site. If a half-wave plate is inserted into the system before the light reaches the cathode, the laser will be left-circularly polarized. The exiting electrons would then have the opposite polarization. The electron beam at JLab is capable of about 80% beam polarization, and can flip the polarization of the beam to reduce systematic effects.

Since E07-013 is a target single-spin asymmetry, the helicity of the beam was integrated over. The accelerator is capable of delivering more than 100 μA of current to Hall A. However, constraints on the temperature of the ^{3}He target means that the current was never allowed to exceeded 15 μA.

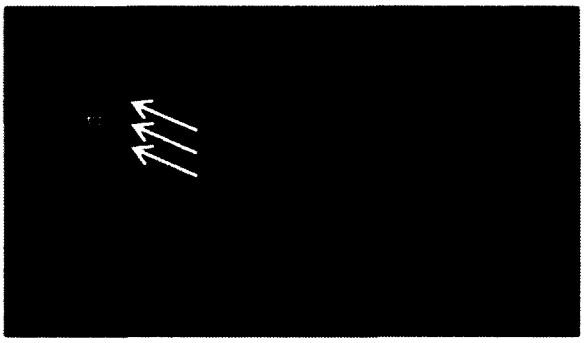

FIG. 3.2: GaAs cathode schematic

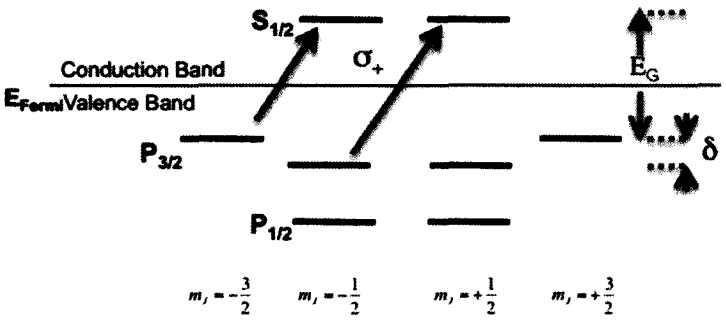

FIG. 3.3: Energy levels for a GaAs crystal under tensile stress. The transitions shown are for right-circularly polarized light. See text for symbol definitions.

3.1.2 Beam Energy

There are several methods by which Hall A can measure the energy of the beam. Among them are the Arc energy method, the eP method, ^{3}He elastic scattering and the

Tiefenbach method. Of these four, E07-013 only relied on two - the Arc energy method and the Tiefenbach method, which is a non-invasive (and thus, slightly less accurate) version of the Arc method.

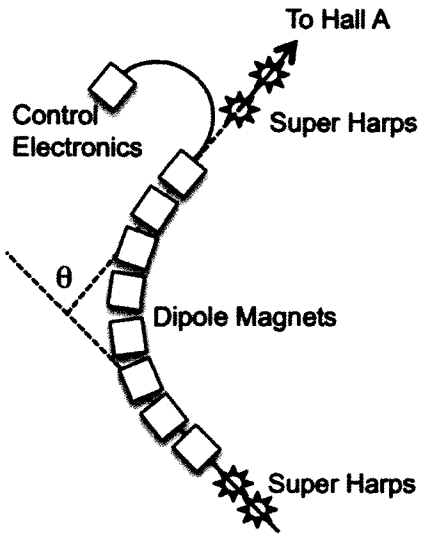

FIG. 3.4: Arc energy measurement schematic

The Arc energy method calculates the beam energy by measuring beam deflection in a known magnetic field while traveling through the 'arced' portion of the accelerator. The deflection will be proportional to both the strength of the magnetic field as well as the momentum (and thus, energy) of the electron:

$$p = c\frac{\int \vec{B} \cdot \vec{dl}}{\theta} \tag{3.1}$$

where θ is the bend angle and c is the speed of light. The source of the magnetic field is the combination of 8 dipole magnets in the arc. The set-points of the dipoles are what determine the nominal bend angle, $\theta = 34.3°$ [32]. Deviations from this nominal value

are detected by wire scanners ('super harps') at the entrance and exit of the arc. Each super harp consist of a thin wire that is scanned through the passing beam. Nearby ion chambers measure the scattering of the beam. The position of the wire is well-known throughout the entire scan, and thus beam position can be calculated. The beam position (and hence, θ) and magnetic field can be plugged into Equation 3.1 to calculate beam energy.

The Tiefenbach method of measuring beam energy is a non-invasive version of the arc method that does not disrupt the beam. Rather than using harp-scans it relies on beam position monitors (discussed later). While they cannot measure beam position to the same accuracy, it does allows for each data run to include a beam energy measurement.

Only one full arc measurement was performed during E07-013, taking place on November 17, 2008. The beam energy was found to be $E_b^{arc} = 5.8894 \pm 0.0005$ (stat.) ± 0.001 (syst.) GeV. The online Tiefenbach calculation was in agreement, at $E_b^{Tief} = 5.8913 \pm 0.0025$ GeV.

3.1.3 Beam Position and Raster

Super harps allow the position of the beam to be measured very precisely. However, they cannot be used as a constant monitor since their usage disrupts the beam. For this reason, special runs are dedicated to harp scans. Precise real-time knowledge of the position of the electron beam entering Hall A is achieved via two Beam Position Monitors (BPMs) that are located $\sim$1.1 and $\sim$7.3 meters upstream from the target (BPMA and BPMB, respectively). Each BPM is simply a cavity with four wires placed 45° from the horizontal and vertical plane. As the beam passes through the BPM each wire will act as an antenna and pick up a signal. The signal size is proportional to the distance from the

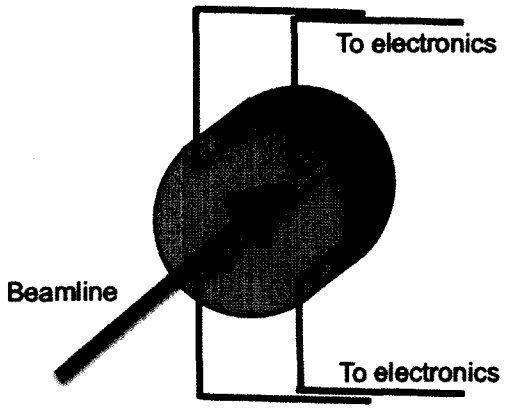

FIG. 3.5: BPM schematic. The wires act as antennas as the beam passes through.

beam. Harp scans are used to calibrate the BCMs.

The polarized ^{3}He target sets constraints on the allowable position of the beam. Certainly, the beam must fall within the cross sectional area of the scattering chamber of the target cell. However, this is not the only demand. Very thin windows are used at the entrance and exit of the ^{3}He scattering chamber. Since the target is under high pressure - typically around 10 atm - the windows are extremely fragile. Aiming the electron beam at one point on the cell windows for too long could heat the window to the point of cell rupture. Short of rupture, this can also lead to local beam-induced density changes in the target cell. For this reason, the beam must be 'rastered' on the window of the scattering chamber.

Beam rastering is performed by two sets of steering magnets that are located 23 meters upstream of the target. One set is oriented such that it deflects the beam horizontally. The second set causes a vertical deflection. By oscillating the frequency and strength of the field the beam can be made to draw out a pattern on the face of the target. For E07-013, the typical raster was a 3×3 mm square.

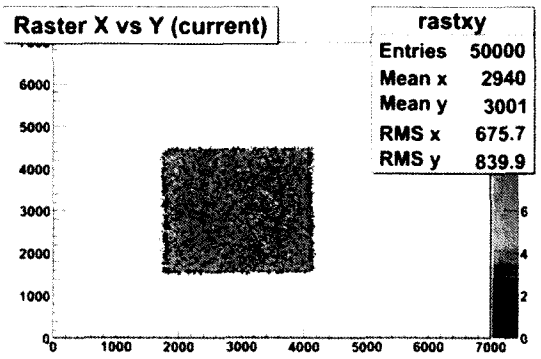

FIG. 3.6: Typical beam rastering during E07-013. Both axis shown are in μm.

3.1.4 Beam Current

It is critical that the total charge incident on the target be monitored, as this number is used to normalize the asymmetry in the analysis. Without this normalization, the asymmetry is meaningless. The charge delivered to Hall A is measured using a Beam Current Monitor (BCM), which consists of an Unser monitor, two RF cavities and the associated electronics [32]. The components are contained in a shielding box to stabilize magnetic and temperature fluctuations. The box is located 25 meters upstream of the target area. The entire system is described in detail in the Hall A Operations Manual [32].

The Unser monitor is a Parametric Current Transformer [32] whose purpose is to provide an absolute reference. It is calibrated by passing a known current through a wire in the beam pipe. The output signal of the Unser is not stable over a time period of several minutes, and thus can not be used as a constant monitor of beam current. To account for this, an RF cavity is placed on each side of the Unser (referred to as the 'upstream' and 'downstream' BCMs). Each RF cavity is a stainless steel waveguide that is tunes to the frequency of the beam (1497 MHz). As the beam passes through the cavity it creates an

electromagnetic field. This field induces a signal in a coil whose response is proportional to the current of the beam.

The RF cavities are regularly calibrated by the Unser throughout the course of an experiment. While the Unser output is only stable over the course of a few minutes, the RF cavities have been shown to be stable over several months of use [32]. Calibration of BCMs is good down to about $5\mu A$, below which the system response is non-linear. For lower currents, there exists a set of amplifiers with gains of $\times 3$ and $\times 10$ which push the non-linear region well below $5\mu A$. Thus, there are a total of 6 BCM readings BCM1_u, BCM3_u, BCM10_u, BCM1_d, BCM3_d, BCM10_d. Each of these signals are fed to the spectrometers and data acquisition systems allowing for several redundancy checks on beam current.

3.2 Detecting the Scattered Electron

Particle detection and tracking during E07-013 were performed using a large acceptance spectrometer that consists of a non-focusing dipole magnet, three drift chambers (DCs), and two electromagnetic calorimeters ('preshower' and 'shower') which are separated by a scintillator plane. Tracking was achieved using the DCs, while particle identification and trigger formation was done using combinations of energy deposited in the two calorimeters. The scintillating layer provided timing information which was used along with the DCs to determine drift time and path reconstruction of a detected particle. A schematic of the detector package can be found in Figure 3.7.

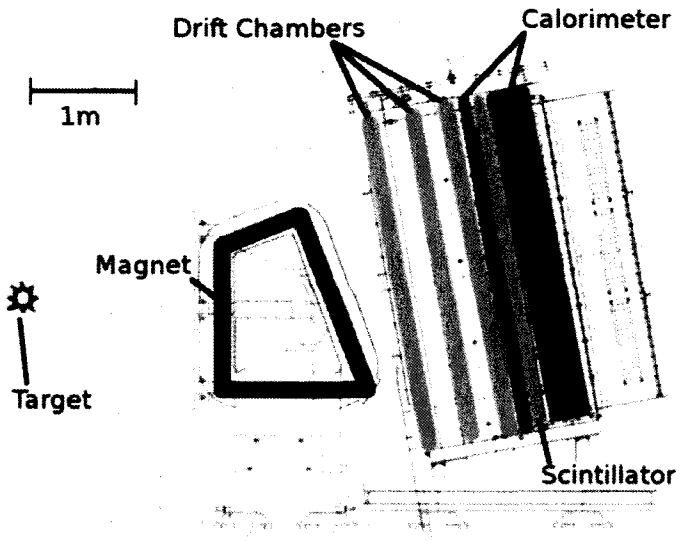

FIG. 3.7: The electron detector package. The blue magnet is referred to as 'BigBite,' which is also commonly used to refer to the entire package.

3.2.1 Big Bite Magnet

Two of the main properties of a spectrometer are its momentum resolution and its spatial acceptance. Optimizing either of these qualities requires different designs. If one desires excellent momentum resolution, the best choice would be a focusing spectrometer. This would usually be made up of a dipole magnet followed by a quadrupole magnet. The dipole magnet effectively acts as a prism, spatially separating particles by momentum, while the quadrupole would act as a sort of microscope, focusing in on one particular momentum. Consequently, the quadrupole magnet will also greatly limit the spatial acceptance of the spectrometer. If, however, one wishes to maximize spatial acceptance, it is best to use a non-magnetic spectrometer. Unfortunately, this comes at the expense of precise knowledge of incoming particle momentum. The BigBite dipole magnet is meant to be a compromise between these two scenarios.

The magnet is placed 1.5 meters from the target area, and has a face gap of 25 cm. The back of the magnet has a pole rotation of 5° to enhance (reduce) the field integral for particles entering the upper (lower) region of the magnet [33]. The design was chosen to detect electrons from an extended target with a length of ± 10 cm projected onto the entrance face [33]. Since the detector package sits at 30° for E07-013, the entire length of the 40 cm target cell can be seen. For E07-013, the momentum acceptance of BitBite was 0.6 - 2.5 GeV/c.

3.2.2 Drift Chambers

Three drift chambers (DCs) were used to reconstruct the path of a particle which passed through the BigBite detector package. Each DC is capable of providing a 2D particle position, with the track being given by combining information from all three. Within a DC are 3 planes of wires, with orientation shown in Figure 3.8.

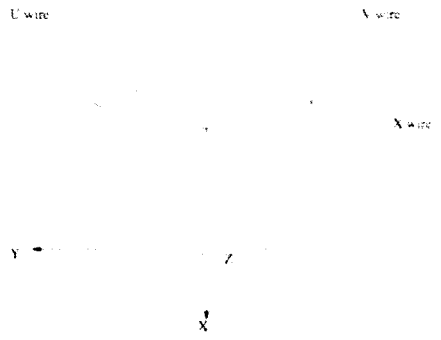

FIG. 3.8: X,U and V wire planes in the drift chambers. The coordinate system shown is that of the entire detector package.

The DC contains a 50/50 mixture of argon and ethane gas, as well as both field source wires and sense wires. These wires are oriented such that the sense wires will be

surrounded by a symmetric electric field. Each sense wire is connected to a Time to Digital Converter (TDC). Any charged particle which passes through the DC will ionize the gas, and these ions will drift toward one of the sense wires, creating a signal in the TDC. The time taken for an ion to drift from the particle location to the sense wire (Δt_{drift}) can be converted into particle position.

Gaining knowledge of the exact drift time is non-trivial, and requires several other pieces of information to extract it. These variables include things such as the time at which the signal from a struck wire reaches the TDC and the time at which the trigger signal arrives at the TDC (see calorimeter section for trigger explanation). For an in-depth discussion on the drift chamber calibration process, see [34].

3.2.3 Scintillators

Figure 3.9 shows a layer of 13 scintillator paddles situated between the preshower and shower calorimeters. Each paddle is fitted with a photomultiplier tube on the end. The scintillator is necessary to provide an extra piece of timing information. When used in conjunction with the tracking information provided by the DCs, the track can be projected back to the target cell to reveal the time and point of interaction in the target. The resolution of the timing signal is on the order of 300 picoseconds.

3.2.4 Calorimeters: Preshower, Shower and Triggers

The BigBite detector package contains 2 layers of calorimeters, called the preshower and shower. The preshower resides just behind the DCs, while the shower is at the back of the detector (see Figure 3.7). Each layer of calorimeter is made up of several lead-glass blocks. There are 54 preshower blocks with dimensions of 8.5 cm x 34 cm x 8.5 cm in X,

Y and Z respectively. Similarly, 189 lead-glass blocks with dimensions 8.5 cm x 8.5 cm x 34 cm (X,Y,Z) make up the shower. See Figure 3.9 for the lay-out of each calorimeter.

When a charged particle passes through one of the lead-glass blocks, an electromagnetic shower is generated. A photomultiplier tube at the end of the block records this signal. The combined size of the signal in the preshower and shower is proportional to the total energy of the particle. Because the signal an electron generates is generally larger than that of a hardon, the combination of preshower and shower signals is useful for both trigger formation and particle identification.

Triggering the Detector

The goal of E07-013 is to detect a scattered electron which is associated with the two-photon process in question. However, particles passing through the BigBite detector are not limited to only this electron; several other 'contaminating' particles are just as likely to generate an electromagnetic shower in the detector. The purpose of the trigger is to tell the data acquisition system to ignore as many of these 'junk' events as possible, recording only the particles pertinent to the experiment. This is done by forming an electronic trigger.

The trigger for E07-013 was formed using the preshower and shower calorimeters in the BigBite detector package. When both calorimeters record a hit from the same particle, the energy deposited in each calorimeter is summed together. The sum of the two signals is then passed to an electronic discriminator, whose threshold can be adjusted to an appropriate minimum value that corresponds to the total energy of the particle to be detected. In this way, particles which deposit very little energy in the calorimeter (such as pions) can be rejected by the detector system rather than being passed to the DAQ.

Several versions of triggers existed for the BigBite detector, and are referred to as T1, T2 , T5, T6 and T7. Many of the triggers were used only by the experiment which E07-013 ran parasitically to ('Transversity'). The main BigBite trigger for Transversity was 'T1', made up of preshower and shower as described above. The trigger for E07-013, 'T6', was a higher threshold version of this T1 trigger, so as to reduce any low-energy background even further. T2 was a copy of T6 which overlapped with a Cerenkov detector. Unfortunately, this Cerenkov detector was under commissioning during E07-013, and was unable to be used.

Calibrating the Preshower and Shower

In order for the sum of the preshower and shower to be equated to the total energy of a particle, the calorimeters must be calibrated by allowing a particle of known energy to be absorbed and leave a signal. For E07-013, this was done using the elastic reaction $\mathrm{H}(e,e')X$ from an H_2 target.

The first step in the procedure is to ensure that the ADC outputs of all shower blocks are acting in roughly the same fashion. A special trigger to detect cosmic rays was set up, since they will typically leave minimum ionization in each block. This minimum output is then aligned to the same ADC channel by adjusting the high voltage on the corresponding photomultiplier tubes (PMTs).

Next, the electron beam is scattered from an H_2 target. Beam energies used were $E_b = 1.231$ and $E_b = 2.306$ GeV. The energy of a scattered electron can be calculated as:

$$E_e = \frac{M_p E_b}{(M_p + E_b(1-\cos\theta))}.$$

Here, M_p is the mass of the proton, E_b the beam energy, and θ is the scattering angle of the electron. This energy is compared to the output of all i ADC amplitudes which can be associated with the given electron:

$$E_i^{ADC} = C_i(A_i - P_i)$$

where A_i is raw ADC amplitude, P_i is ADC pedestal value and E_i^{ADC} is the energy deposited in the i^{th} shower block. C_i is a coefficient to be determined, which transforms the ADC amplitude to the energy of the particle. This is found by a χ^2 minimization, which is defined as the square of the difference in the calculated and measured energies:

$$\chi^2 = \sum_{i=1}^{N} \left(E_e^i - \sum_{j=0}^{M} C_j A_j^i \right)^2$$

where M is the number of blocks in the cluster of shower blocks in question and A_j is the pedestal-subtracted ADC value. This term is minimized with respect to C_i, and the C's are solved for. Details of the χ^2 minimization process can be found in [11]. An energy resolution of $\sigma_{\frac{E}{p}} = 8\%$ was achieved for the reconstructed energy (see Figure **??**).

Detector Deadtime

Due to extremely high rates of particles passing through the detectors, it is impossible to detect every single interaction. This loss in events is known as deadtime (DT). It is important to correct the asymmetry for this DT, as it could introduce a false asymmetry if it is not exactly the same for each target state. The corollary to DT is livetime (LT), which is simply 1 - DT. Measurement of the LT is performed by sending a known number of 'fake' electronic triggers (N_{tot}) to the DAQ system and recording the number that are

received (N_{rec}). The LT is given by:

$$LT = \frac{N_{rec}}{N_{tot}}$$

It is worth pointing out that some triggers have a 'prescale factor' (PS) imposed on them, meaning only 1 out of every PS events are recorded. This factor is thus indirectly included in Equation 3.2. The LT asymmetry was calculated for all of the vertical-target production runs, and was found to be on the order of 1×10^{-4}.

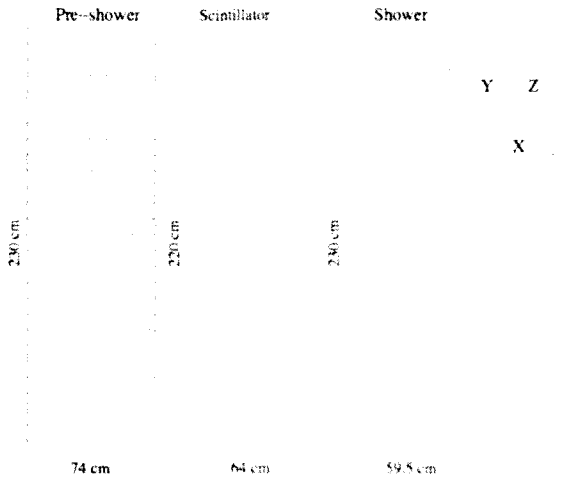

FIG. 3.9: The preshower, scintillator and shower planes of the BigBite detector package.

3.3 Luminosity Monitors

Any experiment which aims to measure such a small asymmetry must make every attempt to limit the occurrence of false asymmetries in the analysis which arise from systematic effects. Two major areas from which systematic uncertainties can arise are the

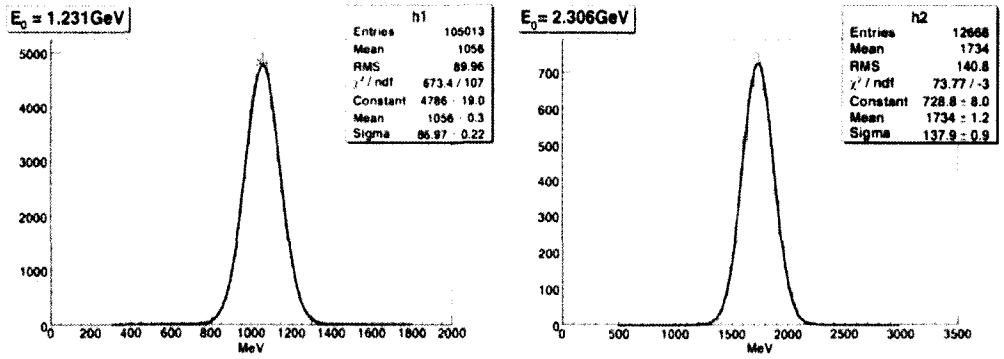

FIG. 3.10: Electron energy reconstruction for E_b = 1.231 Gev (left) and 2.306 Gev (right). The resolution is given by σ/mean, which is about 8%. The mean is lower than the incoming beam energy since there is some energy loss before the scattered particle reaches the shower.

electron beam and ^{3}He target. Beam effects include, but are not limited to things such as position and current drifts. Similarly, target density fluctuations may also give rise to false asymmetries. It is then desirable to define a quantity which is sensitive to these effects. The luminosity is defined as:

$$L = I \times d \times \rho.$$

Here, I is the electron beam current (coulombs/sec), d is the length of the target that the beam interacts with (centimeters) and ρ is the density of the target (typically given as number of nuclei per cubic centimeter). Now, any change in electron beam current or target density can be recognized as a luminosity fluctuation. A single data run in E07-013 intends to maintain a constant current and target density throughout, and hence, should have a constant luminosity. A fluctuation in luminosity would be indicative of a systematic effect.

3.3.1 The Luminosity Detectors

The Luminosity Monitors in Hall A are made up of 8 quartz bars oriented symmetrically around the electron beam pipe at 45 ° intervals, roughly 6.5 meters downstream of the target (Figure 3.11). Due to spacial constraints, 4 of the lumis (1,3,5,7) are situated 6.37 meters downstream, while the remaining 4 (2,4,6,8) are at 6.53 meters downstream (see Figure 3.12 for numbering scheme). This gives scattering angles of 0.5° and 0.7° respectively. When a particle of sufficient energy encounters the quartz, Cherenkov photons are created. These photons travel through a polished aluminum air-light guide and into a photo-multiplier tube (PMT). The analog signal from the PMT is then digitized by an analog-to-digital converter (ADC).

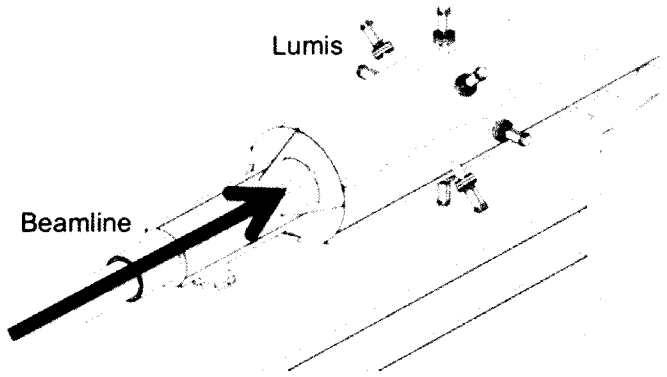

FIG. 3.11: The luminosity monitor system.

3.3.2 Luminosity Monitor Data Acquisition

Until E07-013, the luminosity monitors were used solely by parity experiments which typically measure beam helicity asymmetries. The experiments have a separate

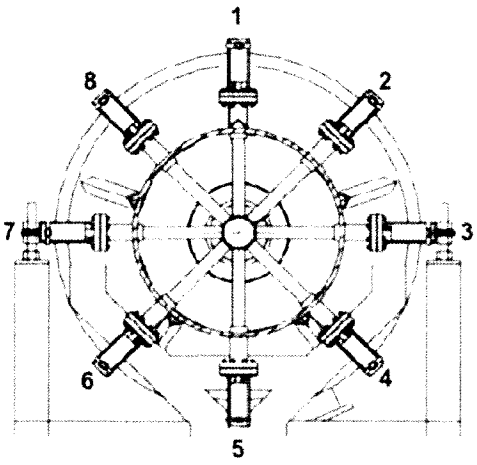

FIG. 3.12: The luminosity monitor numbering scheme, viewed from upstream.

HAPPEX DAQ system that handles the lumi data. For E07-013, both the BigBite DAQ system and the HAPPEX DAQ were run in tandem. New code was written to sample the HAPPEX DAQ every 2 seconds, package the data by beam and target polarization, and finally insert the data into the main DAQ system. This was much more convenient than having two separate, unsynchronized data files for main scattering data and lumi data.

The raw, un-gated lumi ADC signals are acquired via a VME crate in the Right High-Resolution Spectrometer (RHRS) of Hall A. Aside from the ADC signals, the crate also contains a trigger interrupt (TIR), timer, and scaler board. For E07-013, BCM signals of different amplifications were plugged into the scaler board. Target state and beam helicity were connected to the TIR. A typical TCP-IP client/server was set-up between the HAPPEX VME and main DAQ computer. Server code on the VME crate integrated the lumi signal during a data run, gated by both target and helicity state. A client running local to the main BigBite DAQ then requested this 'packaged' data every 2 seconds and inserted it into the main data stream.

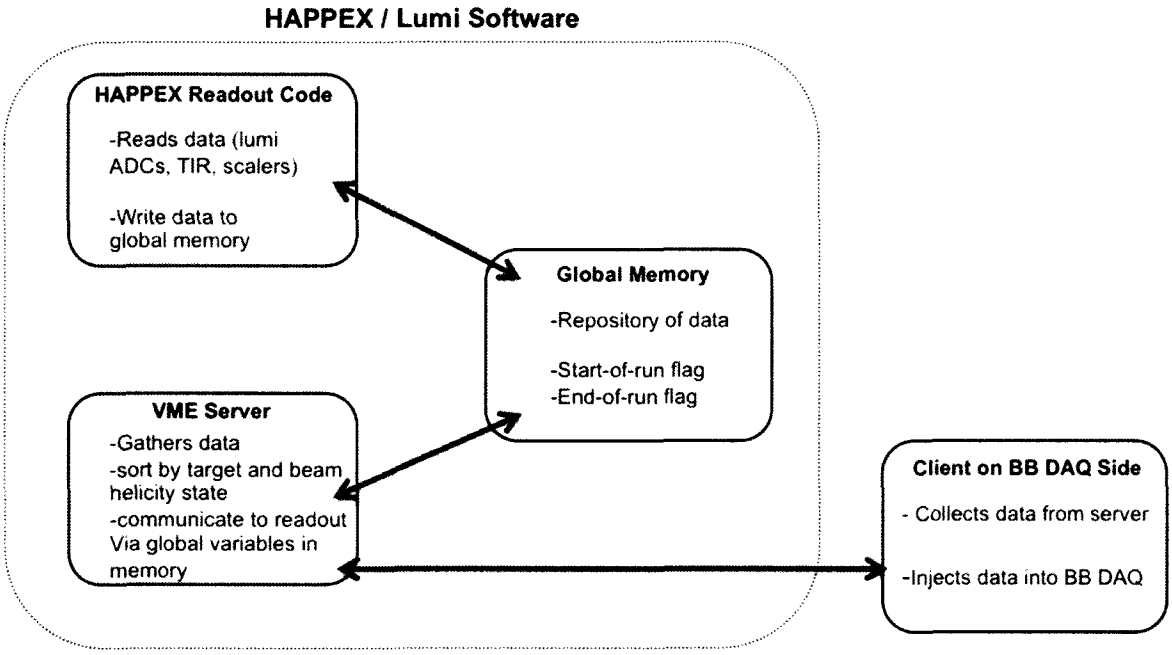

FIG. 3.13: Lumi Data software design

3.3.3 Luminosity Data During E07-013

Figure 3.14 shows the luminosity asymmetry during E07-013. Each luminosity asymmetry was formed from 40 minutes of production data, with 20 minutes spent in the target-up state and 20 minutes in the target-down state. For this analysis, all 8 lumis were summed together. The asymmetry is defined as the difference in lumi signal with target up, $L^{\uparrow}$, and target down $L^{\downarrow}$, divided by the sum of the two. Each term is normalized by the charge accumulated in its respective state:

$$A_{lumi} = \frac{\frac{L^{\uparrow}}{Q^{\uparrow}} - \frac{L^{\downarrow}}{Q^{\downarrow}}}{\frac{L^{\uparrow}}{Q^{\uparrow}} + \frac{L^{\downarrow}}{Q^{\downarrow}}}$$

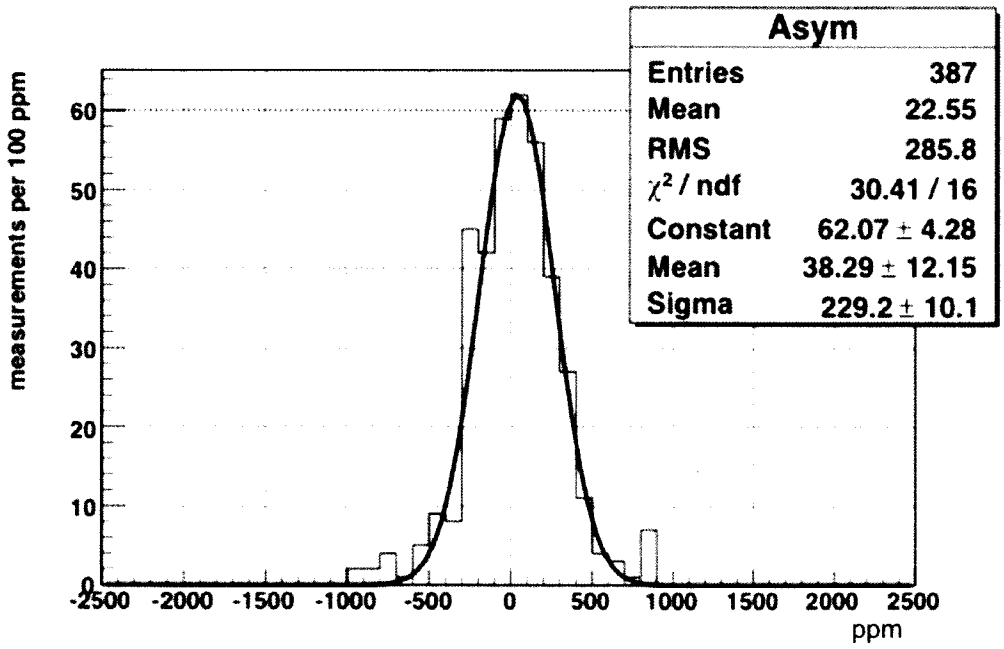

FIG. 3.14: A histogram of luminosity asymmetries. Each entry in the histogram represents a 40 minute section of data, distributed evenly between target state up and down. The smooth curve is a gaussian fit to the data. The mean of the fit is $\sim$ 40 ppm.

The asymmetry for vertical data is found to have an average of $4 \pm 23 \times 10^{-5}$. Similarly, the transverse data shows an asymmetry of $6 \pm 22 \times 10^{-5}$. The size of the asymmetry and error is small compared to the overall statistical error of the experiment, and thus no luminosity correction is made to the final physics asymmetry. Instead, it is included in the systematic error budget.

3.4 Polarized ^{3}He Target

E07-013 made use of the Hall A polarized ^{3}He target system. It consisted of a glass cell which contained ^{3}He gas as well as a Rb-K alkali mixture and N_2. The cell is polarized via a two step process of spin-exchange optical pumping (SEOP). Two types of polarimetry, nuclear magnetic resonance (NMR) and electron paramagnetic resonance (EPR) were used. Both of these methods involve a spin-flip process called adiabatic fast passage (AFP). The polarized ^{3}He target is discussed in detail in Chapter 4.

CHAPTER 4

Polarized ^{3}He Target

4.1 ^{3}He: A Free Neutron Substitute

For any experiment that aims to study the structure of the nucleon, one must first decide on a source of nucleons from which the electron beam can scatter. In the case of electron-proton scattering the options are quite numerous, as there are several readily available high-density sources of protons, most notably hydrogen. However, an experimenter who wishes to study the structure of neutrons faces a major dilemma - a free neutron has a lifetime of only $\sim 887.4 \pm 1.7$ seconds (just under 15 minutes) [35]. As a substitute, one can use neutrons which are bound inside the nucleus of an atom. The simplest of these is deuterium. This serves well as an unpolarized target. However, if one wishes to use a polarized target, a large correction must be made since the polarization is shared between the proton and neutron. For experiments that desire a polarized target, the ^{3}He nucleus is a more natural choice.

4.1.1 The ^{3}He Nucleus

Not only does the ^{3}He nucleus offer a source of neutrons; it also has desirable polarization properties. To first order, the ground state of ^{3}He can be thought of as a pure S wave. In this case, the Pauli exclusion principle requires that the spins of the protons cancel while the spin of the neutron is parallel to the ^{3}He atom. Naively, this results in a polarized neutron target. In reality the ground state of the ^{3}He wave function actually contains a percentage of other angular momentum states, S' and D waves, as well. These contributions are responsible for the proton polarization of ^{3}He. In order to calculate the amount that each state contributes, one must consider the probability, $\mathrm{P}_{n(p)}^{+(-)}$, of having a neutron (proton) with spin aligned (anti-aligned) to the spin of the ^{3}He. In the case of a pure symmetric S wave, one has

$$\begin{aligned} P_n^+ &= 1, \quad & P_n^- &= 0 \\ P_p^+ &= \frac{1}{2}, \quad & P_p^- &= \frac{1}{2} \end{aligned} \tag{4.1}$$

When one takes into account the S' and D wave portions of the wavefunction, these probabilities become [36]

$$\begin{aligned} P_n^+ &= 1 - \Delta, \quad & P_n^- &= 0 + \Delta \\ P_p^+ &= \frac{1}{2} - \Delta' \quad & P_p^- &= \frac{1}{2} + \Delta' \end{aligned} \tag{4.2}$$

where [37]

$$\Delta = \frac{1}{3}[P_{S'} + 2P_D] \quad \text{and} \quad \Delta' = \frac{1}{6}[P_D - P_{S'}] \tag{4.3}$$

The effective nucleon polarizations, $p_{n(p)}$, are then given by

$$\begin{aligned} p_p &= P_p^+ - P_p^- = -2\Delta' \\ p_n &= P_n^+ - P_n^- = 1 - 2\Delta \end{aligned} \tag{4.4}$$

Values for Δ and Δ' are dependent on the model of the ^{3}He wavefunction used to calculate them [36, 37]. Averaging over all models, one arrives at the following:

$$\begin{aligned} \Delta &= 0.07 \pm 0.01, \quad & \Delta' &= 0.014 \pm 0.002 \\ p_n &= 0.86 \pm 0.02, \quad & p_p &= -0.028 \pm 0.004 \end{aligned} \tag{4.5}$$

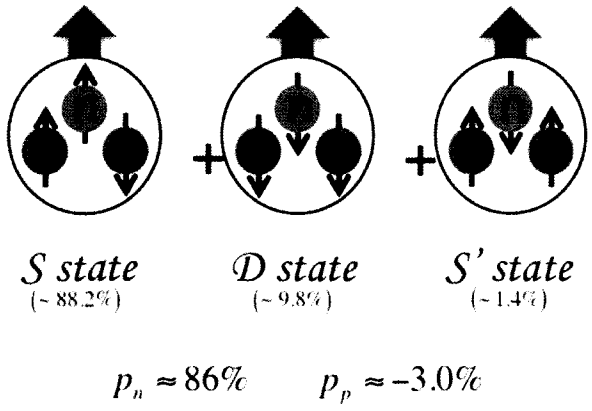

FIG. 4.1: Schematic representation of the ground state of the ^{3}He nucleus.

4.1.2 ^{85}Rb Atomic Structure

The atomic structure of the Rb atom will play a crucial role in many aspects of the polarized ^{3}He target. Both the process of polarization as well as polarimetry measure-

ments will depend on an understanding of the different effects that govern the energy levels of Rb's $5S_{\frac{1}{2}}$ valence electron. For these reasons, it will be convenient to write down the Hamiltonian of a Rb atom.

At its lowest level, the Rb atom is simply a negatively charged electron bound to a positively charged nucleus via the Coulomb potential,

$$V_c = \frac{-Zq_1q_2}{4\pi\epsilon_0 r} \tag{4.6}$$

where Z is the atomic number, q_1 and q_2 are the nucleus and electron charge, respectively, and r is the separation of the two. This potential, along with an appropriate wavefunction for Rb, ψ_{Rb}, can be plugged into Schroedinger's equation to solve for the energy eigenvalues of the system. These eigenvalues will not constitute a continuous spectrum, but rather have the form

$$E_n = \frac{c_0\left(\psi_{Rb}\right)}{n^2} \tag{4.7}$$

where c_0 is some number dependent on the wavefunction chosen. The n is some positive integer and is referred to as the principal quantum number. This is the most basic form of energy quantization in an atom. Evidently, an atomic system viewed in the simplest of ways can have electronic energy E_1, E_2, E_3, etc. Of course, the interaction between an electron and its nucleus are not limited to the Coulomb potential. Among other effects, the description above neglects the intrinsic property of spin, as well as any orbital angular momentum of the system. These will further define the structure of the atom.

Classically, the atom can be viewed as an electron orbiting a nucleus. In a frame of reference where the electron is fixed, this means the nucleus is orbiting the electron. The

nucleus has charge, and an orbiting charge will create a magnetic field. The spin of the electron will couple to this magnetic field and modify the allowable energy eigenvalues of the system (here, 'couple' simply means the the electron - a magnetic dipole - will attempt to align itself with any magnetic field it encounters). This is called 'fine structure' of the atom (also 'spin-orbit' interaction), and can be written as

$$E_{fs} = c_1 \left(\vec{L} \cdot \vec{S} \right). \tag{4.8}$$

Spin-orbit interaction is sometimes said to describe the 'shape' of the electron's orbit about the nucleus and the energy levels it brings about are typically referred to as S, P, D, F, etc.

Still, this picture is not complete. Since the nucleus is not point-like, it is tempting to use the classical analogy of a charged sphere rotating about an axis. This creates yet another magnetic field due to rotating charge, and, similar to fine structure, will couple to the spin of the electron and modify the energy levels. This is 'hyperfine structure,' and is expressed

$$E_{hf} = c_2 \left(\vec{I} \cdot \vec{J} \right) \tag{4.9}$$

where $\vec{I}$ is the spin of the nucleus and $\vec{J} = \vec{L} + \vec{S}$ is the total angular momentum of the electron. For ^{85}Rb, I=5/2 (and thus m_I = -5/2,-3/2,-1/2,1/2,3/2,5/2). The entire system has total spin $\vec{F} = \vec{I} + \vec{J}$. A Rb valence electron in its ground state, then, can have F=3 or F=2, depending on whether $\vec{J}$ is parallel or anti-parallel (respectively) to $\vec{I}$.

The natural energy levels of Rb have now been determined. However, energy eigenvalues of the Rb valence electron can still be modified by external means. If a Rb atom is

placed in an externally applied magnetic field, $\vec{B}_{ext}$, the total spin of the electron-nucelon system will couple to it. This will break the degeneracy of the hyperfine structure of the atom as seen in Figure 4.2.

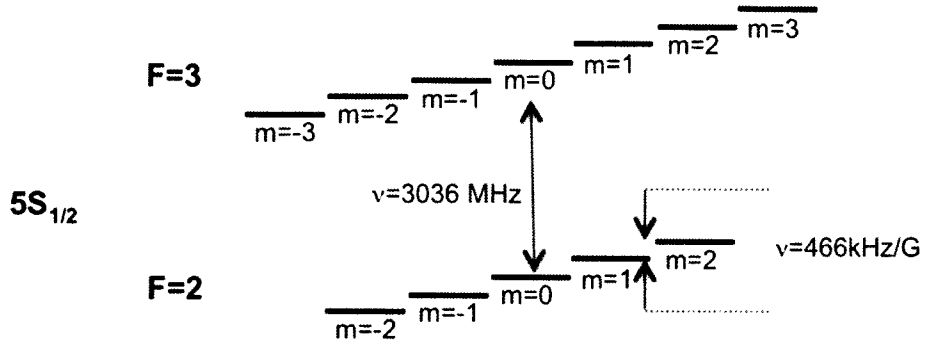

FIG. 4.2: The $5S_{\frac{1}{2}}$ energy level of ^{85}Rb. An applied magnetic field causes the the Rb valence electron states to become non-degenerate. Values of level splitting are for a field of 25 Gauss.

The Hamiltonian of the Rb valence electron can now be written as the sum of each interaction term:

$$H_{tot} = \frac{c_0}{n^2} + c_1(\vec{L} \cdot \vec{S}) + c_2(\vec{I} \cdot \vec{J}) + c_3(\vec{F} \cdot \vec{B}_{ext}). \tag{4.10}$$

The first term is due to the Coulomb interaction. The second is fine structure. Third is hyperfine structure. Lastly is the coupling of the electron and nuclear spin to the applied magnetic field, B_{ext} ('Zeeman effect'). Equation 4.10 could be expanded even further to include a Pauli repulsion term (coupling between the spin of the valence electron with electrons in lower energy levels), but this effect is several orders of magnitude smaller, and thus insignificant to this experiment. It is worth pointing out that all of the interactions mentioned above (Coulomb potential aside) are nothing more than a magnetic dipole (the electron) attempting to align itself with some magnetic field. The only difference is the

origin of the magnetic field.

4.1.3 Spin Exchange Optical Pumping

With it now clear that a polarized ^{3}He atom would effectively act as a free neutron target, the obvious question is raised: How can we polarize a ^{3}He nucleus? There are two widely used methods to achieve this. The first is Metastability Exchange Optical Pumping (MEOP). This technique is based on optically driving the $2\ ^3S_1 \rightarrow 2\ ^3P_0$ transition of ^{3}He's $2\ ^3S_1$ electron with circularly polarized light. The polarization of the optically pumped electron is then transfered to the nucleus via the hyperfine interaction [38]. While the achieved polarizations of this method are quite attractive, the drawback is that the ^{3}He density must be relatively low. For statistics-driven experiments, this can be a major detriment. For an in-depth explanation of MEOP, see [39].

The second method is Spin Exchange Optical Pumping (SEOP), a multi-step process that is much better suited for polarizing high density targets. The first step is to optically pump the valence electron of an alkali metal. In the second step, the alkali metal transfers its polarization to the ^{3}He nucleus by spin-exchange interaction. At Jefferson Lab, the ^{3}He target uses rubidium as the alkali metal. The optical pumping of Rb relies on selection rules that arise from conservation of angular momentum. Figure 4.3 shows the $n = 5$ level (outer shell) of Rb. For now, nuclear spin will be ignored.

When placed in an external magnetic field, the Zeeman Effect causes the energy levels to split. Conservation of angular momentum requires that for any electronic transition, $\Delta m_j = \pm 1$. If the Rb is pumped with right circularly polarized light tuned to the D1 transition ($\lambda = 795$ nm), the electron can only be excited from the 5S, $m_J = -1/2$ level to the 5P $m_J = +1/2$ level (from now on, these will be denoted 5S(P)$_{\pm\frac{1}{2}}$). Likewise,

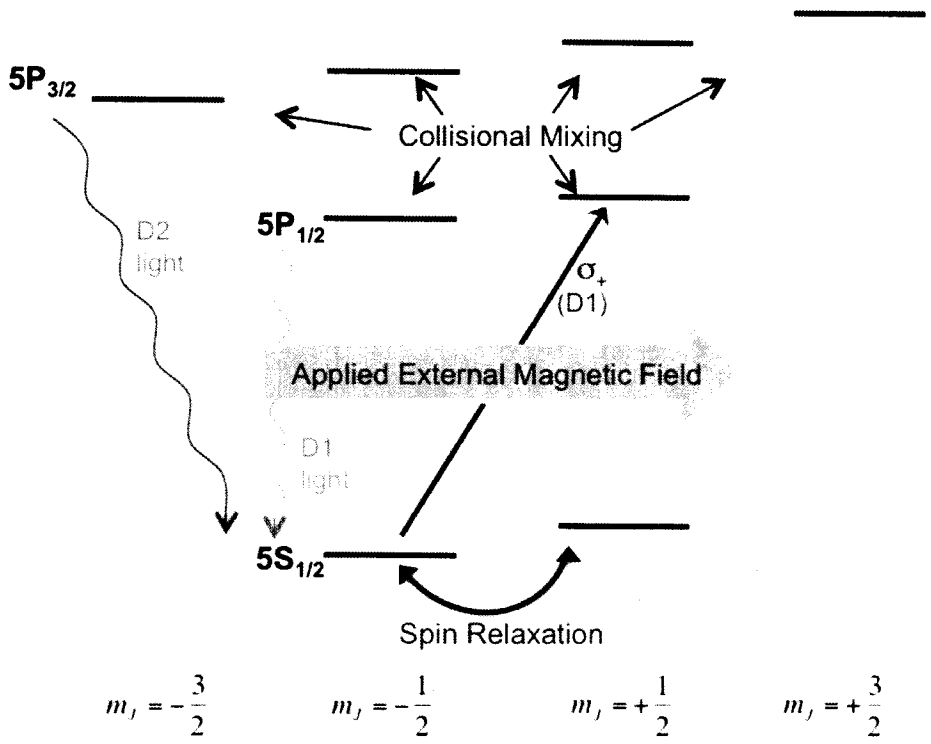

FIG. 4.3: Rb ground state sub-levels (ignoring Rb nuclear spin)

left circularly polarized light could be used to drive the $5S_{+\frac{1}{2}}$ to $5P_{-\frac{1}{2}}$ transition. For this experiment, right circularly polarized light is used. Either way, the $5P_{\frac{1}{2}}$ level is not stable, and the electrons will quickly decay back to either the $5S_{+\frac{1}{2}}$ or $5S_{-\frac{1}{2}}$ state. Each state is equally probable due to collisional mixing in the 5P energy level. While selection rules prohibit the $5S_{+\frac{1}{2}}$ electrons from further pumping, the $5S_{-\frac{1}{2}}$ are continually excited back to the $5P_{+\frac{1}{2}}$ level, only to decay again. This iterative process ensures that over time the $5S_{+\frac{1}{2}}$ state becomes populated.

A complication arises when electrons undergo a 5P $\rightarrow$ 5S transition. In order to decay, the electron must radiate a photon, and the photon does not necessarily have the same polarization or propagation direction as the pumping light. This photon, which *does*

have the same wavelength as the pumping light, will almost certainly be absorbed, causing depolarization. To counter this problem, a trace amount (1%) of N_2 gas is added to the ^{3}He sample. N_2 has both rotational and vibrational degrees of freedom which can absorb energy. For this reason, the quenching cross-section of N_2 (or any diatomic molecule) is much higher than that of ^{3}He. The desirable consequence is radiationless quenching of the excited electrons back to the ground state [31].

As discussed in Section 4.1.2, the picture is confounded when taking into account the non-zero nuclear spin of Rb which leads to the hyperfine interaction. The important thing to note is that there still exists an energy level from which the electron can no longer be excited by right circularly polarized light ($F = 3, m_F = 3$).

The average polarization that the Rb can expect to obtain via optical pumping is estimated as [9]

$$P_{Rb} = \frac{R_p}{R_p + \Gamma_{SD}}. \tag{4.11}$$

where R_p is the optical pumping rate and Γ_{SD} is the electron spin depolarization rate. The optical pumping rate is defined as

$$R_p = \int \Psi(\nu)\sigma(\nu)d\nu \tag{4.12}$$

with $\Psi(\nu)$ being the photon flux per unit frequency and $\sigma(\nu)$ is the cross section of the light absorbed.

4.1.4 Spin Exchange and Relaxation

Spin exchange between the nucleus of a noble gas and the valence electron of an alkali metal as well as alkali spin relaxation are governed by the strength of the magnetic-dipole interaction. For spin exchange the interaction is given by [40]:

$$H_{KS} = \alpha \vec{K} \cdot \vec{S} \tag{4.13}$$

where $\vec{K}$ is the ^{3}He nuclear spin and $\vec{S}$ is the Rb electron spin. For spin relaxation, the leading contributer to Γ_{SD} in Equation 4.11 is the spin-rotation interaction during collision among Rb atoms or between Rb atoms and other gases:

$$H_{NS} = \gamma \vec{N} \cdot \vec{S}. \tag{4.14}$$

In Equation 4.14, $\vec{N}$ is the rotational angular momentum of the Rb. Both α and γ are functions of the internuclear separation, R, of the Rb and ^{3}He which are interacting. Equation 4.13 is dominated by the Fermi-contact interaction

$$\alpha(R) = \frac{16\pi}{3} \frac{\mu_B \mu_K}{K} |\psi(R)|^2 \tag{4.15}$$

where μ_B is the Bohr magneton, μ_K is the magnetic moment of ^{3}He, and $\psi(R)$ is the wavefunction of the Rb valence electron evaluated at the position of the ^{3}He. The cross section for spin exchange is of the order 10^{-24}cm^2 [41].

Nuclear polarization of the ^{3}He increases with time as

$$P_{^3He}(t) = \langle P_{Rb} \rangle \frac{\gamma_{SE}}{\gamma_{SE} + \Gamma} \left[1 - e^{-(\gamma_{SE}+\Gamma)/t}\right] \tag{4.16}$$

where $\langle P_{Rb} \rangle$ is the average Rb polarization and $\gamma_{SE} = k_{SE}[\mathrm{Rb}]$ is the spin exchange rate with k_{SE} being the spin exchange coefficient. The concentration of Rb is denoted as [Rb]. The ^{3}He nuclear relaxation is represented by Γ. The rate of relaxation is determined by performing a spin-down measurement, where the ^{3}He polarization versus time is measured in the absence of SEOP. The exponential decay rate constant τ is called the lifetime of the target cell and is related to the spin relaxation rate as $\Gamma = \tau^{-1}$ [42]. The relaxation rate in terms of the main depolarization sources is

$$\Gamma = \Gamma_{\mathrm{dipole}} + \Gamma_{\mathrm{field}} + \Gamma_{\mathrm{wall}} + \Gamma_{\mathrm{beam}}. \tag{4.17}$$

Here, Γ_{dipole} is due to ^{3}He-^{3}He magnetic dipole interactions, Γ_{field} is due to an external magnetic field gradient, Γ_{wall} is due to collision with the target cell wall and Γ_{beam} is from ionization of the ^{3}He atoms as the beam passes through the target [42].

In the limit that $\langle P_{Rb} \rangle = 1$ and $\Gamma \ll \gamma_{SE}$, the polarization should approach unity. However, a recent study [43] has found an "excess" temperature-dependent relaxation that scales with the alkali-metal density. Their results indicate the presence of a surface relaxation parameter that is correlated to the surface to volume ratio of the target cell. This leads to a new expression for the ^{3}He polarization:

$$P_{^3He} = \langle \mathrm{Rb} \rangle \frac{\gamma_{SE}\,[\mathrm{Rb}]}{\gamma_{SE}\,[\mathrm{Rb}]\,(1+X) + \Gamma} \tag{4.18}$$

where the phenomenological parameter X has been introduced to indicate that the slope of Γ vs. [Rb] is greater than 1. Further study of this 'X-factor' is ongoing.

4.1.5 SEOP Using Hybrid ^{3}He Cells

It is now well known that substituting lighter alkali metals such as Na and K for Rb would result in higher spin exchange efficiencies between an alkali-noble gas pair [44]. It is only the lack in availability of lasers of the appropriate frequency, linewidth and power that prevents this alkali substitution from being made. Despite this, it is still possible to make use of a 'hybrid' scheme that takes advantage of the high spin-exchange cross section between alkali metals. In order to compare the effectiveness of hybrid target cells, one defines a spin-exchange efficiency as the ratio of the rate at which polarized ^{3}He is produced to the rate at which the electronic spin-polarized alkali relaxes [45]:

$$\eta_A = \frac{\gamma_{SE}^A[^3\mathrm{He}]}{\Gamma_A[\mathrm{A}]}. \tag{4.19}$$

$\gamma_{SE}^A = k_{SE}^A[\mathrm{A}]$ is the spin-exchange rate from the alkali (Rb or K) to ^{3}He, k_{SE}^A is the spin-exchange rate constant for the alkali, [A] is the number-density of the alkali vapor, [^{3}He] is the number density of the ^{3}He, and Γ_A is the alkali's electron spin relaxation rate. For a pure Rb cell, the spin-exchange efficiency is

$$\eta_{Rb} = \frac{\gamma_{SE}^{Rb}[^3\mathrm{He}]}{\Gamma_{Rb}[\mathrm{Rb}]}. \tag{4.20}$$

In the case of hybrid alkali mixtures, the spin-exchage rate (the γ term) must be modified:

$$\gamma_{SE}^{Rb+K} = k_{SE}^{Rb}[\mathrm{Rb}] + k_{SE}^{K}[\mathrm{K}]. \tag{4.21}$$

Similarly, the spin-relaxation rate must be modified to account for the presence of K:

$$\Gamma'_{Rb} = \Gamma_{Rb} + D\Gamma_K + q_{KR}[\mathrm{K}] \tag{4.22}$$

where D is the density ratio of Rb to K, D =[K]/[Rb] and q_{KR} is the spin-relaxation rate for Rb-K collisions. Finally, we can write the spin-exchange efficiency for a Rb-K alkali mixture:

$$\eta_{Rb,K} = \frac{(k_{SE}^{Rb}[\mathrm{Rb}] + k_{SE}^{K}[\mathrm{K}])[^3\mathrm{He}]}{(\Gamma_{Rb} + \frac{[\mathrm{K}]}{[\mathrm{Rb}]}\Gamma_K + q_{KR}[\mathrm{K}])[\mathrm{Rb}]}. \tag{4.23}$$

Recent measurements [46, 47] have shown that k_{SE}^{Rb} and k_{SE}^{K} are very close in value, both around $6\times10^{-20}\mathrm{cm}^3/\mathrm{s}$. However, $\Gamma_k \ll \Gamma_{Rb}$. Further, an extremely high spin-exchange rate between K and Rb quickly brings the polarization of the two to equilibrium. Because of this, the lower spin-relaxation rate of K can be exploited without modifying the laser pumping system. The benefits of this hybrid method of polarization are also clearly dependent on the ratio of the alkali densities, D. See [45] for an in-depth study.

4.1.6 Circularly Polarized Rb Laser Light

As discussed in 3.1.2, exploiting the angular momentum selection rules via optical pumping requires that one finds a way to deliver circular polarized light to the ^{3}He-alakali mixture. However, the Rb diode lasers at Jefferson Lab provide unpolarized light. There is no way to immediately turn the emitted laser light into circularly polarized light, so one must instead manipulate each of its two components - S and P waves (referring to the direction of electric fields, not to be confused with S and P energy levels). Figure 4.4 describes the optics used to perform this decomposition.

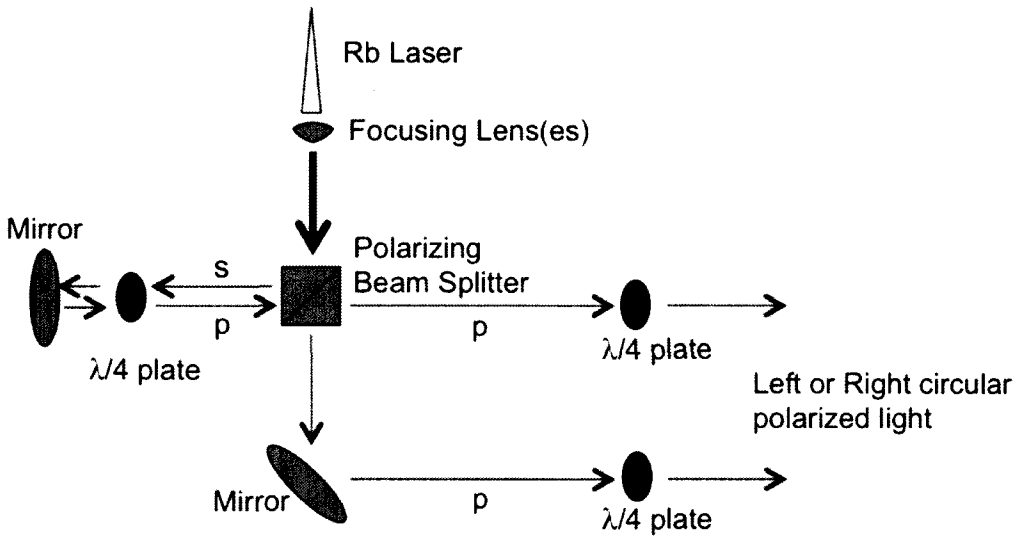

FIG. 4.4: Optics to create right-circular polarized light.

The light is first collimated so that it is easier to work with over relatively long distances (focusing lenses). From there, it passes through a linear polarizing beam splitter. The P-waves will pass straight though the splitter, while the S-waves are reflected 90° (in reality, a very small amount of P-wave also gets reflected). The reflected S-waves pass through a $\lambda/4$ plate, are reflected by a mirror, and finally travel again through the $\lambda/4$ plate. This process creates a half-wavelength phase shift of the S-wave, turning it into a P-wave. It will then continue on through the beam splitter undeflected (however, that small amount of P-wave mentioned above that was deflected with the S-wave is now S-wave itself, and will be reflected back toward the laser. For this reason, it is important that the optics alignment be near-perfect, but not perfect (otherwise there is risk of burning the laser fiber). All of the laser light traveling toward the ^{3}He-alkali mixture is now P-wave. A final pass through a $\lambda/4$ plate will circularly polarize the light.

E07-013 implemented 5 lasers, all of which were united via a 5:1 optical combiner.

Each laser provided ~25 Watts of power. After some loss due to optics, the total power was just over ~100W. Two of these lasers were broadband lasers as used in past ^{3}He experiments. They have wavelengths centered at 795 ± 2nm. The remaining three were narrow-band lasers with central wavelength 795 ± 0.2 nm. The benefit of using the narrow-band lasers is two-fold [48]. First, it greatly increases the optical-pumping rate of Rb. Recall Equation 4.24:

$$R_p = \int \Psi(\nu)\sigma(\nu)d\nu \tag{4.24}$$

The photon flux, $\psi(\nu)$, is described on the left of Figure 4.5. The absorption cross-section, $\sigma(\nu)$, is shown on the right. Clearly, the line shape of the narrow band laser (red) is a much better match to the D1 absorption cross-section of the Rb than the broadband laser (blue). The result is a higher pumping rate [48].

Additionally, one can take advantage of the shape of the Rb polarization gradient along the laser light's propagation path (Figure 4.6). If the pumping chamber for Rb is short enough such that its end is reached before the 'sharp transition,' the Rb polarization will be near unity along the entire light path. The use of hybrid alkali metals and narrow-band pumping lasers are by far the two most significant advances in polarized ^{3}He cell technology in recent years. Early ^{3}He experiments at JLab reached polarizations of <40% using broadband lasers and pure Rb alkali [31, 41, 42, 49].

In 2006 JLab E02-013 used hybrid cells to achieve polarizations of near 50% [17] - a world record at the time. The most recent group of ^{3}He experiments (including E07-013) obtained maximum in-beam polarization of greater than 60%, setting a new standard for polarization levels.

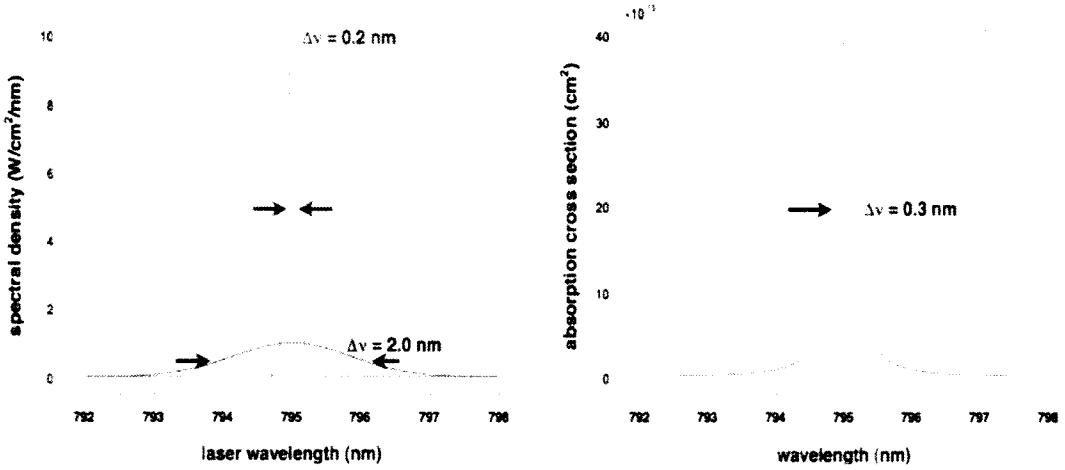

FIG. 4.5: LEFT: Spectral density vs. wavelength for two types of lasers. Blue is the line width of broadband lasers. Red is narrow band. RIGHT: Absorption cross-section for Rb vs. wavelength.

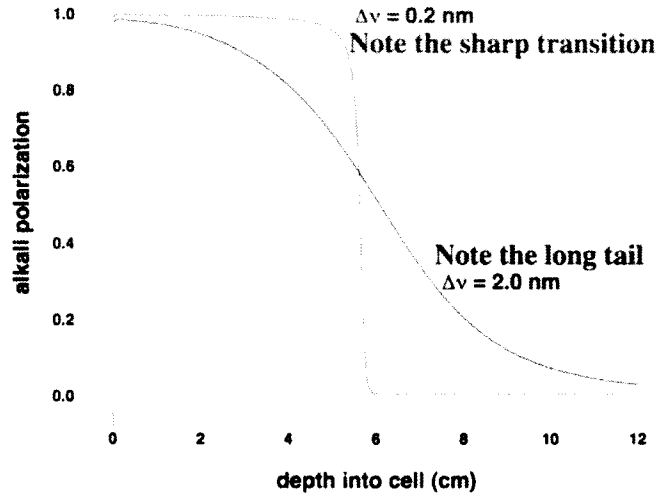

FIG. 4.6: Rb polarization gradient as a function of depth into 3He cell.

4.2 The ^{3}He Target Cell

4.2.1 The Creation of a ^{3}He Cell

We now know all the necessary ingredients needed to create a polarized ^{3}He target cell. They are: ^{3}He gas, an alkali mixture of Rb and K vapor, a small amount of N_2 and circularly polarized laser light. The next step is to find an appropriate container to accommodate all of these pieces. Scattering experiments such as E07-013 set specific constraints on the container. First, the material used must contain as little paramagnetic material as possible. Also, for statistics-driven experiments it is desirable to have a very dense (and thus high pressure) target. However, the container should have very thin walls, as excess material will inevitably lead to a high background rate. Thus, an appropriate balance must be found between cell-wall thickness and ^{3}He gas pressure. Finally, the porosity of the material to ^{3}He should be very low. A container that leaks ^{3}He gas will not only have a short useful lifetime, but also introduce difficult corrections due to a non-constant target density. The material that best satisfies all of these prerequisites is GE 180 aluminosilicate glass.

The nature of a counting experiment as well as the ^{3}He polarization process also sets strict requirements on the shape of the target cell. There must be an area designated for pumping the alkali metal and polarization (pumping chamber) and an area for scattering the electron beam (scattering chamber). The pumping chamber should have a cross-sectional area to match the shape and diameter of the incoming laser light (for E07-013, D=3"). Likewise, the scattering chamber should be made to accommodate the incoming electron beam. It should be long enough (length = 40 cm for E07-013) to provide the electron beam sufficient scattering length, and only wide enough to allow for

usual beam rastering - any wider would only be a waste of materials and increase radiative corrections. The two chambers should be connected via a tube that allows the transfer of polarized ^{3}He from the pumping region to the scattering region. The glass at where the electron beam enters and exits should be as thin as possible to reduce background. Figure 4.7 shows a cell that satisfies all of these requirements.

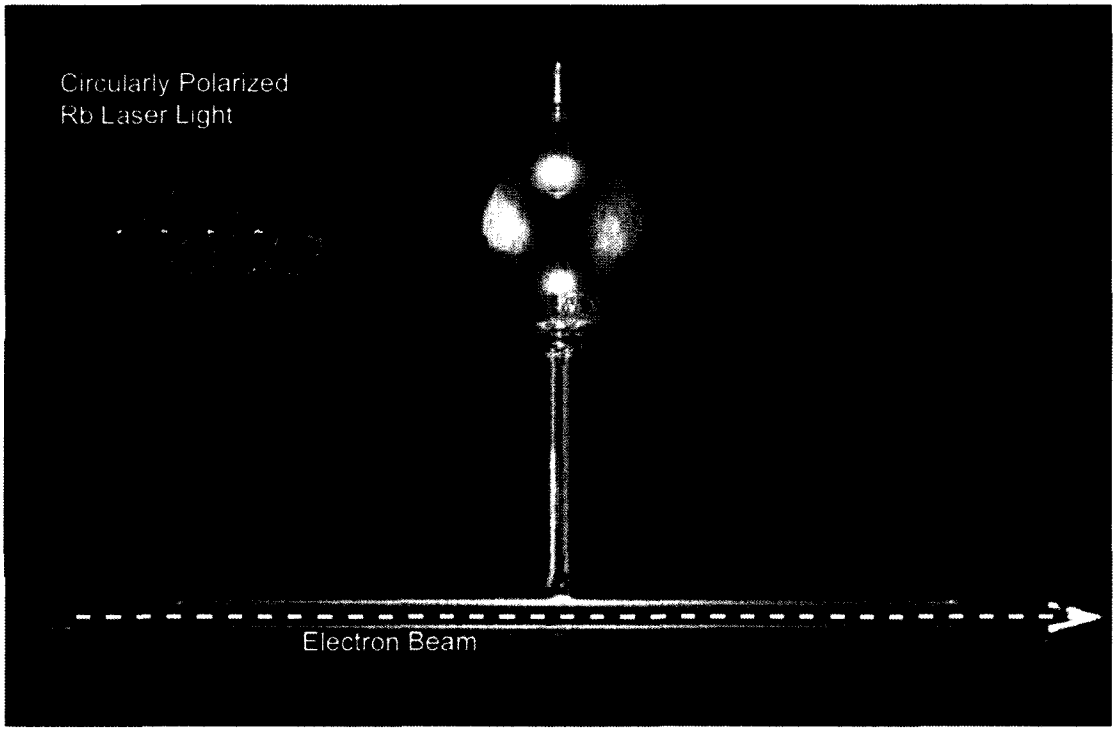

FIG. 4.7: A typical ^{3}He cell, including the pull-off, pumping chamber, transfer tube, scattering chamber and thin end-windows.

The 'pull-off' in the picture is not a geometric requirement of the experiment or polarization procedure, but rather a byproduct of the cell filling process. Each ^{3}He cell is originally part of a glass 'string' (see Figure 4.8). The string is connected to a series of valves and pipes that are under vacuum. ^{3}He and N_2 gas are flowed through the system and enter the cell via the pull-off area. The alkali, on the other hand, exists in the retort

at the end of the string and is chased into the pumping chamber. Finally, the pull-off is heated and the cell is removed from the string. An in-depth discussion on filling a ^{3}He cell can be found in [50] .

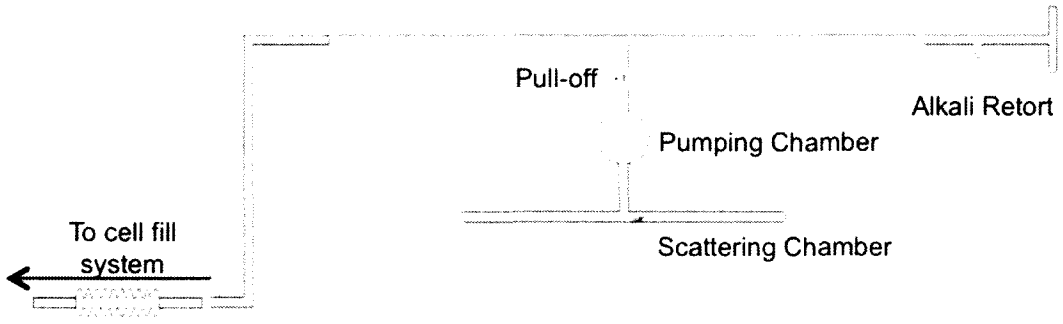

FIG. 4.8: A ^{3}He cell before being removed from the string.

4.2.2 Target Cell Properties

Once a new ^{3}He cell is in hand, it is very important to measure certain properties that are unique to each cell. In order to later make corrections to the data, one must precisely know the target density as well as the thickness of the glass at several points along the scattering chamber. Further, during the experiment one must monitor the temperature of the ^{3}He cell as fluctuations will cause a change in target density.

Cell Wall Thickness

It is important to know all the dimensions of the cell for a complete data analysis. These will affect things such as background rate, polarization transfer from pumping to scattering chamber and even polarimetry (since the volume of the cell between pick-up

coils decides the amount of material between the coils). Several of these characteristics, such as chamber dimensions, can be determined simply by careful measurement with a caliper. Obviously, measurement of the cell wall thickness, t_w, cannot be made in this way, and instead were made using laser interferometry.

The laser interferometry measurement is performed using a narrow-band laser of finely tunable wavelength. The laser is first split into two lines (refer to Figure 4.9). One is used to precisely measure the wavelength of the light. The second is sent through an optical chopper so that the remaining electronic components in the system can be sure to separate signal from background. Once chopped, the light is again split into two lines. One of these is sent to a lock-in amplifier. The final line of light is directed at the cell wall. Its reflection is received by a photodiode.

The intensity of light reflected from a flat surface is given by [50]:

$$I_r = \frac{\eta}{1-\eta} I_0 \tag{4.25}$$

where

$$\eta = \frac{4\left(\frac{n-1}{n+1}\right)^2}{1-\left(\frac{n-1}{n+1}\right)^2} \sin^2\left(\frac{2\pi n t_w \cos\theta}{\lambda}\right). \tag{4.26}$$

Here, n is the index of refraction, λ is the wavelength of the laser, θ is the angle of the reflection and t_w is the thickness of the surface. Measurements were made several places along the length of the target, as the nature of glass blowing leads to inconsistencies in thickness throughout the cell.

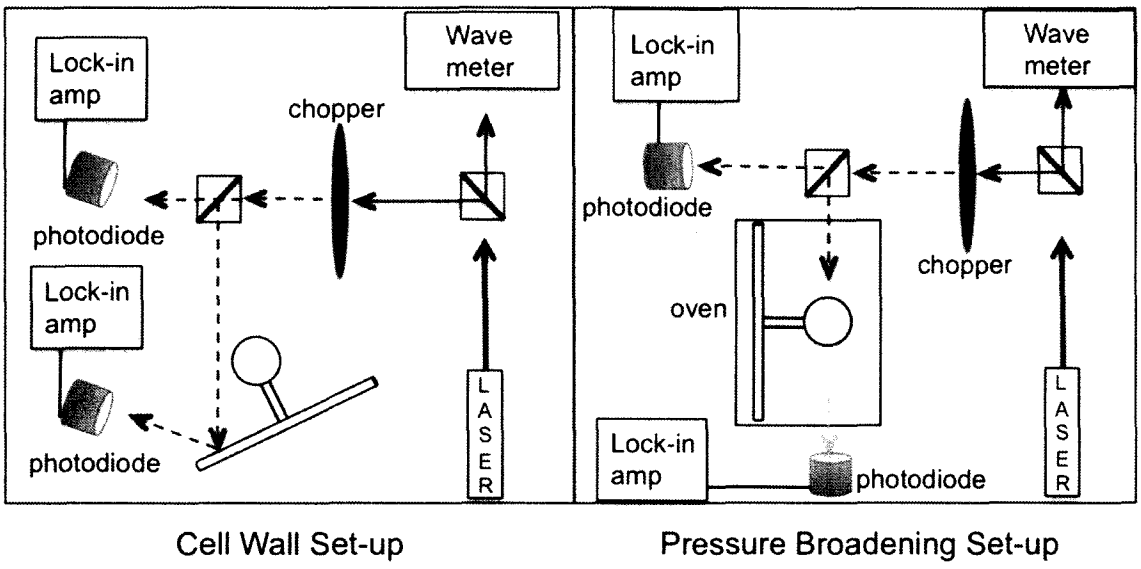

FIG. 4.9: Set-up for cell wall thickness and pressure broadening measurements.

Target Density Measurements

Every aspect of a cell-fill is recorded in detail so as to retain as much knowledge of cell characteristics as possible, in particular, the density of the gas that is inserted into a cell. However, there are always uncertainties (precise temperatures during certain aspects of the cell fill, for one) that propagate uncertainty to the final calculated 'fill-density' of the ^{3}He cell. For this reason, it is necessary to find a more accurate method to measure cell density. This method is called 'pressure broadening,' and exploits the broadening of Rb absorption lines due to collision with the ^{3}He atoms.

In an ideal world, the absorption spectrum of an atom would consist of several delta function peaks, with each peak corresponding to a particular allowable energy transition. In practice, a measurement of this spectrum does not reveal delta spikes, but rather a smearing of the peaks about or near their expected central value. This broadening/shifting

of the spectral line shape can be due to several effects, depending on the system being considered. For instance, a sample can experience 'Doppler broadening,' which is due to thermal motion of the sample. A particle moving toward a photon with *nearly* the correct energy to cause excitation may 'see' the photon as actually *having* the correct energy due to a Doppler shift.

Density measurements on a ^{3}He cell depend on pressure broadening, which is much more predominant than, say, Doppler broadening [51]. In pressure broadening, the spectral change is due to the collision of nearby atoms with those which are absorbing/emitting photons. These collisions cause a deformation in the emitting particle, which in turn will perturb the energy levels of the particle and thus shift the frequency of the photons it emits. This effect depends on both the pressure and temperature of the gas, and thus the temperature of the sample must be carefully monitored throughout the measurement.

The procedure is as follows. First, the ^{3}He cell is placed in an oven and heated such that the Rb is vaporized. The optics line begins with a narrow-band laser which is passed through a beam splitter. One of the lines is used to precisely monitor the wavelength (frequency) of the laser. The second is sent through an optical chopper. Chopping the laser at a known frequency ensures that all of the electronics involved can separate signal from noise. The chopped beam is again split. One of these lines are fed to a photo-diode, then a lock-in amplifier. The second is passed through a window in the oven and sent through the pumping chamber of the cell. A photodiode resides on the opposite end of the oven, and receives the laser light which is not absorbed by the cell.

The wavelength is then swept through the D1 resonance of ^{85}Rb (795 nm). The absorption spectrum is plotted as a function of frequency, as in Figure 4.10. The shape of

the broadening, S_{PB}, has the form of a Lorentzian:

$$S_{PB}(\nu) = \frac{A[1 + 0.6642 \cdot 2\pi T_d(\nu - \nu_c)]}{(\nu - \nu_c)^2 + (\gamma/2)^2} + B \tag{4.27}$$

where A and B are fit parameters, T_d is the collision time, ν is the frequency of laser light, and ν_c is the usual central value of the resonance. γ is the FWHM of the signal, which is the goal of the measurement. An in-depth study on extracting the cell density from the line width can be found in [51].

The sinusoidal background in the signal is due to an 'etalon' effect. This is caused by the laser interfering with its own reflection as it passes through windows of the oven or the cell. The shape can easily be fit and removed without consequence.

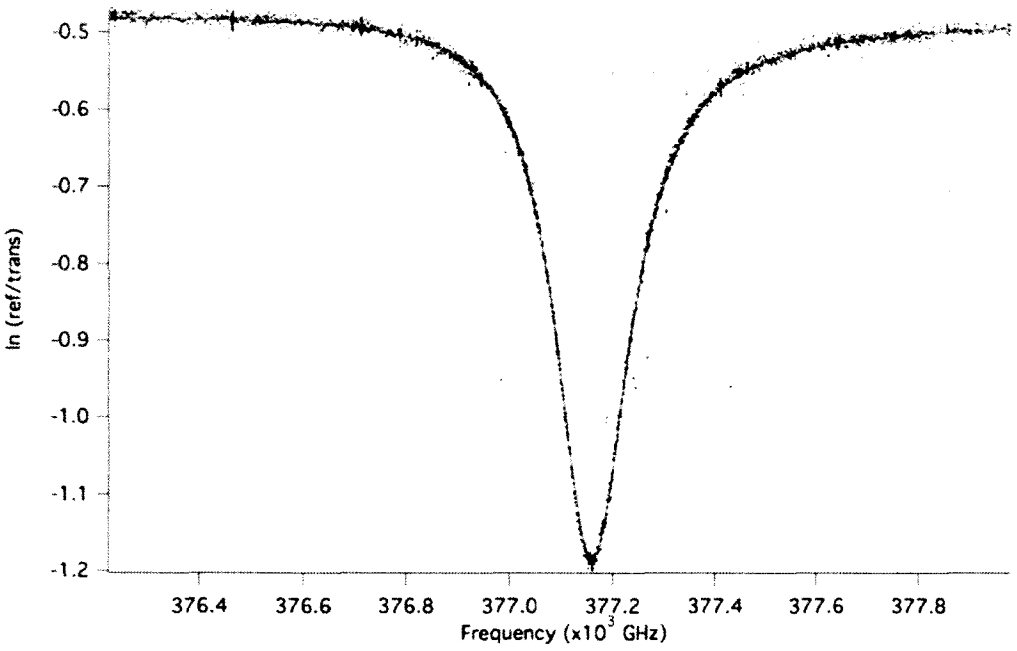

FIG. 4.10: Results of a typical pressure broadening scan. The signal is fit to a Lorentzian shape to extract the cell density.

4.3 The ^{3}He Target Set-Up

A schematic of E07-013's polarized ^{3}He set-up is shown in Figure 4.11. During E07-013, the target system was capable of polarization in x, y and z directions. For sake of clarity, only the z direction is shown in the figure. The target cell is mounted in the system such that the pumping chamber is contained in an oven and the scattering chamber is exposed. In order to vaporize both the Rb and K alkali, the oven is heated to $\sim 230^\circ$ C, which is achieved by flowing hot air through an inlet tube. The oven is centered in a pair of Helmoltz coils (red) which create a uniform 'holding field,' whose purpose is to maintain the direction of ^{3}He spins. Another set of Helmoltz coils (green) are used to generate an oscillating RF field. This is used to flip the spin direction of the ^{3}He atoms. Laser light is transported from the laser room (not shown) via several optical fibers and is directed through the aforementioned polarizing optics. It is then guided by a series of polarization preserving mirrors through an oven-window and finally arrives at the pumping chamber. An 'EPR' coil that is used for polarimetry is mounted inside the oven, just above the pumping chamber. A photodiode, also for EPR, looks through an oven window. Finally, there is a pair of 'pick-up' coils into which the target scattering chamber can be lowered. These are used for a second form of polarimetry. Due to geometric constraints, pick-up coils for scattering chamber polarimetry only exist in one direction. However, there are also pick-up coils mounted on the oven that can perform polarimetry on the pumping chamber.

Several aspects of the target set-up have been modified from previous designs, making this the most versatile ^{3}He target system ever used. E07-013 is the first Jefferson Lab ^{3}He experiment to use a vertically polarized target, and the first to allow for polarization in x, y and z directions. For this to be possible, the oven design from previous experi-

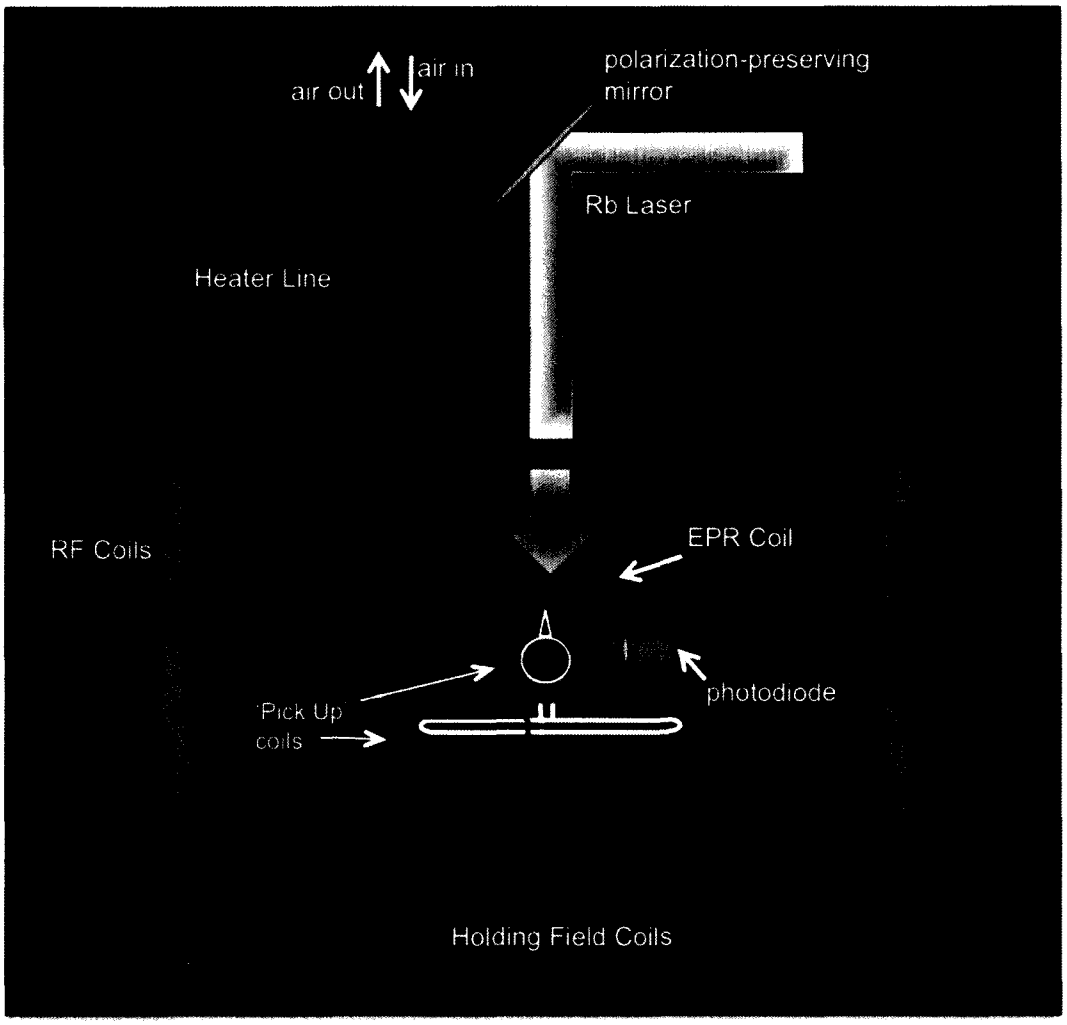

FIG. 4.11: Schematic of the polarized ^{3}He target system. Only the vertical pumping direction is shown for clarity.

ments had to be completely overhauled. The setup is also the first to mount the EPR coil inside the oven - not a trivial task due to high temperatures and geometric limitations - which makes the EPR signal much stronger. In addition to the usual NMR pick-up coils positioned around the scattering chamber, there are 3 sets of coils mounted on the oven surrounding the pumping chamber. This allows for polarimetry with every spin flip, regardless of spin orientation and without the need to move the target from the in-beam position.

4.3.1 Target Oven

In order to expand the ^{3}He setup to include a third polarization direction the oven had to undergo several modifications. The most obvious change is that yet another optics line must have an entrance to reach the pumping chamber of the cell. An added complication to this is that the pumping laser light cannot hit the pull-off of the cell. This would cause the pull-off to heat up, and could possibly lead to cell rupture. The problem was solved by shifting the pull-off by $\sim$ 42 degrees from its usual position and rotating the cell by the same angle in the oven. Further, since x, y and z directions around the cell must be kept clear to allow the passage of laser light, the oven had to be expanded to account for heating-system airflow.

The combination of high operating temperatures along with the off-center support of the oven rendered the materials used for past ovens insufficient. Instead, a new material would have to be used. Requirements were that it be lightweight, non-magnetic and able to sustain high temperatures. It must also be rigid and have a very low rate of expansion at the target operating temperatures, otherwise the precision of the target cell position would not be met. The material that best fits this description is ceramic-glass mica. Even after

changing the material, a supplementary support system had to be designed to share some of the oven weight.

4.3.2 Target Ladder

Data runs during E07-013 can be classified into two broad categories: production mode and test runs. Production mode implies a ^{3}He target with normal beam conditions. The majority of data is collected in production mode. However, several calibration tests must be run, and they usually require targets other than ^{3}He. The other targets where mounted on the target ladder, which hung below the ^{3}He oven (see Figure 4.12). The ladder consists of a row of seven carbon foils, a reference cell and an empty position that gave the electron beam a straight path to the beam dump. The carbon foils are mainly used as a means of calibrating spectrometer optics. A small piece of beryllium oxide is mounted in front of the carbon and is used for alignment of the electron beam.

The reference cell is an empty glass cell with the (nearly) identical shape and same material as the ^{3}He target chamber. The cell is connected to a gas handling system so that it can be filled with a desired gas or evacuated at the appropriate times. The available gasses were N_2, H_2 and unpolarized ^{3}He. They were used to determine nitrogen dilution, proton cross-section and elastic ^{3}He cross-section respectively.

4.4 Polarimetry

The preceding sections have laid out the means by which E07-013 achieved very high polarization levels throughout the duration of the experiment. It is, however, insufficient to only attain these polarizations - one must also find ways to accurately measure

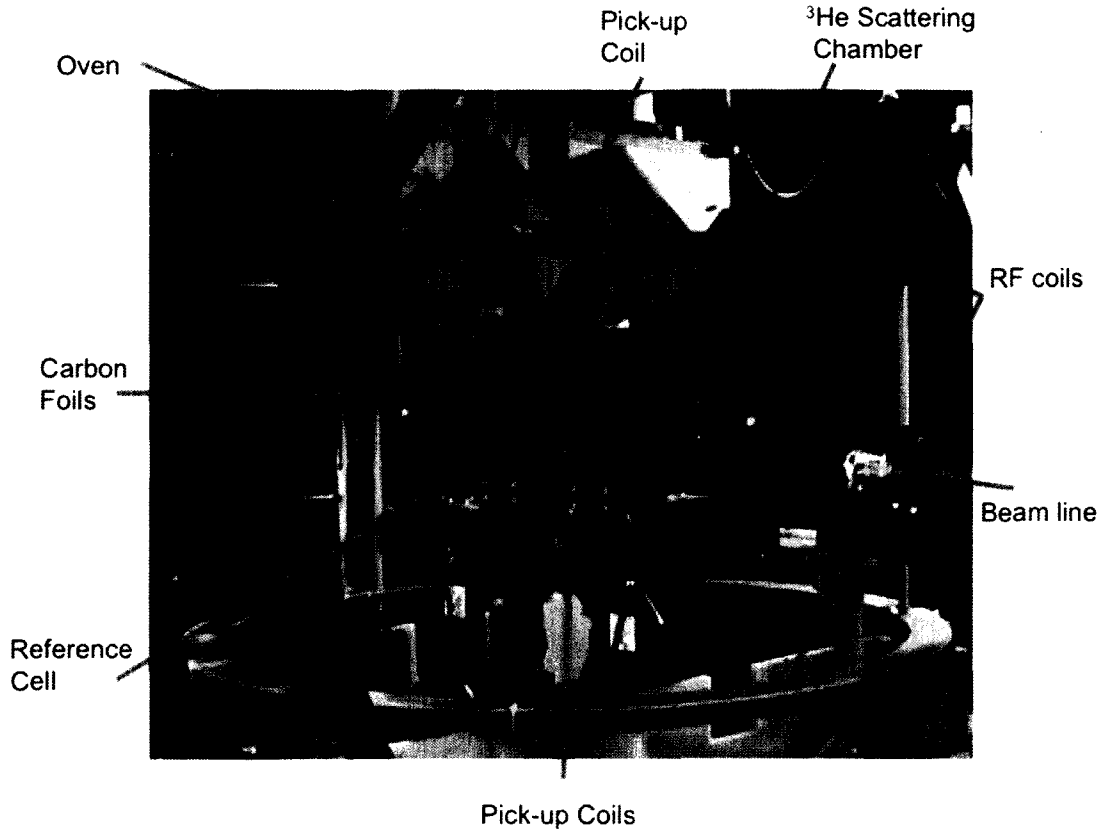

FIG. 4.12: Close up photograph of JLab's Hall A polarized ^{3}He target system.

the target polarization such that the polarization uncertainty does not dominate the error budget. Ideally, a polarimetry measurement would sample each individual atom within the target cell, and average over all samples:

$$\vec{P}_{target} = \frac{1}{N} \sum \vec{P}^i_{nucleus} \tag{4.28}$$

where N is the total number of ^{3}He nuclei in the cell. Of course, there is no way to actually examine each individual nucleus. Instead, one must find a measurable quantity that

is related to the summation in Equation 4.28. E07-013 used two types of polarimetry to do this. They are Nuclear Magnetic Resonance (NMR) and Electron Paramagnetic Resonance (EPR). Each utilizes a spin-reversal technique called Adiabatic Fast Passage (AFP) which minimizes polarization loss. While NMR is the easiest to perform in practice, its downfall is that it is not a direct measurement of ^{3}He polarization and therefore must be calibrated by a material with well-known polarization properties (usually water). EPR is more difficult in practice, but is a direct measurement of polarization.

4.4.1 Nuclear Magnetic Resonance and Adiabatic Fast Passage

Perhaps the most revealing equation one can consider in discussing NMR is Faraday's law,

$$\text{emf} = \frac{d\Phi_B}{dt} \tag{4.29}$$

which states that a changing magnetic flux through a closed circuit will induce an electromotive force in that circuit. This law is employed in ^{3}He polarimetry by flipping the collective spins (a magnetic field) of the ^{3}He nuclei and recording a signal in a nearby set of pick-up coils. The flipping of spins is accomplished using AFP.

A ^{3}He atom with spin $\vec{I}$ has a magnetic moment $\vec{M} = \gamma\vec{I}$, where γ is the gyromagnetic ratio ($\gamma_{^3He} = 3.243$ kHz/G)[42]. When this atom is placed in a magnetic field (in this case, the previously mentioned 'holding field'), the magnetic moment will experience a torque [52]:

$$\frac{d\vec{M}}{dt} = \gamma\vec{M} \times \vec{H}_0. \tag{4.30}$$

This produces a precession of $\vec{M}$ about of $\vec{H}_0$.

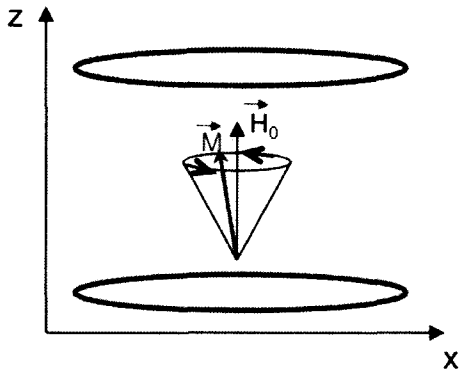

FIG. 4.13: Precession of $\vec{M}$ about the holding field $\vec{H}_0$. The red circles represent one set of Helmoltz coils used to create $\vec{H}_0$.

It will prove convenient to change to a rotating coordinate system which will precess in tandem with the magnetic moment. Vector $\vec{M}$ can then be re-written as

$$\frac{d\vec{M}}{dt} = \frac{\partial \vec{M}}{\partial t} + \vec{\omega} \times \vec{M} \tag{4.31}$$

where $\partial\vec{M}/\partial t$ is the motion of $\vec{M}$ in the rotating coordinate system and $\vec{\omega}$ is the frequency of precession. Substituting Equation 4.31 into 4.30 yields

$$\frac{\partial \vec{M}}{\partial t} = \gamma \vec{M} \times \left(\vec{H}_0 + \frac{\vec{\omega}}{\gamma} \right). \tag{4.32}$$

The extra term in Equation 4.32, $\vec{\omega}/\gamma$, can be thought of as a 'fictitious' magnetic field that arose when changing to a rotating coordinate system (the magnetic analog to the Coriolis effect). Clearly, if the precession rate of the magnetic moment is opposite that of the rotating coordinate system, i.e. $\vec{H}_0 = -\vec{\omega}/\gamma$, then $\partial\vec{M}/\partial t$ will be zero. This means that in the rotating frame, the motion of the magnetic moment has vanished. Viewed from the

lab frame, this magnetic moment is rotating at what is defined as the Larmour frequency:

$$\omega_L = -\gamma H_0. \tag{4.33}$$

As of now, the discussion has mentioned only one external magnetic field - the holding field H_0. The AFP process requires that another external field be introduced. This is an oscillating 'RF field,' which is generated perpendicular to H_0. Figure 4.14 describes what the RF field looks like as time passes.

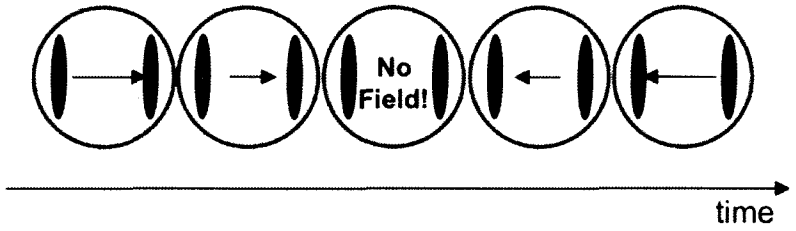

FIG. 4.14: RF field vs. time. The red circle represents the same set of coils as in Figure 4.11. The green coils are the RF generating coils. The pattern repeats as time passes.

This RF field can be viewed as two counter rotating fields, as in Figure 4.15. The

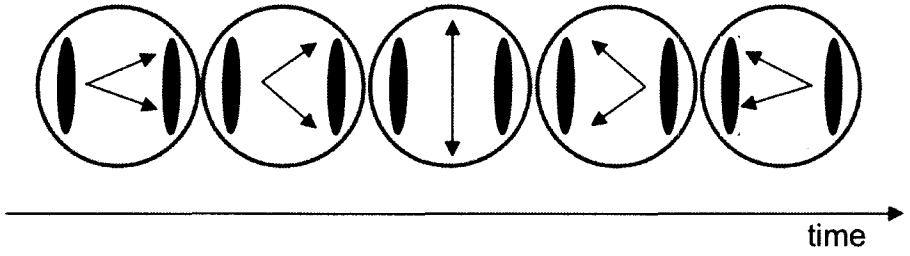

FIG. 4.15: RF field vs. time, viewed as two counter-rotating fields. The sum of the two vectors is equal to those shown in Figure 4.14.

'effective' field seen by the magnetic moment now has an x-component in addition to the

original z-component created by the holding field. The effective magnetic field can now be written as seen by the dipole, but with the RF field turned on:

$$\vec{H}_{eff} = \left(\vec{H}_0 + \frac{\omega}{\gamma}\right)\hat{z} + \vec{H}_1\hat{x}' \tag{4.34}$$

where $\hat{x}'$ is the x-axis in the rotating coordinate system and $\vec{H}_1$ represents one component of the magnetic field which is rotating. It can be shown that the other component of the oscillating field is negligible [53]. The resulting precession about $\vec{H}_{eff}$ will appear as in Figure 4.16.

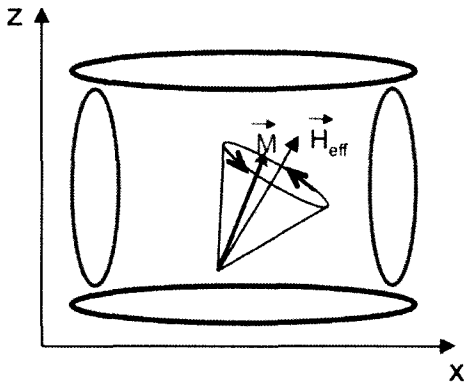

FIG. 4.16: $\vec{M}$ precessing about $\vec{H}_{eff}$ as seen in the rotating coordinate system.

Let $\omega_1 = -\gamma\vec{H}_1$. Then the angle between $\vec{H}_{eff}$ and $\vec{H}_0$ is given by

$$\tan\theta = \frac{\vec{H}_1}{\vec{H}_0 + (\omega/\gamma)} = \frac{\omega_1}{\omega_L - \omega} \tag{4.35}$$

$$\sin\theta = \frac{H_1}{H_{eff}} = \frac{\omega_1}{-\gamma H_{eff}}; \qquad \cos\theta = \frac{\omega_L - \omega}{-\gamma H_{eff}}$$

If $\vec{H}_1 \ll \vec{H}_0$, then θ will be very small. However, as $|\vec{H}_1|$ approaches $|\vec{H}_0|$, i.e. $|\omega - \omega_L| \approx$

$|\omega_1|$, a resonance condition is reached. It is now clear how to flip the spins of the ^{3}He atoms. The $\vec{H}_0$ field is swept from 25 G to 32 G through the resonance $\vec{\omega} = \vec{\omega}_L/$ (for ^{3}He, $\vec{\omega}_L/\gamma = 28.06$ G). The ^{3}He spins will follow the effective field as long as the adiabatic condition is satisfied:

$$\frac{1}{T_1} \ll \frac{1}{H_1}\frac{dH_0}{dt} \ll \gamma H_1 \tag{4.36}$$

where $T_1 \approx 435$ s is the relaxation rate of ^{3}He in the rotating coordinate system. Typically, $H_1 \approx 91$ mG. In short, the adiabatic condition requires that the sweep be slow enough that the spins can follow the magnetic field, but faster than the relaxation time of the spins. An AFP flip can also be performed by sweeping the RF field through resonance as the holding field is held constant.

As of yet, still nothing has been said about an actual polarization measurement. This is done by positioning a set of 'pick-up' coils near the target. They should be placed perpendicular to both the holding field and RF field. When the ^{3}He spins reach resonance, $\vec{H}_0 = \vec{\omega}_L/\gamma$, they will induce an electromotive force (EMF) in the pick-up coils. The amplitude of this signal is proportional to the component of ^{3}He magnetization, M_T, that is transverse to $\vec{H}_0$ [31]:

$$S(t) = M_T \frac{\left(\vec{H}_{eff}\right)_{\perp}}{|\vec{H}_{eff}|} = \frac{M_T H_1}{\sqrt{\left(H\left(t\right) - H_0\right)^2 + H_1^2}} \tag{4.37}$$

and $H(t)$ is

$$H(t) = \begin{cases} \alpha t + \beta & : t < t_{sweep} \\ \beta - \alpha t & : t_{sweep} < t < 2t_{sweep} \end{cases} \tag{4.38}$$

Here, $\alpha = 2$ G/s is the sweep rate, $\beta = 25$ G is the initial $\vec{H}_0$ and $t_{sweep} = 4$ s is the length of the sweep. The polarization of ^{3}He is related to the signal S(t) as

$$P_{^3He} = \kappa_{NMR} S_{^3He}. \tag{4.39}$$

Physical properties of the cell and coils, as well as their positions, determine the constant of proportionality, κ_{NMR} [54]. A typical NMR measurement during E07-013 is shown in Figure 4.17.

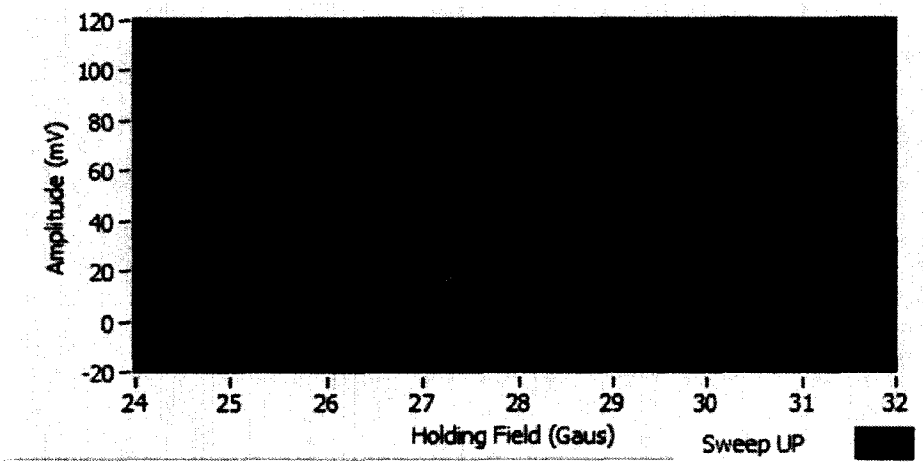

FIG. 4.17: A typical AFP NMR spectrum.

Rapid Spin Flip and AFP Loss

One way of calculating a target single-spin asymmetry (SSA) would be to accumulate data in one target state for half of the experiment, flip the target spin, and then collect data on the other target state for the remainder of the experiment. This, however, can lead to false asymmetries. If, for instance, the ^{3}He cell had a very slow leak, the data at the beginning of the experiment would be collected from a target of higher density than that at the end of the experiment. This would clearly affect the scattering cross-sections that are eventually used to form the SSA. It is then desirable to make several flips of the target spin, reducing the amount of time that the system has to undergo unintended evolutions. In the limit that the time between spin flips, Δt_{flip}, goes to zero, any systematic effects should as well. E07-013 was the first ^{3}He experiment at Jefferson Lab to implement a 'rapid spin-flip' process.

Unfortunately, there is a definite loss of polarization that is intrinsic to the AFP spin-fip process (called 'AFP loss'). If Δt_{flip} is too short, the SEOP process will not have enough recovery time to counter this loss in polarization. As the number of flips, N_{flips} becomes large the polarization will be destroyed. One must find an appropriate Δt_{flip} such that an equilibrium between pumping rate and AFP loss is reached as $N_{flip} \rightarrow \infty$. A series of studies found Δt_{flip} to be optimized around $\Delta t_{flip} \approx 20$ min.

An added bonus of rapid spin-flip is that with each spin-flip, one can perform a polarimetry measurement. Pick-up coils positioned on the oven (see Figure 4.11) were used to receive an NMR signal from the pumping chamber of the ^{3}He cell. Of course, these measurements must somehow be extended to the scattering chamber. Since pick-up coils for both the scattering and pumping chamber existed for the longitudinal pumping direction, the appropriate corrections could be made.

Water Callibration

As mentioned above, NMR is not a direct measurement of ^{3}He polarization and requires calibration. One method of calibration would be to use EPR measurements - a direct form of polarimetry. However, if one wishes to use NMR and EPR as two independent methods of polarimetry, another calibration method must be used. Regardless of technique, the goal is to determine κ_{NMR} (Equation 4.39). The term is dependent on several factors including the responsiveness of the system, gains of electronics, the ^{3}He density between pick-up coils and the geometric flux produced by a particular cell [9]. Most of these are easily measured or already known properties of the cell. The purpose of water calibration is to determine the response of the system using a sample with well known polarization properties.

To perform water NMR, one should use a cell filled with water that has dimensions that are as similar to the ^{3}He cell as possible. The water cell is then mounted in the ^{3}He target system. The resonant field for water is $H_r = 21.27$ G, so the sweep of the field runs from $H_0 = 18$ G to $H_0 = 25$ G. Since the thermal polarization of water is very small, a summation of several sweeps (sometimes $N_{sweeps} > 1000$) is needed to increase the signal-to-noise ratio. The polarization of the water is

$$P_w = \chi H(t) \tag{4.40}$$

where $H(t)$ is the same as in Equation 4.38 and χ is the magnetic susceptibility of the proton, which is well known [50].

In order to extract the polarization of ^{3}He, one first relates the polarization of water,

P_w, and the water signal height, S_w:

$$c_w = \frac{P_w}{S_w} \frac{\mu_p n_p \Phi_{tot}}{\mu_{^3He}(\Phi_{pc} n_{pc} + \Phi_{tc} n_{tc} + \Phi_{tt} n_{tt})} \equiv \kappa_{NMR}. \tag{4.41}$$

The terms in 4.41 which have not been defined are parameters related to the magnetic flux through the pick-up coils and target density and are discussed in detail in [50]. The ^{3}He polarization can then be written as

$$P_{^3He} = c_w S_{^3He}. \tag{4.42}$$

4.4.2 Electron Paramagnetic Resonance

A second form of polarimetry was used during E07-013: electron paramagnetic resonance (EPR), which also implements the AFP spin-flip process. Recall the Hamiltonian for a Rb atom in a magnetic field (Equation 4.10):

$$H_{tot} = \frac{c_0}{n^2} + c_1(\vec{L} \cdot \vec{S}) + c_2(\vec{I} \cdot \vec{J}) + c_3(\vec{F} \cdot \vec{B}_{ext})$$

The final term indicates that an external magnetic field (such as the holding field, H_0) will cause a shift in energy level spacing (Zeeman effect). The corresponding energy shift is

$$\Delta E_{B_{ext}} = h\nu_0 \tag{4.43}$$

Certainly, the collection of polarized ^{3}He atoms in the target also constitute a magnetic field which is external to the Rb atom. Taking this into account, the resulting modified

Hamiltonian is

$$H_{tot} = \frac{c_0}{n^2} + c_1(\vec{L}\cdot\vec{S}) + c_2(\vec{I}\cdot\vec{J}) + c_3[\vec{F}\cdot(\vec{B}_{ext} + \delta\vec{B}_{^3He})] \tag{4.44}$$

where $\delta\vec{B}_{^3He}$ is the magnetic field of the ^{3}He atoms. The energy gap between levels is now

$$\Delta E_{B_{ext}\pm B_{^3He}} = h(\nu_0 \pm \nu_{^3He}) \equiv h\nu_{EPR}. \tag{4.45}$$

Here, $\pm$ indicates ^{3}He spins parallel or anti-parallel to the holding field. The shift, ν_{EPR}, is measurable quantity, and is directly proportional to the polarization level of ^{3}He. A measurement of ν_{EPR} with ^{3}He spins up ($\nu_\uparrow$), then down ($\nu_\downarrow$), will isolate the effect of polarized ^{3}He since $\nu_{^3He\uparrow} = -\nu_{^3He\downarrow}$(hence the usage of AFP spin-flip):

$$\nu_\uparrow - \nu_\downarrow = \nu_0 + \nu_{^3He\uparrow} - \nu_0 - \nu_{^3He\downarrow} = 2\nu_{^3He\uparrow} \tag{4.46}$$

Since the Rb is constantly under optical pumping, the majority of valence electrons are in the F=3, m=3 state (see Figure 4.2). By applying an RF field near the resonance of the F=3, m=3 $\rightarrow$ m=2 transition, the population of the two states will begin to equalize. The electrons in the F=3, m=2 state can again be excited to the $5P_{1/2}$ state, and, through collision mixing, the $5P_{3/2}$ state (Figure 4.3).

Most of these electrons will be radiationlessly quenched back to the $5S_{1/2}$ state, but a small fraction will decay by emitting a fluorescent photon. The emitted D1 light is saturated by the incoming pumping laser, and cannot be resolved. However, the D2 line ($\sim$ 780nm) is far enough from the laser wavelength that it can be detected by a nearby

photodiode. The EPR frequency is then determined to be the maximum of D2 intensity versus RF frequency. Figure 4.18 shows the frequency of the splitting as a function of time. The changes in frequency correspond to spin flips.

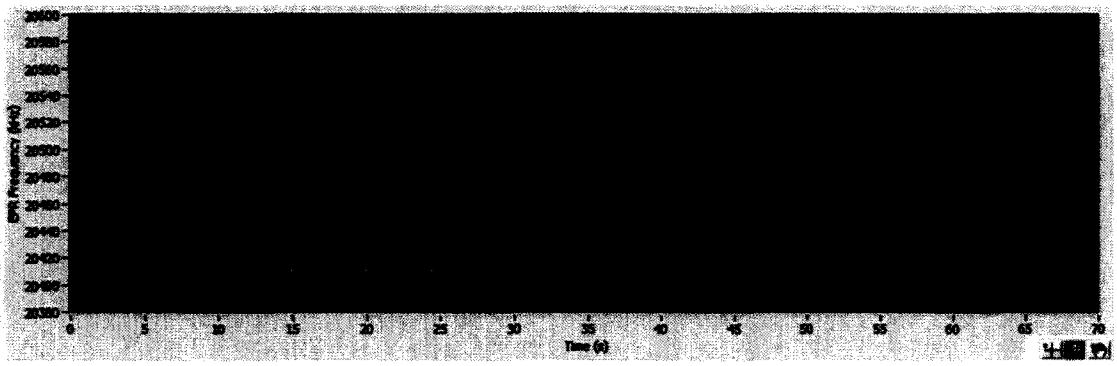

FIG. 4.18: A typical EPR measurement, which shows EPR frequency versus time.

The polarization of the ^{3}He is related to the frequency shift as [17]:

$$\Delta\nu_{EPR} = \frac{8\pi}{3}\frac{d\nu_{EPR}(F,m)}{dB}\kappa_0\mu_K P_{^3He} \tag{4.47}$$

where F and m are quantum numbers of the transition, B is the magnetic field, $\mu_{^3He}$ is the magnetic moment of the ^{3}He and $P_{^3He}$ is the average polarization of the ^{3}He. The term κ_0 depends on the temperature, T, of the sample, and has been experimentally determined [55].

$$\begin{aligned} \kappa_0^{Rb} &= 6.39 + 0.00914[T - 200(^\circ C)], \\ \kappa_0^{K} &= 5.99 + 0.0086[T - 200(^\circ C)], \end{aligned} \tag{4.48}$$

EPR with Hybrid Cells

A perhaps unexpected attribute of hybrid cells is that EPR may be performed using an atomic resonance of K despite the fact that it is not being optically pumped. Since the spin-exchange cross-section of Rb-K is extremely efficient, their polarizations can be considered equal [17]. An RF signal tuned to a K transition will cause depolarization, which in turn will lead to Rb depolarization. The Rb will then be optically pumped and again emit D2 light. The only advantage that Rb EPR has over K EPR is that κ_0^{Rb} is known to greater precision than κ_0^K [56].

Temperature Tests

Several aspects of the data analysis (for example $\rho_{^3He}$, κ_0 and κ_{NMR}) require precise knowledge of the temperature of ^{3}He in the cell. Resistive temperature detectors (RTDs) placed on the cell are used to monitor the temperature of both the pumping and scattering chamber. Because there will be a temperature gradient across the glass of the cell, these RTD readings will not precisely represent the temperature of the gas inside. Several temperature tests must be performed in order to determine the true internal temperature of the ^{3}He gas. These tests are being analyzed by Yi Zhang, a graduate student at Lanzhou University in China. Results are included in the analysis, but no write-up currently exists on the analysis procedure. Details will be available in his thesis.

4.5 The ^{3}He Target During E07-013

E07-013 made use of three different ^{3}He target cells, Astralweeks ('Astral' for short), Maureen and Brady. Astral and Brady were filled at UVa and Maureen was filled at

W&M. Several cell properties such as chamber volumes, fill density and lifetime are given in Table 4.1. All three cells were hybrids. Each cell had a 3" pumping chamber diameter and a target chamber diameter that was roughly 2 cm. The transfer tubes are typically between 5 and 6 cm in length.

Cell	Filled at	V_p (cm)	V_t (cm)	V_{tt} (cm)	Fill Density (amg)	Lifetime (hours)
Astralweeks	UVa	164.92	79.47	6.77	8.082	40
Maureen	W/M	180.75	89.05	4.15	7.23	26
Brady	UVa	169.27	74.57	5.98	7.87	31

TABLE 4.1: ^{3}He cells and their properties. V_p, V_t and V_{tt} are the volumes of the pumping chamber, target chamber and transfer tube, respectively.

4.5.1 Polarimetry Analysis

As mentioned earlier, there are two different methods of measuring polarization. EPR is a direct measurement, and NMR requires a calibration constant to convert the signal height to a polarization. E07-013 used EPR measurements to calibrate the NMR measurements. In this case, the calibration constant for NMR is simply defined as the ratio of the EPR polarization to the signal height of the NMR measurement. While it is possible to perform EPR using either Rb or K, E07-013 used only K. As a cross-check to the EPR calibration, two water NMR measurements were performed.

EPR Analysis

There are two ways in which the EPR signal can be converted to polarization, referred to as the direct method and the derivative method. Both methods were used for the analysis so as to have a cross-check. EPR analysis was performed by Chiranjib Dutta,

a graduate student at University of Kentucky. A brief summary of his work is discussed here. The full analysis procedure can be found in his thesis [12].

The direct method of polarimetry extraction makes use of the Breit-Rabi formula:

$$\nu_{\pm} = \left(\frac{g_S \mu_B}{-2} - \frac{1}{2} g_I \mu_N\right) \frac{B}{h} \pm \frac{\nu_h f_s}{2} \left[1 - \sqrt{1 \pm 2\left(\frac{2I-1}{[I]}\right) x + x^2}\right] \tag{4.49}$$

where the terms are defined in [48]:

$\nu_{\pm}$ = frequency where $\pm$ refers to the state $M_F = \pm(I + \frac{1}{2})$

g_S = electron g-factor = -2.002319304372

g_I = g-factor =+0.26097

μ_B = Bohr magneton = $9.27400095 \times 10^{-24}$ JT^{-1}

μ_N = magnetic moment = + 0.39146

$\nu_h f_s$ = ground state hyperfine splitting frequency = 461.719 MHz

B = holding field

x = $(g_I \nu_N - g_S \mu_B) \frac{B}{h \nu_h f_s}$

One can invert this equation and acquire the field as a function of frequency:

$$B(\nu) = \left(-b - s\sqrt{b^2 - 4c}\right)/2 \tag{4.50}$$

Here, s and c are coefficients defined in [12] and ν is the frequency of each target state in Figure 4.18. One can then define $\Delta B = B_1(\nu_1) - B_2(\nu_2)$, which can then be related to

the ^{3}He magnetization:

$$M_{^3He} = \frac{\Delta B}{(2/3)\mu_0 \kappa_0} \tag{4.51}$$

where μ_0 is the permiability of free space and κ_0 is the term dicussed in Section 4.4.2. The polarization can be extracted by:

$$P = \frac{M_{^3He}}{\rho \mu_{^3He}} \tag{4.52}$$

where P is the polarization, ρ is the density of ^{3}He in the cell and $\mu_{^3He} = 1.07^{-26}$ JT^{-1}.

The second method of extracting polarization from EPR is the derivative method.

$$P = \frac{\Delta \nu}{\frac{d\nu}{dB}\frac{8\pi}{3}\kappa_0 \mu_{^3He}\rho} \tag{4.53}$$

where $\Delta\nu = \nu_1 - \nu_2$ and the other terms are defined previously. The derivative of the frequency with respect to the field can be expressed as:

$$\frac{d\nu_{\pm}}{dB} = \frac{(g_I\mu_N - g_s\mu_B)^2}{h[I]} \sum_{n=0}^{5} b_n \frac{x^n}{[I]^n} \tag{4.54}$$

where $[I] = 2I + 1$ and b are coefficients of expansion which can be found in [12]. It is then straightforward to plug in these coefficients and calculate P.

Each NMR measurement was calibrated using the EPR analysis. To do this, the calibration constant had to be determined. Since spin flips are required to do EPR, one can also obtain NMR signals in the process. For the first flip during EPR, a polarization number is obtained. An NMR signal is recorded as well. One can then define the calibration

constant for this measurement as:

$$C_1 = \frac{P_1}{S_1} \tag{4.55}$$

where P_1 and S_1 are simply the EPR polarization and the NMR signal, respectively. Flipping the spin back to the original state gives a second measurement:

$$C_2 = \frac{P_2}{S_2}. \tag{4.56}$$

The final calibration constant is the average of C_1 and C_2.

$$C = \kappa_{NMR} = \frac{1}{2}\sum_{i=1}^{2} C_i \tag{4.57}$$

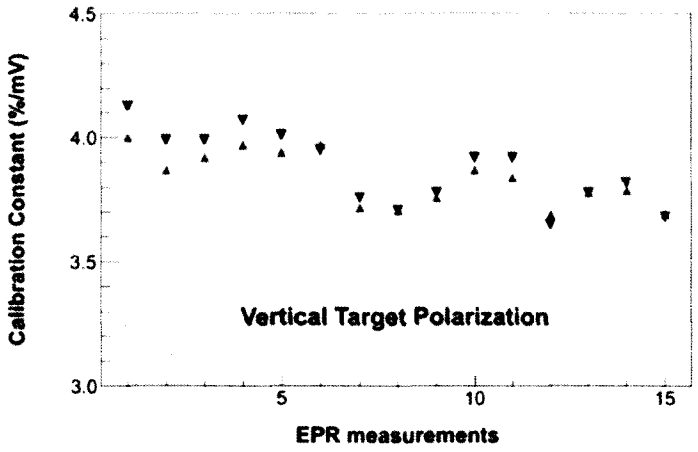

FIG. 4.19: Calibration constants for all EPR measurements during E07-013. Red triangles are constants from up sweeps and blue triangles are constants from down sweeps.

E07-013 as well as the Transversity experiment had record-setting target performance throughout the experiment. Figure 4.20 shows the target polarization versus run number for all 'good' vertical production data runs. The weighted average polarization over all runs was $\sim 62\%$.

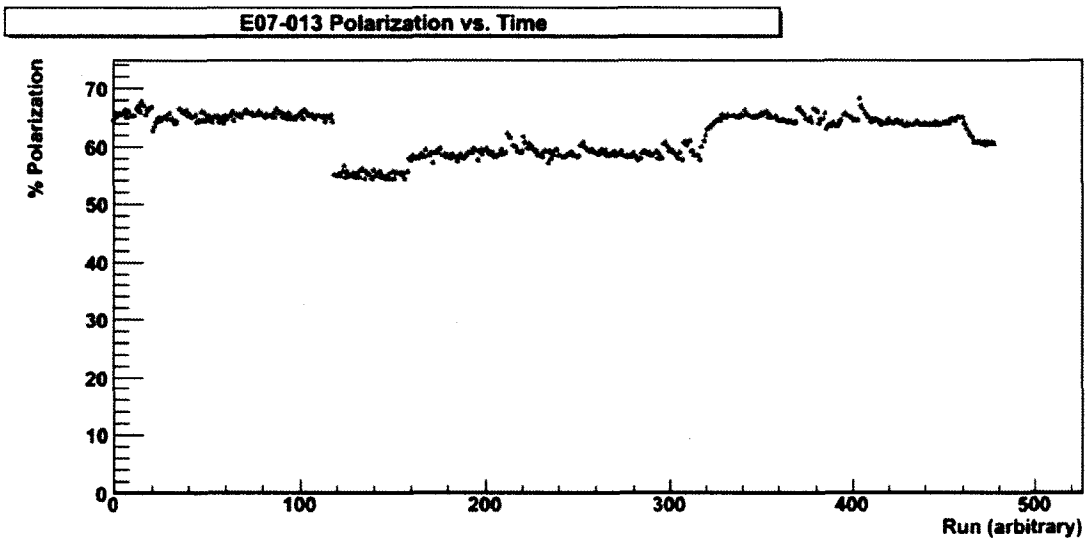

FIG. 4.20: ^{3}He target performance for vertical production data runs.

CHAPTER 5

Analysis

5.1 Analysis Procedure

The goal of this data analysis is to extract the target single-spin asymmetry, A_y^n, from $^3\mathrm{He}^\uparrow(e,e')$ deep-inelastic scattering. Ideally, this would consist of scattering an electron beam from a 100% polarized neutron target into a spectrometer with perfect particle identification and efficiency. Of course, this scenario is impossible to achieve, and so several corrections must be applied to the data in order to arrive at the desired physics result. A schematic of this process is shown in Figure 5.1. One begins by applying tracking and particle identification cuts to the raw data in order to obtain target-spin dependent electron counts, N^+ and N^-. These counts are then normalized to the accumulated charge and detector livetime in their respective target-spin states. These are referred to as 'yield' (Equation 5.10). The raw asymmetry is formed from these two numbers. Because the PID and tracking cuts are not 100% efficient, there is some amount of contamination within the final sample of electrons. A correction is made by estimating both the level of

contamination (defined in Equation 5.12) as well as the asymmetry of the contaminating particles. After these corrections, one has a 'raw electron asymmetry'. This asymmetry is then corrected further for target polarization and nitrogen dilution (to be discussed later in this chapter). The result of the above process gives the physics asymmetry from a polarized ^{3}He target. The remaining step is to use an appropriate model of the ^{3}He atom in order to extract the asymmetry's contribution due to a polarized neutron. Each of these steps will be discussed in detail in this chapter, followed by experimental results.

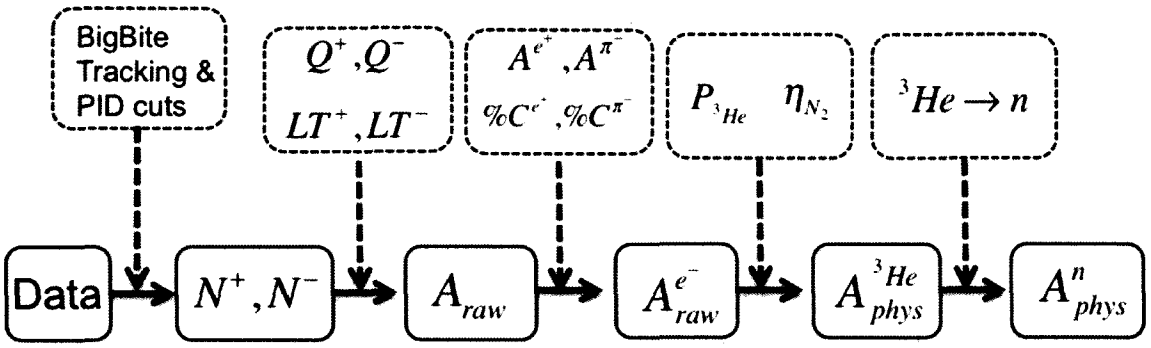

FIG. 5.1: Asymmetry analysis procedure. Symbols are defined in text throughout Chapter 5.

5.2 Particle Tracking and Identification

5.2.1 Quality Cuts

Before any attempt to discern electrons from other particles is begun, there are first several 'quality cuts' which are applied to the data. These are intended to remove portions of data which are problematic due to various issues while running, in particular, sudden drops in beam current and problems with beam steering and track reconstruction.

1.2.1a Trip Cuts

It is not uncommon for the beam current to drop to zero during a data run (called a 'beam trip'). The current then must be ramped back to the set value. While it is possible to properly normalize these data, it is quite difficult. Since this makes up only a small amount of the total data, these beam trip periods are simply cut out and thrown away. This is done in the first pass analysis by requiring the beam current be above some threshold in order to be considered quality data. Figure 5.2 shows a typical sample of beam delivered during normal data acquisition mode. The red data points represent quality beam, while black represents the removed beam trips.

Another possible problem occurs when there is a small deflection in the beam steering. If this deflection is great enough such that the beam scrapes the side of the target cell, a large shower of particles will saturate the wire chambers. The ensuing high currents in the chamber causes a trip in the wire chamber voltages. Portions of data which include these trips are excluded from the final set of analyzed data.

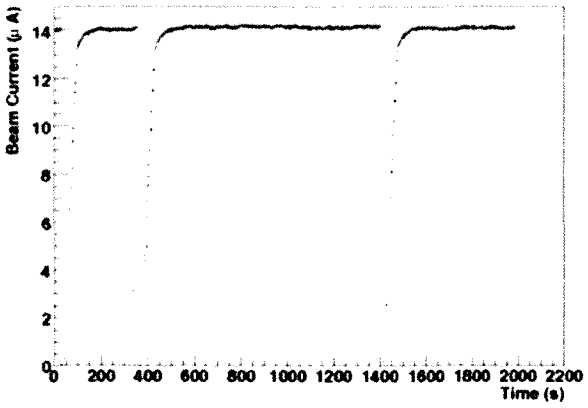

FIG. 5.2: Typical beam current vs. time during data acquisition. Black points represent a beam trip, and are excluded from the analysis.

1.2.1b Tracking Cuts

Below is a summary of the cuts which are applied in order to ensure a quality track has been reconstructed for each good electron event in BigBite.

Number of Tracks

The most obvious of these quality cuts is that it must be possible to reconstruct at least one track for the trigger. It is, in fact, possible for the tracking algorithm to find more than one track for a particle, given the enormous number of events that are passing through the wire chambers at any given time. In the case of several tracks being found, shower cluster information is used to choose the one which is most reasonable.

Geometric Cut

Because E07-013 is an inclusive measurement, it does not have the luxury of a coincident event to aid in the reduction of contamination. For this reason, the trigger threshold for this experiment (T6) was set higher than that of the Transversity experiment which it was parasitic to. However, it was recognized that several shower blocks at the top of the BigBite spectrometer still had a relatively low threshold due to electronics problems. As a consequence, this region of the detector was highly contaminated with low-energy pions, and thus was excluded from the data analysis. Further, all fringes of the BigBite detector were excluded. Since these areas have a much weaker magnetic field than the center of the magnet, track reconstruction is very poor in these regions.

Reconstructed Vertex

The tracking reconstruction algorithm will project the track of a particle back to its point of origin at the target area; this variable is referred to as $targetvz$. The entire 40 cm length of the target cell is visible to BigBite, so collimators were positioned to block the majority of scattering from the entrance and exit windows. Beyond this, a

cut on $targetvz$ is implemented to ensure that the detected electrons were scattered from the ^{3}He gas within the cell, rather than the target cell glass itself.

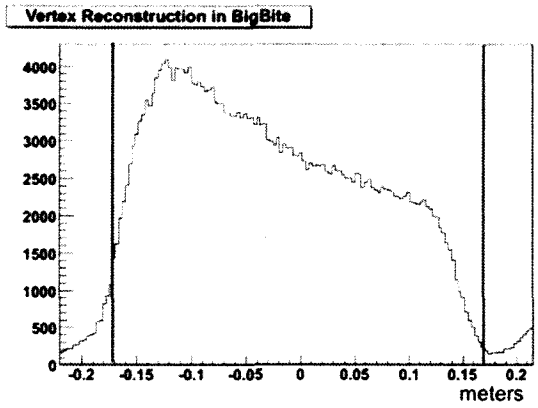

FIG. 5.3: BigBite reconstructed vertex (T6 events). Units on the x-axis are given in meters.

Track Match with Shower Cluster

Not only can a reconstructed track be projected back to the target, it can also be projected forward and be associated with a hit in the shower calorimeter. For each track, an appropriate cluster of energy deposition must be found in the calorimeter. The difference between the central position of the shower cluster and the projected track position on the shower should ideally be zero. In practice, there is always some distribution to this difference, and a cut in placed at the level of a few sigma to eliminate particles with good tracks, but no certain shower hit.

χ^2 / ndof

The overall quality of the reconstructed track can be determined by calculating the

chi-squared divided by the number of degrees of freedom. In this case, χ^2 is given as

$$\chi^2 = \sum_i \frac{(x_{reconst} - x_{track})^2}{R_i^2} \tag{5.1}$$

where $x_{reconst}$ is the reconstructed hit position, x_{track} is the projected hit position of the track, and R is the resolution for each wire plane [11]. The number of degrees of freedom is the number of wire planes that are used in reconstructing the track. [11]. Particles which have a $\chi^2/N_{dof} > 2.4$ are removed from the analysis.

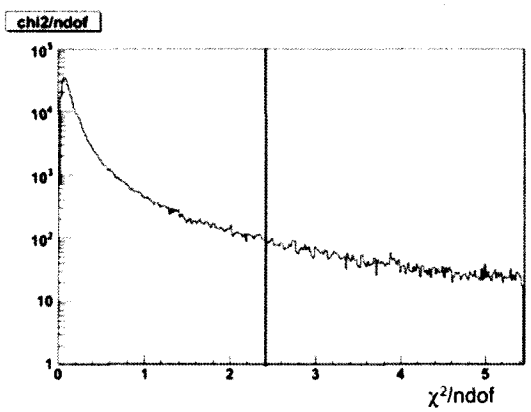

FIG. 5.4: Cut on χ^2/N_{dof} for track reconstruction (T6 events).

5.2.2 Particle Identification

Once the raw data has been pared down to 'quality data', one must turn to the task of separating good electrons from other contaminating particles, which can certainly pass all the quality checks. For E07-013, the main contamination comes from pions and pair-produced electrons. Each of these particles require their own set of PID cuts to properly study their contribution to the raw asymmetry. The PID cuts are described below.

Particle Charge

Because each particle that enters the BigBite detector package must first pass through the magnet, charged particles will have a track which distinctly bends left or right with respect to the direction of the magnetic field. Therefore, a cut on the bend direction of the particle is equivalent to a cut on its charge. Obviously, electrons and negative pions would have the same charge cut, while the positrons used to study pair-production would be opposite.

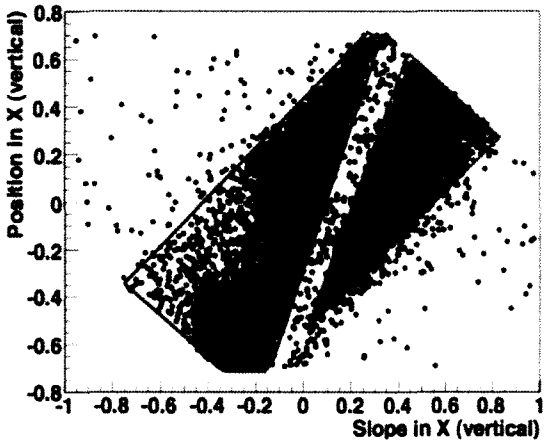

FIG. 5.5: Negative (blue triangle) and positive (red triangle) particles in the BigBite spectrometer

Particle Momentum

The momentum of a particle can be reconstructed using the bending angle of the track along with knowing the magnetic field of BigBite. Since the central value of the pion peak is at lower momentum than the electrons, a relatively high minimum momentum of 1.0 GeV/c was used in this analysis. Data binning was done using this momentum. Four bins of $1.0 < p_1 < 1.2 < p_2 < 1.5 < p_3 < 1.8 < p_4 < 2.5$ (GeV/c) were chosen so as to try to evenly distribute raw statistics amongst each bin.

Energy Deposited in Preshower

Energy deposited in the preshower calorimeter is the most important tool available to separate pions and electrons. Figure 5.6 shows the spectrum for particles which fired 'Trigger 6' - the main trigger for E07-013. Since pions are minimally ionizing, they will have a peak which is much lower in the preshower spectrum than that of electrons, which deposit significantly more energy. For the three highest momentum bins, an electron cut of PS $>$ 400 MeV was used. Since the lowest momentum bin had higher contamination, a higher cut of PS $>$ 600 MeV was used. Preshower cuts for a positron sample were identical. To select pions, a cut of PS $<$ 350 MeV was used.

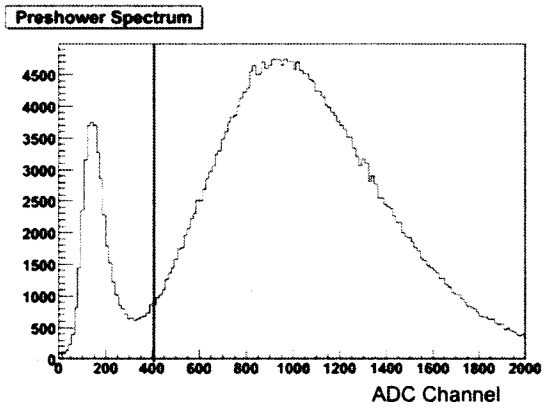

FIG. 5.6: Preshower spectrum for T6. Particles to the left of the red line are negative pions, while electrons are to the right. Leakage of the pion peak into the electron sample is addressed later.

E/p Cut

Because electrons have very little mass, the majority of their total energy is due to momentum. The ratio of their energy to momentum should then be very near one. For pions, one would expect this ratio to be less than one. A cut of $0.8 < E/p < 1.2$ is placed on the data to a exploit this. Figures 5.7 and 5.8 show a plot of energy deposited in the preshower versus this E/p ratio for T6 and T1, respectively.

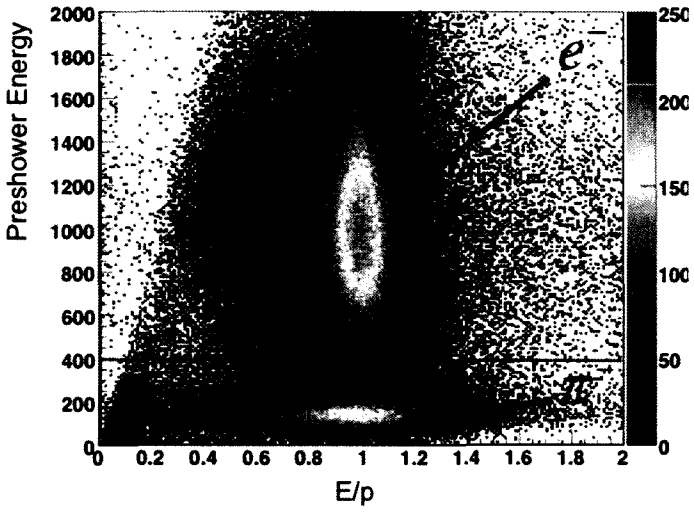

FIG. 5.7: Preshower energy versus E/p for T6 events. The pion peak position is shifted up in E/p compared to T1 due to the higher trigger threshold.

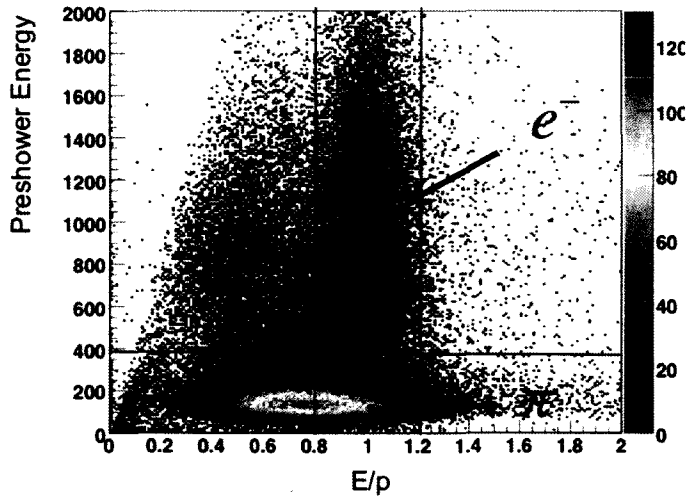

FIG. 5.8: Preshower energy versus E/p for T1 events. The fraction of electron events is drastically reduced due to the lower trigger threshold.

DIS Cut

Each event has several reconstructed kinematic variables associated with it. Because this is a deep inelastic measurement, a cut of $W > 2$ GeV was applied to all data.

5.3 Data Binning and Kinematics

Because the BigBite spectrometer package has large momentum acceptance, it is possible to group all of the collected data into several kinematic bins. For this analysis, four data bins were used. Binning was done using the reconstructed momentum of the particle. The size of the momentum bins were chosen such that the raw data would be evenly distributed amongst the four bins.

Within each momentum bin, each event has a set of reconstructed kinematic variables. The final central kinematic values for each bin (sans radiative corrections) were determined by averaging over all events in the bin. A summary of the kinematics are given in Table 5.1.

Momentum Range (GeV/c)	p (GeV/c)	W (GeV)	ν (GeV)	θ (degrees)	Q^2 (GeV/c)^2	x_b
1.00 - 1.22	1.12	2.86	4.67	29.6	1.71	0.191
1.22 - 1.50	1.36	2.71	4.53	29.6	2.08	0.244
1.50 - 1.80	1.64	2.52	4.25	29.5	2.50	0.314
1.80 - 2.50	2.05	2.26	3.84	28.8	3.00	0.414

TABLE 5.1: Kinematics for the four BigBite data points.

5.4 Contamination Studies

Despite application of all of the previously mentioned quality and PID cuts, the nature of BiteBite (being a detector with large momentum and spatial acceptance, as well as poor PID) allows for pions and 'bad' electrons to be recorded by the data acquisition system. Since all available PID cuts have been exhausted, one is left with the task of estimating the amount of contamination that remains in the data sample. Not only will this affect the numbers of 'good' electron events (and thus, statistical uncertainty) - these contaminating particles can also contribute their own asymmetry which in general differs from that of the good electrons of interest.

For E07-013, there are two types of contamination that must be addressed - negative pions (π^-) and pair-produced electrons (e^+ ; here, 'pair' refers to a photon-induced electron-positron pair, and so this contamination is usually referred to as 'positron contamination'). There are then four quantities which must be well-quantified in order to make the proper corrections to the asymmetry. First is the fraction of pion and positron contamination, denoted C_{π^-} and C_{e^+}, respectively. Further, one must know the corresponding asymmetries which these particles contributed, A_{π^-} and A_{e^+}. The correction has one further complication: the positron data sample which is used to study the pair-produced contamination has it's own contamination, the positive pion (π^+). Each of these contaminants are addressed below.

5.4.1 Negative Pion Contamination

Contamination due to π^- is the most straight-forward and benign to address. Figure 5.6 shows the spectrum of energy deposited in the preshower calorimeter. There is a clear separation of the π^- and electron peaks due to the fact that the π^- is a minimally ionizing

particle within the detector. Contamination is estimated directly by fitting each of the peaks to an appropriate function, setting a cut value, and comparing the integrated value of each function above the cut value. Figure 5.9 shows the results of this study.

The pion peak is fit using a Gaussian function that is convoluted with a Landau tail. The electron peak is fit to a gaussian shape. The contamination is then defined as:

$$C_{\pi^-} = \frac{\int_{ps_{min}}^{\infty} f(\pi^-)}{\int_{ps_{min}}^{\infty} f(e^-)} \tag{5.2}$$

where ps_{min} is the minimum preshower cut and $f(\pi^-)$ and $f(e^-)$ are the functional fits of the pion and electron peak, respectively.

Momentum Range (GeV/c)	$C_{\pi^-}^{T1}$ (%)	$C_{\pi^-}^{T6}$ (%)
1.00 - 1.22	8.0	0.5
1.22 - 1.50	7.0	1.2
1.50 - 1.80	2.8	1.0
1.80 - 2.50	0.5	0.4

TABLE 5.2: π^- contamination for each momentum bin and trigger in BigBite

5.4.2 Pair-Produced e^+e^- Contamination

A much more prominent form of contamination comes from the production of π^0. These particles have an extremely short lifetime - about 8.2×10^{-17} - before decaying primarily as:

$$\pi^0 \rightarrow \gamma + \gamma \tag{5.3}$$

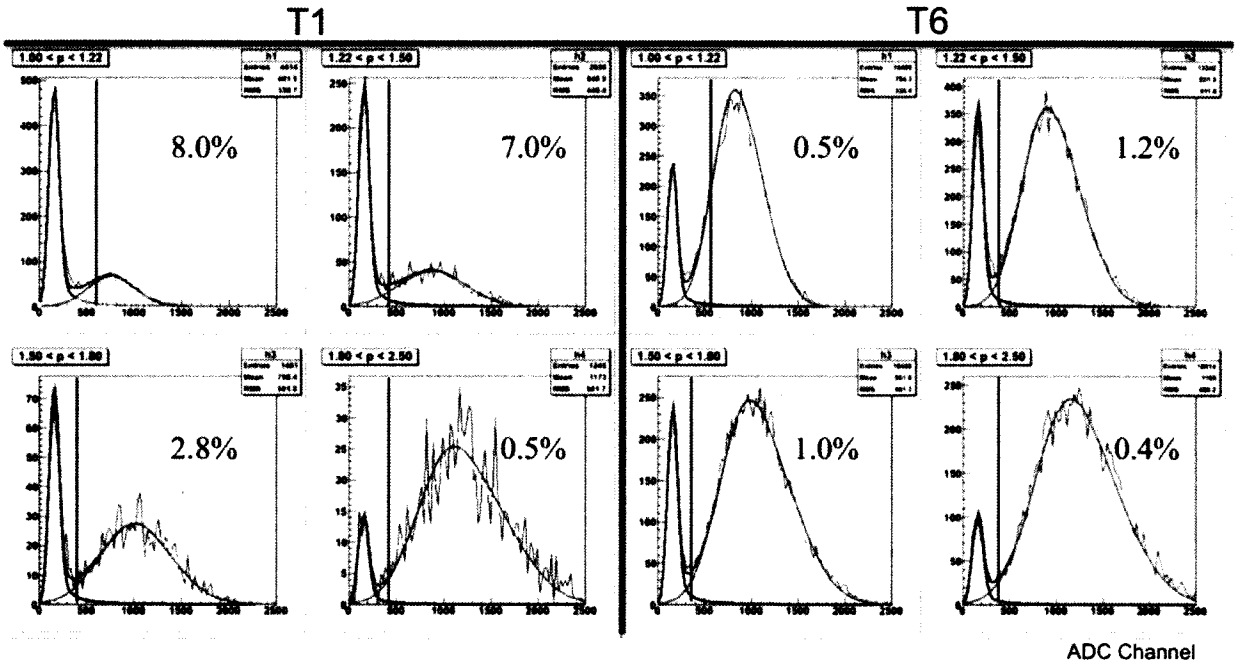

FIG. 5.9: Negative pion contamination estimates for each momentum bin. The vertical black line on each plot represents the preshower cut on that particular momentum bin. The blue fit is the pion peak and the red is the electron peak.

The short lifetime means that the decay occurs even before the π^0 has time to exit the target cell. As a consequence, it is very probable that the photons will then interact with the glass of the target cell, resulting in an e^-e^+ pair production. These pair-produced electrons cannot be distinguished from 'good' electrons in the BigBite detector, and thus, the level at which they contaminate the data must be calculated.

It is clear that for each contaminating pair-produced electron, there must also be a pair-produced positron. One can then estimate the number of pair-produced electrons simply by measuring the positron yield. For this reason, pair-production contamination is commonly referred to as positron contamination.

The positron yield is measured by reversing the polarity of the BigBite magnet and applying the same set of data cuts to the now positively charged data. Not surprisingly, these data will have it's own contamination - the π^+ particle - which must be accounted for. This is treated in the same manner as the π^- contamination in the previous section.

Figure 5.10 shows the positron yield (blue) compared to the electron yield (red), where the yield is given by:

$$Y_{e^{+(-)}} = \frac{N_{e^{+(-)}}}{Q_{e^{+(-)}} \cdot LT_{e^{+(-)}}} \tag{5.4}$$

with N being the number of positrons (electrons), Q being the charge on beam accumulated during the data run and LT is the livetime. Positron yield comes from positive polarity runs, while electron yield comes from the normal production data runs. The level of positron contamination is defined as

$$C_{e^+} = \frac{Y_{e^+}(1 - C_{\pi^+})}{Y_{e^-}(1 - C_{\pi^-})} \tag{5.5}$$

Here, $C_{\pi^{+(-)}}$ is the pion contamination in the respective data sample which must be subtracted out.

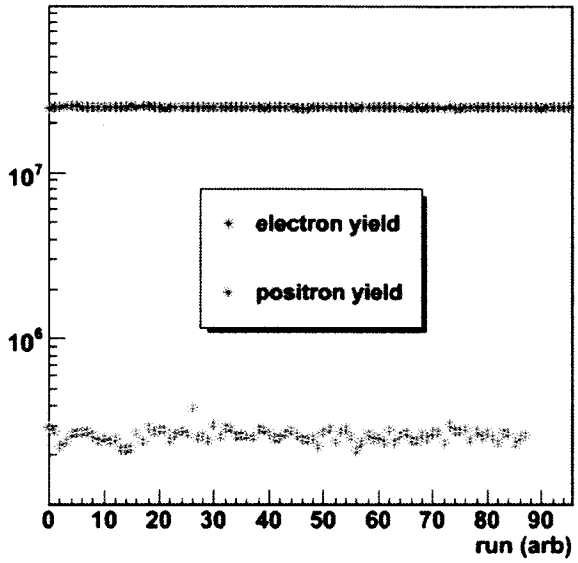

FIG. 5.10: Positron (blue) and electron (red) yield versus run number (arbitrary) for each of the momentum bins.

π^+ Contamination in the Positron Sample

The π^+ contamination in the positron data is calculated in the same way as for π^-, as in Equation 5.2. For the lowest momentum bins, the contamination in T6 is much smaller due to the higher trigger threshold. As momentum increases, the pair-production falls off such that the pions dominate. The final positron contamination is shown in Table 5.4.

5.4.3 Zero-Track Events

A possible third type of contamination could be 'no-track' (NT)events. If a particle such as a photon enters the detector, it will deposit energy in the calorimeters, but not have

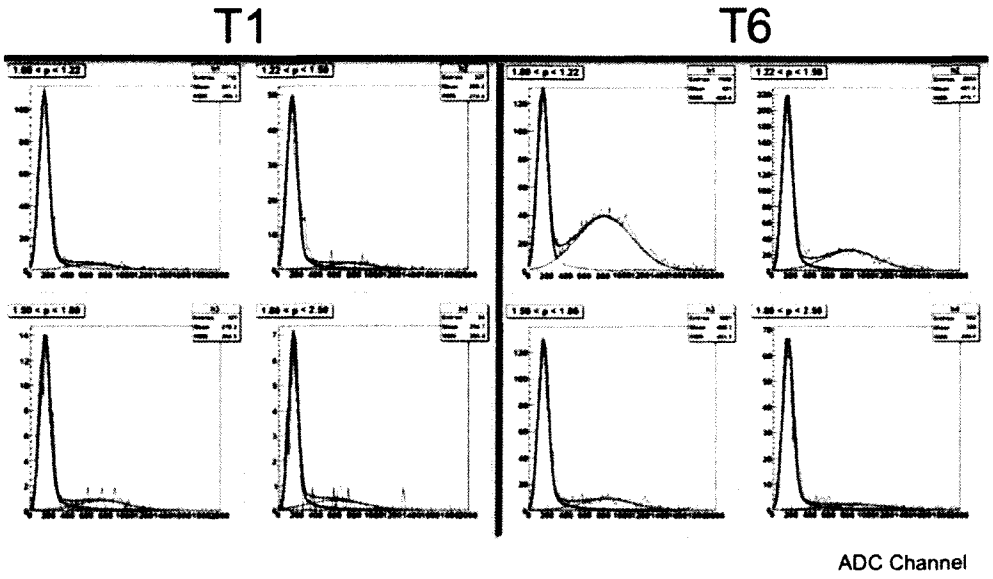

FIG. 5.11: Positive pion contamination estimates for each BigBite momentum bin.

p-bin	T1	T6
1	36%	3%
2	39%	11%
3	25%	19%
4	22%	38%

TABLE 5.3: π^+ contamination in the BigBite positron data sample

p-bin	T1	T6
1	39%	56%
2	32%	26%
3	27%	13%
4	19%	5%

TABLE 5.4: Positron contamination for each momentum bin and trigger in BigBite. These numbers are corrected for the presence of pions in the samples.

a track in the tracking chambers. If this NT-event energy deposition occurs in the same spacial region and at the same time as a good electron event, the total energy of the good electron will be incorrect. This event should not be recorded as a true 'good' event, and so represents a type of contamination. It is straightforward to measure the asymmetry of these particles, simply by requiring reasonable PID cuts and requiring that no track exist for the event. Unfortunately, there is no way to use the data to calculate the contamination level of NT-events. Further studies are needed to account for this contamination, however, the effect is believed to be small. Asymmetry results for NT-events are shown at the end of the thesis. The cuts used to identify these NT-events are:

Number of Tracks

The number of tracks must be zero.

Preshower Cut

The energy deposited in the preshower calorimeter must be greater than 200 MeV.

Shower Cluster Match

The preshower calorimeter energy deposition cluster must match the shower calorimeter energy deposition cluster.

Total Energy

The NT events are assumed to be mostly photons, which are massless. Thus, the total energy of the NT event should fall between $1.0 \text{ GeV} < E_{tot} < 2.5 \text{ GeV}$.

5.5 Asymmetry Formalism

A 'raw' asymmetry, along with several background asymmetries must be calculated, then combined appropriately in order to reach the end goal of the inclusive target single-

spin asymmetry of an electron scattering in the deep inelastic region from a neutron. In this thesis, the term 'raw' refers to an asymmetry which includes only PID cuts. It does NOT include corrections due to polarization, contamination, N_2 dilution, ^{3}He$\rightarrow$ n, or radiative corrections. Asymmetry terminology is summarized below.

A_{raw}: All good electron cuts are applied.

A_{π^-}: All good negative pion cuts are applied.

A_{e^+}: All good positron cuts are applied.

A_{π^+}: All good positive pion cuts are applied. This is needed to correct the positron asymmetry, A_{e^+}.

A_{e^-}: All good electron cuts are applied and contamination is removed.

The goal is to use A_{π^-}, A_{π^+} and A_{e^+} to correct A_{raw} in order to extract A_{e^-}. This is followed by corrections for target polarization, nitrogen dilution, neutron extraction and radiative corrections, which leads to the final result.

5.5.1 Defining The Single-Spin Asymmetries

The single-spin asymmetry for the i^{th} data run is defined as

$$A_X^i = \frac{Y_i^{\uparrow} - Y_i^{\downarrow}}{Y_i^{\uparrow} + Y_i^{\downarrow}} \tag{5.6}$$

where X can be any of the asymmetries listed above. $Y_i^{\uparrow(\downarrow)}$ is the yield with target spin up (down) for the run. The yield is given as

$$Y_X^{\uparrow(\downarrow)} = \frac{N_X^{\uparrow(\downarrow)}}{Q^{\uparrow(\downarrow)} \cdot LT^{\uparrow(\downarrow)}} \tag{5.7}$$

where N is the number of events in the respective target state, Q is the charge accumulated during the data run and LT the livetime of the detector. Contamination asymmetries are formed in the same fashion. Assuming LT and N are not statistically correlated, the uncertainty on the raw asymmetry is given by

$$\left(\delta A_X^i\right)^2 = \left(\frac{\partial A_X^i}{\partial Y_i^{\uparrow}}\right)^2 \left(\delta Y_i^{\uparrow}\right)^2 + \left(\frac{\partial A_X^i}{\partial Y_i^{\downarrow}}\right)^2 \left(\delta Y_i^{\downarrow}\right)^2 \tag{5.8}$$

which reduces to

$$\delta A_X^i = \frac{2Y_i^{\uparrow}Y_i^{\downarrow}}{\left(Y_i^{\uparrow} + Y_i^{\downarrow}\right)^2}\sqrt{\frac{1}{N_i^{\uparrow}} + \frac{1}{N_i^{\downarrow}}} \tag{5.9}$$

5.5.2 From Raw Asymmetry to Electron Asymmetry

Extraction of the electron asymmetry from the raw asymmetry requires proper subtraction of background contributions. For E07-013, this background is predominantly made up of negative pions and pair-produced electrons (a.k.a. positron contamination). Subtraction of the background is performed as follows: Begin by defining the raw yield in each target state as

$$Y_{raw}^{\uparrow(\downarrow)} = \frac{N_{raw}^{\uparrow(\downarrow)}}{Q^{\uparrow(\downarrow)} \cdot LT^{\uparrow(\downarrow)}} = \frac{N_{e^-}^{\uparrow(\downarrow)} + N_{\pi^-}^{\uparrow(\downarrow)} + N_{e^+}^{\uparrow(\downarrow)}}{Q^{\uparrow(\downarrow)} \cdot LT^{\uparrow(\downarrow)}} \tag{5.10}$$

where e^- are the good electrons, π^- the negative pions, and e^+ are the pair-produced positrons. The raw asymmetry is defined as

$$A_{raw} = \frac{Y_{raw}^{\uparrow} - Y_{raw}^{\downarrow}}{Y_{raw}^{\uparrow} + Y_{raw}^{\downarrow}} = \frac{\left(Y_{e^-}^{\uparrow} + Y_{\pi^-}^{\uparrow} + Y_{e^+}^{\uparrow}\right) - \left(Y_{e^-}^{\downarrow} + Y_{\pi^-}^{\downarrow} + Y_{e^+}^{\downarrow}\right)}{\left(Y_{e^-}^{\uparrow} + Y_{\pi^-}^{\uparrow} + Y_{e^+}^{\uparrow}\right) + \left(Y_{e^-}^{\downarrow} + Y_{\pi^-}^{\downarrow} + Y_{e^+}^{\downarrow}\right)} \tag{5.11}$$

Introduce the following short-hand notation for the difference or sum of terms:

$$\Delta_{e^-} = Y^{\uparrow}_{e^-} - Y^{\downarrow}_{e^-} \qquad \sum e^- = Y^{\uparrow}_{e^-} + Y^{\downarrow}_{e^-}$$
$$\Delta_{\pi^-} = Y^{\uparrow}_{\pi^-} - Y^{\downarrow}_{\pi^-} \qquad \sum \pi^- = Y^{\uparrow}_{\pi^-} + Y^{\downarrow}_{\pi^-}$$
$$\Delta_{e^+} = Y^{\uparrow}_{e^+} - Y^{\downarrow}_{e^+} \qquad \sum e^+ = Y^{\uparrow}_{e^+} + Y^{\downarrow}_{e^+}$$

$$\Delta_T = \Delta_{e^-} + \Delta_{\pi^-} + \Delta_{e^+} \qquad \sum T = \sum e^- + \sum \pi^- + \sum e^+$$

This allows the asymmetry to be written as

$$A_{raw} = \frac{\Delta e^- + \Delta \pi^- + \Delta e^+}{\sum e^- + \sum \pi^- + \sum e^+} = \frac{\Delta_T}{\sum_T}$$

$$= \frac{\Delta_{e^-}}{\sum_T} + \frac{\Delta_{\pi^-}}{\sum_T} + \frac{\Delta_{e^+}}{\sum_T}$$

Now multiply each term by a fraction that equals 1:

$$A_{raw} = \frac{\Delta_{e^-}}{\sum_T}\left(\frac{\sum e^-}{\sum e^-}\right) + \frac{\Delta_{\pi^-}}{\sum_T}\left(\frac{\sum \pi^-}{\sum \pi^-}\right) + \frac{\Delta_{e^+}}{\sum_T}\left(\frac{\sum e^+}{\sum e^+}\right)$$

$$= A_{e^-}\left(\frac{\sum e^-}{\sum_T}\right) + A_{\pi^-}\left(\frac{\sum \pi^-}{\sum_T}\right) + A_{e^+}\left(\frac{\sum e^+}{\sum_T}\right)$$

and solve for the electron asymmetry:

$$A_{e^-} = \left(\frac{\sum_T}{\sum e^-}\right)\left[A_{raw} - A_{\pi^-}\left(\frac{\sum \pi^-}{\sum_T}\right) - A_{e^+}\left(\frac{\sum e^+}{\sum_T}\right)\right]$$

The electron sum term can be re-written as

$$\sum e^- = \sum_T - \sum \pi^- - \sum e^+ = \sum_T \left(1 - \frac{\sum \pi^-}{\sum_T} - \frac{\sum e^+}{\sum_T}\right).$$

Define the contamination as the number of pions (positrons) divided by the total number of particles:

$$C_{\pi^-} = \frac{\sum \pi^-}{\sum_T} \qquad C_{e^+} = \frac{\sum e^+}{\sum_T} \tag{5.12}$$

Substitution of Equations 5.12 and 5.12 into Equation 5.12 gives the proper equation to extract the electron asymmetry from the contaminated raw event sample:

$$A_{e^-} = \frac{A_{raw} - C_{\pi^-} A_{\pi^-} - C_{e^+} A_{e^+}}{1 - C_{\pi^-} - C_{e^+}} \tag{5.13}$$

The statistical uncertainty is

$$\delta A_{e^-} = \frac{2Y^{\uparrow}Y^{\downarrow}}{(Y^{\uparrow} + Y^{\downarrow})^2} \sqrt{\frac{1}{N^{\uparrow}} + \frac{1}{N^{\downarrow}}} \left(\frac{1}{1 - C_{\pi^-} - C_{e^+}}\right) \tag{5.14}$$

A Note on Correcting the Positron Asymmetry

Just as the raw electron data is contaminated by π^-, the positron data sample will have π^+ contamination. A correction due to π^+ is made to A_{e^+} exactly as described above. The numerator in Equation 5.13 would become $A_{e^+} - C_{\pi^+} A_{\pi^+}$ and the $(1 - C_{\pi^-} - C_{e^+})$ term in both Equations 5.13 and 5.14 would become $(1 - C_{\pi^+})$.

5.5.3 Combining Data Runs

Each of A_{π^-}, A_{e^+} and A_{π^+} are combined run-by-run in the same manner. For each run, a statistical weighting factor is calculated as the ratio of the square of the reciprocal of the uncertainty for a given run to the sum over all runs of the squared reciprocal uncertainty:

$$w_X^i = \frac{\left(\frac{1}{\delta A_X^i}\right)^2}{\sum_i \left(\frac{1}{\delta A_X^i}\right)^2}. \tag{5.15}$$

The weighted asymmetry over all i runs is then

$$A_X = \sum_i w_X^i A_X^i. \tag{5.16}$$

The uncertainty on these asymmetries is

$$\delta A_X = \sqrt{\frac{1}{\sum_i \left(\frac{1}{\delta A_X^i}\right)^2}}. \tag{5.17}$$

This process gives final values for A_{π^-}, A_{e^+} and A_{π^+}, which will be treated as global numbers. While $A_{e^-}^i$ will be corrected on a run-by-run basis for target polarization, P_T^i, each run will use the same value of the contamination asymmetries. Thus, Equations 5.13 and 5.14 can be written with i indices on the appropriate variables:

$$A_{e^-}^i = \frac{A_{raw}^i - C_{\pi^-} A_{\pi^-} - C_{e^+} A_{e^+}}{1 - C_{\pi^-} - C_{e^+}} \tag{5.18}$$

$$\delta A^i_{e^-} = \frac{2Y_i^{\uparrow}Y_i^{\downarrow}}{\left(Y_i^{\uparrow}+Y_i^{\downarrow}\right)^2}\sqrt{\frac{1}{N_i^{\uparrow}}+\frac{1}{N_i^{\downarrow}}}\left(\frac{1}{1-C_{\pi^-}-C_{e^+}}\right)$$

Finally, corrections for target polarization and nitrogen dilution are applied:

$$A_{e^-} = \frac{1}{\eta_{N_2}}\sum_i \frac{w^i_{e^-}A^i_{e^-}}{P^i_T} \tag{5.19}$$

$$\delta A_{e^-} = \sqrt{\frac{1}{\sum_i\left(\frac{P^i_T\eta_{N_2}}{\delta A^i_X}\right)^2}}$$

A Note on Combining Triggers

It was mentioned earlier that there are two independent triggers, T1 and T6, which have useful data for this measurement (Each T6 is NOT counted as a T1). Each asymmetry mentioned to this point was calculated separately for T1 and T6. Final results were then combined via statistical weighting in the same manner as laid out above (essentially treating T1 and T6 results as two different data runs).

5.6 Extracting the Physics Asymmetry

5.6.1 Nitrogen Dilution

As mentioned in Chapter 3, a small amount of N_2 ($\sim$ 1% by density) is mixed with the ^{3}He in order to allow non-radiative decay instead of the emission of unpolarized photons during SEOP. This will cause the measured asymmetry to be diluted by electrons which scatter from unpolarized N_2, rather than polarized ^{3}He. The diluted asymmetry can

be written as

$$A_{meas}^{e^-} = \frac{Y_{^3He}^{\uparrow} - Y_{^3He}^{\downarrow}}{Y_{^3He}^{\uparrow} + Y_{^3He}^{\downarrow} + Y_{N_2}}. \tag{5.20}$$

One must multiply this measured asymmetry by a 'dilution factor' in order to properly remove the nitrogen term:

$$A_{meas}^{e^-} = \frac{Y_{^3He}^{\uparrow} - Y_{^3He}^{\downarrow}}{Y_{^3He}^{\uparrow} + Y_{^3He}^{\downarrow} + Y_{N_2}} f \tag{5.21}$$

where f is defined as

$$f = \frac{Y_{^3He}^{\uparrow} + Y_{^3He}^{\downarrow} + Y_{N_2}}{Y_{^3He}^{\uparrow} + Y_{^3He}^{\downarrow}}. \tag{5.22}$$

Using the fact that $Y_{N_2} \propto \rho_{N_2}\sigma_{N_2}$ and $Y_{^3He^{\uparrow}} + Y_{^3He^{\downarrow}} \propto \rho_{^3He}\sigma_{^3He}$, one can write

$$\eta_{N_2} \equiv \frac{1}{f} = \frac{\rho_{^3He}\sigma_{^3He}}{\rho_{^3He}\sigma_{^3He} + \rho_{N_2}\sigma_{N_2}}. \tag{5.23}$$

Dividing through by $\rho_{^3He}\sigma_{^3He}$, one has

$$\eta_{N_2} = \frac{1}{1 + \left(\frac{\rho_{N2}}{\rho_{^3He}}\right)\left(\frac{\sigma_{N2}}{\sigma_{^3He}}\right)} \tag{5.24}$$

which is the usual form for the nitrogen dilution factor. There are then two quantities needed to calculate the dilution. The first is the ratio of the two densities in the target cell. These are taken from the fill values of the cell, and are listed in Table 5.5. Uncertainties are taken as $\pm 2\%$ for $\rho_{^3He}$ and $\pm 5\%$ for ρ_{N_2}.

The cross-section ratio is determined experimentally by measuring scattering from

cell	$\rho_{^3He}$ (amg)	ρ_{N_2} (amg)
Astralweeks	8.08	0.11
Maureen	7.52	0.106
Brady	7.87	0.11

TABLE 5.5: The ^{3}He and N_2 densities for each target cell.

the reference cell, first with N_2, then with unpolarized ^{3}He. Each of the runs have the same reference cell geometry, beam energy, detector acceptance and particle ID, so one can simply compare the yields of each run, normalized to charge (Q), livetime (LT) and reference cell density (ρ_{gas}^{ref}):

$$\frac{\sigma_{N2}}{\sigma_{^3He}} \propto \frac{Y_{N2}}{Y_{^3He}} = \frac{N_{N2}}{N_{^3He}} \frac{Q_{^3He}}{Q_{N2}} \frac{LT_{^3He}}{LT_{N2}} \frac{\rho_{^3He}^{ref}}{\rho_{N2}^{ref}} \tag{5.25}$$

Uncertainties which must be accounted for include fill densities of the polarized target cells (listed above), and uncertainty on the cross-sections, which include both statistical uncertainty and uncertainty on reference cell pressure (± 1 psig). The total uncertainty on the cross section is given as

$$\delta\sigma_{gas} = \sqrt{\left(\frac{\delta N_{gas}}{Q \cdot LT \cdot \rho_{gas}}\right)^2 + (\sigma_{gas})^2 \left(\frac{\delta\rho_{gas}}{\rho_{gas}}\right)^2} \tag{5.26}$$

and the complete uncertainty on the nitrogen dilution factor is

$$\delta\eta_{N_2} = \eta^2 \frac{\rho_{N_2}}{\rho_{^3He}} \frac{\sigma_{N_2}}{\sigma_{^3He}} \sqrt{\left(\frac{\delta\rho_{N_2}}{\rho_{N_2}}\right)^2 + \left(\frac{\delta\rho_{^3He}}{\rho_{^3He}}\right)^2 + \left(\frac{\delta\sigma_{N_2}}{\sigma_{N_2}}\right)^2 + \left(\frac{\delta\sigma_{^3He}}{\sigma_{^3He}}\right)^2}. \tag{5.27}$$

The nitrogen dilution factors averaged over all 3 target cells are given in Table 5.6. Figure 5.12 shows the dilution factor for each cell and each kinematic point.

x_B	η_{N_2}	$\pm\ \delta\eta_{N_2}$
0.190	0.908	0.010
0.243	0.897	0.011
0.243	0.900	0.011
0.414	0.903	0.011

TABLE 5.6: Nitrogen Dilution for 4 x-bins.

As a cross-check, one can estimate nitrogen dilution factors directly from the structure function, F_2 for protons and deuterium. Recall Equation 5.28:

$$\eta_{N_2} = \frac{1}{1 + \left(\frac{\rho_{N2}}{\rho_{^3He}}\right)\left(\frac{\sigma_{N2}}{\sigma_{^3He}}\right)} \tag{5.28}$$

In the deep-inelastic region, the ratio of cross-sections can be estimated simply by counting the respective number of protons and neutrons in nitrogen and ^{3}He:

$$\begin{aligned} \sigma_{^3He}^{DIS} &\approx 2\sigma_p^{DIS} + \sigma_n^{DIS} \propto 2F_2^p + F_2^n \\ \sigma_{N_2}^{DIS} &\approx 7\sigma_p^{DIS} + 7\sigma_n^{DIS} \propto 7F_2^p + 7F_2^n \end{aligned} \tag{5.29}$$

which then gives the ratio

$$\frac{\sigma_{N2}}{\sigma_{^3He}} \approx \frac{7\sigma_p + 7\sigma_n}{2\sigma_p + \sigma_n}. \tag{5.30}$$

The nitrogen dilution can then be written as

$$\eta_{N_2} = \frac{1}{1 + \left(\frac{\rho_{N2}}{\rho_{^3He}}\right)\left(\frac{7\sigma_2^p + 7\sigma_2^n}{2\sigma_2^p + \sigma_2^n}\right)}. \tag{5.31}$$

In DIS, the cross-sections can be well approximated using the structure functions, $\sigma_x \propto$

F_2^x. One can then write things in terms of the proton and deuterium structure functions $F_2^d = (F_2^p + F_2^n)/2$:

$$\eta_{N_2} = \frac{1}{1 + \left(\frac{\rho_{N2}}{\rho_{^3He}}\right)\left(\frac{5F_p+14F_d}{F_p+2F_d}\right)}. \tag{5.32}$$

Structure functions were calculated using

$$F_2^{p(n)} = \sum_q e_q^2 \cdot x \cdot q(x) \tag{5.33}$$

where $q(x)$ are quark distribution functions. Results from calculations for η_{N_2} as well as the ratio of $\eta_{N_2}^{data}$ to $\eta_{N_2}^{calc}$ are shown in Table 5.7. The model used for calculations does not include the EMC effect or radiative corrections. However, it agrees with the data to within 3%. This thesis uses results from the data method for corrections to the asymmetry and useds the statistical error on the data method as the systematic error on η_{N_2}.

x_B	$\eta_{N_2}^{calc}$	$\frac{\eta_{N_2}^{data}}{\eta_{N_2}^{calc}}$
0.190	0.9198	0.986
0.243	0.9200	0.974
0.243	0.9203	0.980
0.414	0.9206	0.981

TABLE 5.7: Nitrogen Dilution for 4 x-bins calculated using structure functions. The right-most column is the ratio of direct measurement of nitrogen dilution to the calculated values.

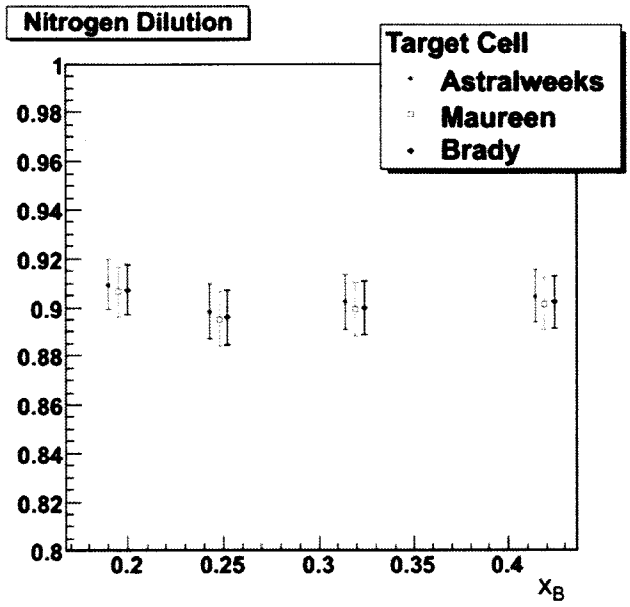

FIG. 5.12: Nitrogen dilution calculated from reference cell data runs.

5.6.2 Neutron Extraction from ^{3}He

To this point, all asymmetries are from a ^{3}He target. In order to extract the neutron asymmetry from the ^{3}He asymmetry, an effective polarization approach is used:

$$A_y^{^3He} = f_n p_n A_y^n + 2 f_p p_p A_y^p \tag{5.34}$$

where A_y^n and A_y^p are the physics asymmetries which correspond to the neutron and proton. Solving for A_y^n gives:

$$A_y^n = \frac{A^{^3He} - 2 p_p f_p A_y^p}{p_n f_n}$$

The terms p_n and p_p are the effective polarization of the neutron and proton, and were discussed in Chapter 4. They are taken to be:

$$p_n = 0.86 \pm 0.02, \qquad p_p = -0.028 \pm 0.004$$

The terms f_n and f_p are the neutron and proton dilution factors to be determined. This can be accomplished either with reference cell data ('data method') or by using a simple model of the unpolarized (U) ^{3}He cross-section ('theory method'):

$$\sigma_U^{^3He} = 2\sigma_U^p + \sigma_U^n$$

such that the neutron and proton dilution factors are simply:

$$f_n = \frac{\sigma_U^n}{2\sigma_U^p + \sigma_U^n} \qquad f_p = \frac{\sigma_U^p}{2\sigma_U^p + \sigma_U^n} \tag{5.35}$$

The cross-sections can be re-written in terms of structure functions, as in Equation 5.32:

$$f_n = \frac{F_2^n}{2F_2^p + F_2^n} \qquad f_p = \frac{F_2^p}{2F_2^p + F_2^n} \tag{5.36}$$

The neutron dilution factor can be simply expressed as $f_n = 1 - f_p$. Thus, if one can experimentally determine f_p, f_n follows. The data method of obtaining the dilution factors relies on this idea. The yield from the reference cell filled with a source of protons (H_2) can be directly compared to the yield from the reference cell filled with ^{3}He:

$$f_n = 1 - f_p = 1 - \frac{\sigma_p}{2\sigma_p + \sigma_n} = 1 - \frac{\sigma_{H_2}}{\sigma_{^3He}} \tag{5.37}$$

Results for f_n for each method is shown in Figure 5.13 and listed in Table 5.8. The theory method is done solely as a cross-check for the data method, which is used for the final neutron extraction. Data method uncertainty comes from the uncertainty on the yields.

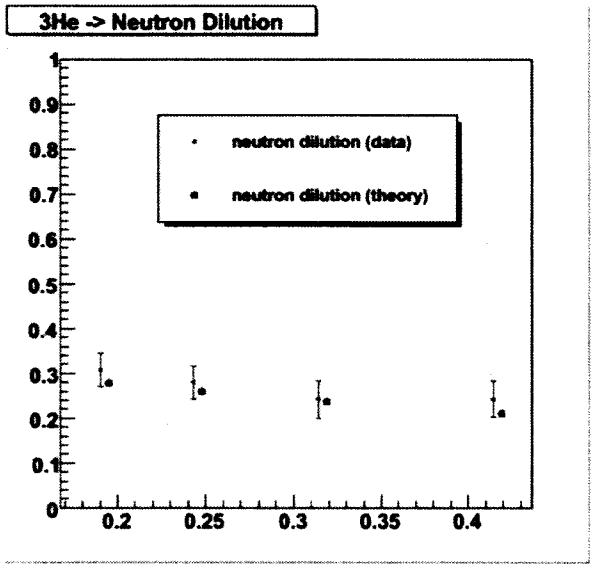

FIG. 5.13: Neutron dilution factors. Red data points are f_n^{data}. Blue points are $f_n^{F_2}$

x_B	f_n^{data}	δf_n^{data}	$f_n^{F_2}$	$\frac{F_2}{data}$
0.190	0.307	$\pm$ 0.038	0.279	0.91
0.243	0.279	$\pm$ 0.037	0.260	0.93
0.243	0.242	$\pm$ 0.040	0.237	0.98
0.414	0.242	$\pm$ 0.041	0.210	0.88

TABLE 5.8: Neutron dilution factor determined both experimentally (data) and by calculation (F_2).

5.7 High Resolution Spectrometer Data

As mentioned previously, E07-013 was parasitic to the Transversity experiment, E06-010. As a consequence, the Left Arm High Resolution Spectrometer (LHRS) in Hall A was accepting electron data throughout the duration of E07-013. Analysis of this data gives yet another kinematic point for the DIS SSA. Further, the LHRS data provides a systematic cross-check for the BigBite data. Because the LHRS and BigBite are on opposite sides of the beamline, the measured asymmetries should have opposite signs.

This section gives an overview of the LHRS SSA analysis. The formalism and procedure are exactly the same as for BigBite. The differences are the PID cuts and levels of π^- and e^+ contamination. Since this is a HRS with smaller acceptance, there is no momentum binning and thus only one data point. A summary of the LHRS kinematics is shown in Table 5.9.

p (GeV/c)	W (GeV)	ν (GeV)	θ	Q^2 (GeV/c)^2	x_b
2.35	2.55	3.54	15.9	1.04	0.157

TABLE 5.9: Kinematics for the LHRS data point

5.7.1 The Left HRS Layout

The LHRS contains three quadrupole magnets and one dipole magnet in a QQDQ configuration. These are followed by a layer of VDCs, a scintillator (S1), aerogel detector (A1), gas cherenkov detector, RICH detector, second scintillator (S2m) and finally, two pion rejectors. The singles trigger for the LHRS ('T3') required a hit in both of the S1 and S2m scintillator paddles, along with appropriate timing. An in-depth discussion on

trigger logic can be found in [11]. Figure 5.14 shows a schematic of the LHRS.

5.7.2 LHRS PID Cuts

Below is a summary of data cuts used to identify electrons in the LHRS. These cuts are much simpler and less numerous than those for BigBite - a consequence of the high-resolution design.

Cherenkov Energy Deposition

Electrons fire the detector, whereas hadrons will not, thus Cherenkov ADC > 300.

Aerogel Energy Deposition

Electrons will fire the aerogel detector, thus a cut of $A1 > 150$ was used.

E/p

Same as BigBite E/p, but with different electron/pion peak locations. $E/p > 0.65$.

Number of Tracks

One and only one track should exist for the LHRS spectrometer, thus $N_{track} = 1$.

Beam Trip Cut

Same cut as is used for BigBite data to remove beam trips.

DIS Cut

Same cut as is used with BigBite data to ensure deep inelastic scattering, $W > 2$ GeV.

Acceptance Cuts

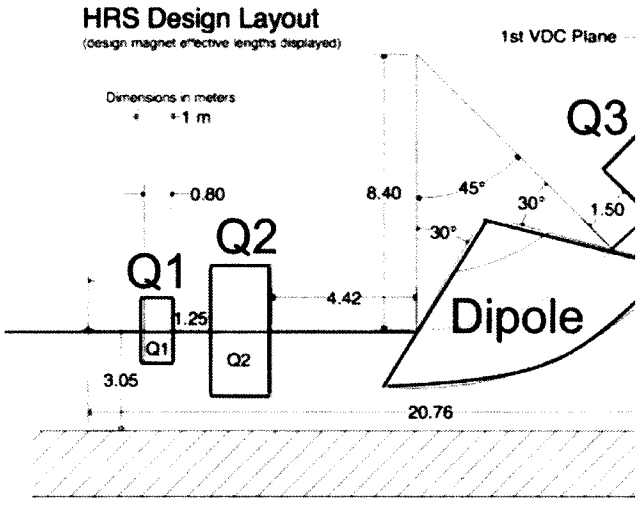
HRS Design Layout
(design magnet effective lengths displayed)
1st VDC Plane
Dimensions in meters
1 m
Q3
0.80
8.40
45°
30°
1.50
30°
Q2
Q1
4.42
Dipole
1.25
Q1
Q2
3.05
20.76

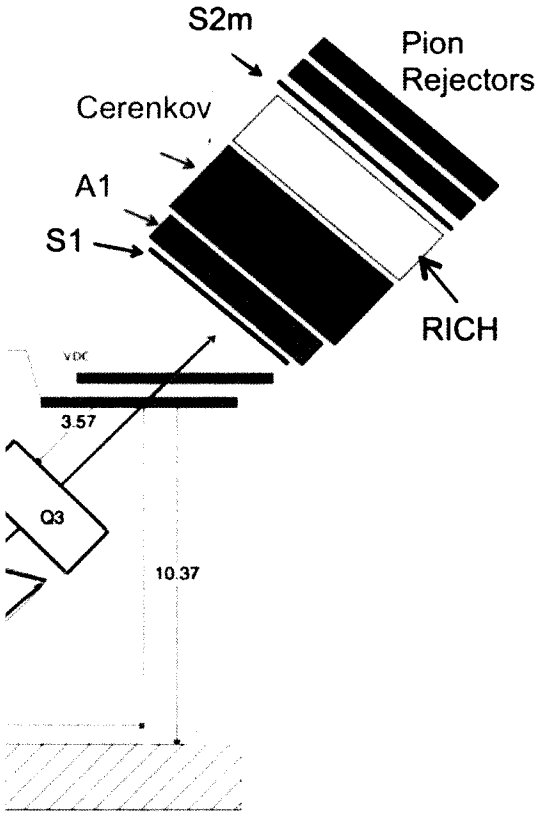

FIG. 5.14: The Left High Resolution Spectrometer in Hall A.

Cuts were applied to the track projections on the pion rejector:

$$-1.5 < L.prl1.trx < 1.0,$$

$$-0.2 < L.prl1.try < 0.2$$

5.7.3 LHRS Contamination

As with the BigBite singles data, the two concerning forms of contamination in the LHRS (T3) trigger will be pions and positrons. Reference [34] takes an in-depth look at negative pion contamination in the LHRS and finds it to be negligible, thus it is ignored here. The positron contamination is studied in the same manner as the BigBite data. The yields of both positrons and electrons are shown in Figure 5.15. In the absence of pion contamination, the expression for positron contamination is simply given as:

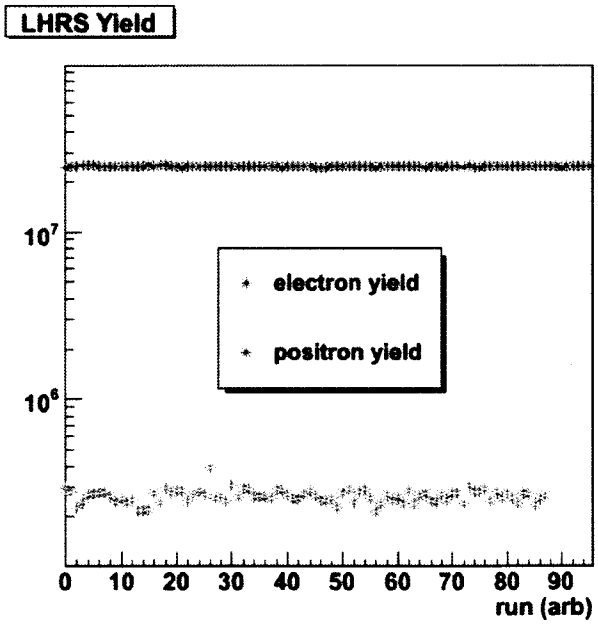

FIG. 5.15: Positron (green) and electron(red) yields in the LHRS.

$$\%C_{e^+}^{LHRS} = \frac{Y^{e^+}}{Y^{e^-}} = 1.1\%$$

where $Y^{e^{+(-)}}$ is the usual definition of particle yield.

5.7.4 LHRS Dilution

Nitrogen dilution as well as ^{3}He$\longrightarrow n$ factors were calculated for the LHRS in exactly the same manner as for BigBite. The values are $\eta_{N_2} = 0.88 \pm 0.03$ and $f_n = 0.21 \pm 0.037$.

5.8 Radiative Corrections

The scattering theory which was laid forth in Chapters 1 and 2 assume that the cross-section is made up of the Born term plus the next-to-leading order 2γ term. This is an incomplete picture, as in reality there are an infinite number of higher order terms, such as loop diagrams, bremsstrahlung and ionization effects. This 'radiated' cross-section is what is measured in the lab. Radiative corrections are performed in order to address these processes. For a target single-spin asymmetry, diagrams which do not have two photons coupling to the target do not have an asymmetry, thus, these 'internal' corrections can be ignored. It is the 'external' ionization and bremsstrahlung that are the most significant for this experiment.

Despite the fact that a deep-inelastic cut on the invariant mass of $W > 2$ GeV is applied to the data, this does not guarantee that all data which passes the cut are truly from the DIS process. It is certain that some electrons will experience an interaction in another of the scattering regions, then radiate energy away (via interaction with materials)

such that it *appears* to have the correct final energy to satisfy the DIS cut. For this reason, one must estimate the non-DIS contributions to the total radiated cross-section at the kinematics of the experiment. This requires strict accounting of the amount and type of material surrounding the target.

Energy loss due to ionization is dependent on both the type and thickness of material passed through (in radiation lengths). Figure 5.16 shows a summary of the materials which can affect the energy of the electron. The materials before scattering include the beryllium exit window of the beam pipe, ^{4}He inside the target enclosure, ^{3}He cell window and ^{3}He gas (assuming that *before* the interaction, the electron traversed half of the target cell). After scattering, the electron passes through the remainder of the ^{3}He gas, the glass cell wall, ^{4}He inside the target enclosure, the target enclosure itself (G10 glass reinforced epoxy), and an air gap between the target enclosure and BigBite detector. For the LHRS data, the Kapton entrance window must also be considered. The material of the target enclosure was found to contribute an insignificant amount. Since the LHRS and BigBite are at significantly different scattering angles, the amount of glass target cell passed through will be different for the two spectrometers.

The radiation lengths of the different materials are summarized in Table 5.10. Variables are defined as follows: The radiation length of the material is X_0. The density of the material is ρ, and given in gm/cm^3. The thickness of the material is simply the path-length that the electron has through the material, in cm. '# of X_0' is a unitless number, defined as the ratio of thickness to radiation length.

Using this information, the unpolarized radiated cross-section is calculated using the Mo and Tsai formalism [57] for external radiative corrections. The total cross-section is the sum of the elastic cross-section, quasi-elastic cross-section, resonances, and deep inelastic cross-sections. Each of these were calculated by fitting existing world data. An

extensive discussion of this code can be found in [8]. Figure 5.17 shows the radiative contributions to the total cross-section with an incident electron energy of $E_0 = 5.89$ GeV and a scattering angle of $30°$. It is clear that the quasi-elastic tail is by far the most significant at these kinematics, with the remaining resonances contributing well under 1%. Table 5.11 summarizes the quasi-elastic contribution to E07-013 data. For BigBite data, the lowest momentum bin, the quasi-elastic background is $\sim 10\%$. The second bin sees a background of less than 5%, the third is just over 2% and the highest momentum bin is less than 1%. For the LHRS data, the quasi-elastic contribution is about 4%. Regardless of data point, this results in a shift in the asymmetry central value of less than 1% (estimated using preliminary A_y^{QE} results from JLab). Thus, these radiative corrections are simply included in the systematic uncertainty budget.

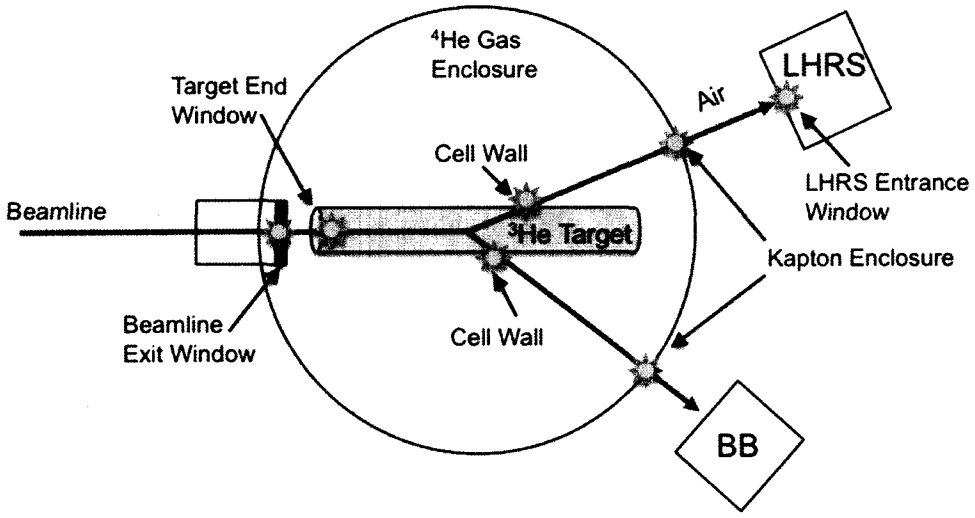

FIG. 5.16: Sources of electron energy loss surrounding the point of interaction.

Material *before*	X_0 (cm)	$\rho\left(\frac{\text{gm}}{\text{cm}^3}\right)$	Thickness (cm)	# of X_0
Be	35.28	1.848	0.0254	0.000719
^{4}He	528107.5	0.00166	22.86	0.0000433
Glass	7.038	2.76	0.01	0.00142
^{3}He	43423	0.00125	19.9	0.000456
				$\sum^{before} = 0.00263$
Material *after* (BigBite)	X_0 (cm)	$\rho\left(\frac{\text{gm}}{\text{cm}^3}\right)$	Thickness (cm)	# of X_0
^{3}He	43423	0.00125	1.9	0.0000438
Glass	7.038	2.76	0.22	0.03125
^{4}He	528107.5	0.00166	80.77	0.0001529
Air	30423	0.00121	67.11	0.002206
				$\sum^{after}_{BigBite} = 0.03365$
Material *after* (LHRS)	X_0 (cm)	$\rho\left(\frac{\text{gm}}{\text{cm}^3}\right)$	Thickness (cm)	# of X_0
^{3}He	43423	0.00125	3.44	0.0000792
Glass	7.038	2.76	0.399	0.0566922
^{4}He	528107.5	0.00166	79.05	0.0001496
Air	30423	0.00121	51.23	0.0016839
Kapton	28.6	1.42	0.0254	0.0008881
				$\sum^{after}_{LHRS} = 0.05949$

TABLE 5.10: Radiation lengths of material surrounding the target

$< p >$ (GeV/c)	σ_{total} (μb)	σ_{QE} (μb)	$C_{QE} \equiv \frac{\sigma_{QE}}{\sigma_{total}}$	$C_{QE} * A_y^{QE}$	$\frac{C_{QE} * A_y^{QE}}{\delta A_y^{DIS}}$
1.11	2.40×10^{-5}	2.02×10^{-6}	0.084	1.68×10^{-4}	9.3×10^{-3}
1.36	1.85×10^{-5}	9.01×10^{-7}	0.049	9.80×10^{-5}	9.5×10^{-3}
1.64	1.46×10^{-5}	3.19×10^{-7}	0.022	4.40×10^{-5}	4.2×10^{-3}
2.05	9.8×10^{-6}	8.40×10^{-8}	0.009	1.80×10^{-5}	1.7×10^{-3}

TABLE 5.11: Quasi-elastic contribution due to radiation effect at $E_0 = 5.89$ GeV and $\theta = 30°$.

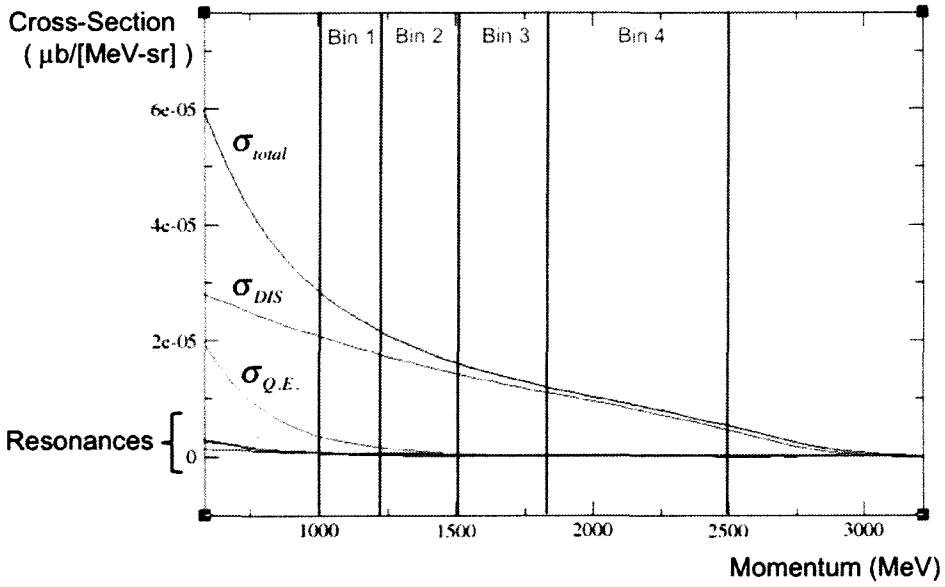

FIG. 5.17: Radiative contributions to the total unpolarized cross-section versus momentum at $E_0 = 5.89$ GeV and $\theta = 30°$. Shown is the total (black), DIS (purple), quasi-elastic (green) and the Delta (yellow), R1(brown), R2 (blue) and 2N (red) resonances.

5.9 Systematic Uncertainty

This section summarizes the systematic uncertainties that are associated with the target single-spin asymmetry measurement. Table 5.12 summarizes all the systematic uncertainties and their contribution to the overall uncertainty. They are first separated as correlated (corr) and uncorrelated (uncorr) effects, then combined for a total systematic error. The main systematic uncertainties are:

Negative Pion Asymmetry: is the statistical uncertainty on the negative pion asymmetry that was measured during E07-013, for each bin.

Positron Asymmetry : is the statistical uncertainty associated with the pair-produced electron asymmetry that was measured during E07-013, for each bin.

Negative Pion Contamination: is the uncertainty on the level of negative pion contamination that remains in the final data sample. Each bin was assigned a relative uncertainty of 100%.

Pair-Produced Electron Contamination: is uncertainty on the level of pair-produced electron contamination that remains in the final data sample. This is easily the largest systematic uncertainty in the entire experiment. Presently, there are two independent methods used to calculate these numbers: the method laid out in Section 5.4.2, and a calculation performed by Xin Qian in his thesis [34]. The uncertainty applied to the contamination numbers is the difference between the two methods.

Target Polarization: Error on the target polarization is taken to be 5% relative to the measured polarization value. This includes error on the target density.

Target Misalignment: The target polarization direction ($\theta_{^3He}$) is known to $\pm 0.5°$. Misalignment could dilute the vertical data asymmetry and enhance the transverse data asymmetry. Further, although it was ignored for this measurement, the beam was polarized throughout the experiment. The helicity sequence had quartet structures of either $+--+$ or $-++-$. Should a double-spin asymmetry (DSA) exist for this experiment's target and beam configuration, this could also enter as a systematic effect. However, these effects are proportional to the sine of the misalignment, i.e. $\sin(0.5°)$. This means the DSA must be at least 10% to contribute to these results at the 10^{-3} level. To contribute at the 10^{-2} level, the DSA would have to be greater than 100%. This effect is considered small, and not included in the error budget.

Nitrogen Dilution: Error on the nitrogen dilution numbers is due to both uncertainty in the fill density of ^{3}He ($\sim 2\%$) as well as N_2 ($\sim 5\%$). It also includes uncertainty on the reference cell pressure (~ 1 psig). The uncertainty is between $3-4\%$ relative to the value of η_{N_2}.

^{3}He $\rightarrow$ n, f_n: is the uncertainty introduced due to extraction of the neutron from the ^{3}He nucleus.

Luminosity Asymmetry: is taken to be the FWHM value of the luminosity asymmetry distribution in Figure 3.14, which has a value of 1×10^{-4}.

Livetime Asymmetry: is taken as the value of the livetime asymmetry, shown in Figure 5.18. It's value is 1.5×10^{-4}.

Radiative Corrections: is taken as $X\%$ of the statistical uncertainty, when X is 100 times the ratio in the final column of Table 5.11.

Each of these uncertainties contribute to the overall asymmetry as:

$$(\delta A_y^{sys})^2 = \left(\frac{\partial A_y^n}{\partial A_{\pi^-}}\right)^2 (\delta A_{\pi^-})^2 + \left(\frac{\partial A_y^n}{\partial A_{e^+}}\right)^2 (\delta A_{e^+})^2 + \left(\frac{\partial A_y^n}{\partial C_{\pi^-}}\right)^2 (\delta C_{\pi^-})^2 + \left(\frac{\partial A_y^n}{\partial C_{e^+}}\right)^2 (\delta C_{e^+})^2 + \left(\frac{\partial A_y^n}{\partial P_T}\right)^2 (\delta P_T)^2 + \left(\frac{\partial A_y^n}{\partial \eta_{N_2}}\right)^2 (\delta \eta_{N_2})^2 + \left(\frac{\partial A_y^n}{\partial f_n}\right)^2 (\delta f_n)^2 + (A_{lumi})^2 + (A_{LT})^2 + (\delta R.C.)^2 \left(\delta A_y^{stat}\right)^2$$

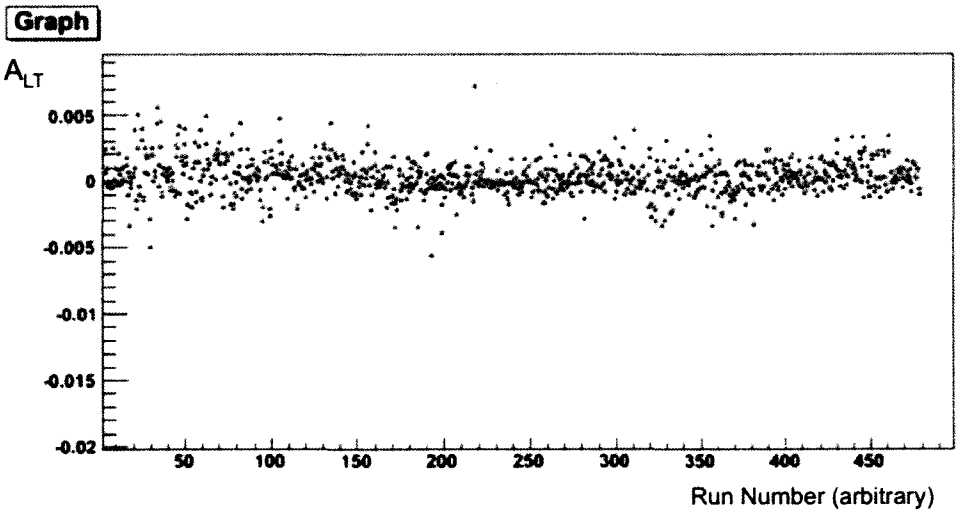

FIG. 5.18: The livetime asymmetry for E07-013. The red points are for T1 and the green are T6, which makes up over 90% of all data. The average value is 1.5×10^{-4}.

BigBite Momentum Bin 1				
Source	Corr / Uncorr	Uncertainty	Relative / Absolute	δA_{sys}^{source}
A_{π^-}	uncorr	0.0015	absolute	5.85×10^{-5}
A_{e^+}	uncorr	0.0019	absolute	3.9×10^{-3}
C_{π^-}	uncorr	100%	relative to C_{π^-}	1.97×10^{-3}
C_{e^+}	uncorr	20%	relative to C_{e^+}	2.08×10^{-2}
P_T	corr	5%	relative to P_T	3.56×10^{-3}
η_{N_2}	corr	0.010	absolute	7.9×10^{-4}
^{3}He$\rightarrow n$	corr	0.03	absolute	7.6×10^{-3}
A_{lumi}	uncorr	1.0×10^{-4}	absolute	1.0×10^{-4}
A_{LT}	uncorr	1.5×10^{-4}	absolute	1.5×10^{-4}
Rad. Corr.	corr	0.93%	relative to δA_y^{stat}	1.67×10^{-4}
			Correlated:	$\delta A_{sys}^{\text{corr}} = 8.4 \times 10^{-3}$
			Uncorrelated:	$\delta A_{sys}^{\text{uncorr}} = 2.1 \times 10^{-2}$
			Total:	$\delta A_{sys} = 2.3 \times 10^{-2}$

TABLE 5.12: Systematic Uncertainty in the lowest BigBite momentum bin.

BigBite Momentum Bin 2				
Source	Corr / Uncorr	Uncertainty	Relative / Absolute	δA_{sys}^{source}
A_{π^-}	uncorr	0.0018	absolute	6.30×10^{-5}
A_{e^+}	uncorr	0.0021	absolute	1.37×10^{-3}
C_{π^-}	uncorr	100%	relative to C_{π^-}	4.10×10^{-4}
C_{e^+}	uncorr	58%	relative to C_{e^+}	5.0×10^{-3}
P_T	corr	5%	relative to P_T	3.03×10^{-4}
η_{N_2}	corr	0.011	absolute	8.0×10^{-5}
^{3}He$\rightarrow n$	corr	0.03	absolute	7.0×10^{-4}
A_{lumi}	uncorr	1.0×10^{-4}	absolute	1.0×10^{-4}
A_{LT}	uncorr	1.5×10^{-4}	absolute	1.5×10^{-4}
Rad. Corr.	corr	0.95%	relative to δA_y^{stat}	9.8×10^{-5}
			Correlated:	$\delta A_{sys}^{\text{corr}} = 8.0 \times 10^{-4}$
			Uncorrelated:	$\delta A_{sys}^{\text{uncorr}} = 5.2 \times 10^{-3}$
			Total:	$\delta A_{sys} = 5.3 \times 10^{-3}$

TABLE 5.13: Systematic Uncertainty in the 2nd BigBite momentum bin.

BigBite Momentum Bin 3				
Source	Corr / Uncorr	Uncertainty	Relative / Absolute	δA_{sys}^{source}
A_{π^-}	uncorr	0.0027	absolute	6.30×10^{-5}
A_{e^+}	uncorr	0.0032	absolute	6.1×10^{-4}
C_{π^-}	uncorr	100%	relative to C_{π^-}	4.13×10^{-4}
C_{e^+}	uncorr	110%	relative to C_{e^+}	9.0×10^{-3}
P_T	corr	5%	relative to P_T	1.4×10^{-3}
η_{N_2}	corr	0.011	absolute	3.46×10^{-4}
$^3\text{He} \rightarrow n$	corr	0.03	absolute	3.69×10^{-3}
A_{lumi}	uncorr	1.0×10^{-4}	absolute	1.0×10^{-4}
A_{LT}	uncorr	1.5×10^{-4}	absolute	1.5×10^{-4}
Rad. Corr.	corr	0.42%	relative to δA_y^{stat}	4.4×10^{-5}
			Correlated:	$\delta A_{sys}^{\text{corr}} = 8.0 \times 10^{-4}$
			Uncorrelated:	$\delta A_{sys}^{\text{uncorr}} = 9.1 \times 10^{-3}$
			Total:	$\delta A_{sys} = 9.2 \times 10^{-3}$

TABLE 5.14: Systematic Uncertainty in the 3rd BigBite momentum bin.

BigBite Momentum Bin 4				
Source	Corr / Uncorr	Uncertainty	Relative / Absolute	δA_{sys}^{source}
A_{π^-}	uncorr	0.0038	absolute	4.4×10^{-5}
A_{e^+}	uncorr	0.0047	absolute	5.2×10^{-5}
C_{π^-}	uncorr	100%	relative to C_{π^-}	5.4×10^{-4}
C_{e^+}	uncorr	350%	relative to C_{e^+}	9.36×10^{-3}
P_T	5%	corr	relative to P_T	1.46×10^{-3}
η_{N_2}	corr	0.011	absolute	3.56×10^{-4}
^{3}He$\rightarrow n$	corr	0.03	absolute	4.18×10^{-3}
A_{lumi}	uncorr	1.0×10^{-4}	absolute	1.0×10^{-4}
A_{LT}	uncorr	1.5×10^{-4}	absolute	1.5×10^{-4}
Rad. Corr.	corr	0.17%	relative to δA_y^{stat}	1.78×10^{-5}
			Correlated:	$\delta A_{sys}^{\text{corr}} = 8.0 \times 10^{-4}$
			Uncorrelated:	$\delta A_{sys}^{\text{uncorr}} = 9.3 \times 10^{-3}$
			Total:	$\delta A_{sys} = 9.4 \times 10^{-3}$

TABLE 5.15: Systematic Uncertainty in the 4th BigBite momentum bin.

LHRS data point				
Source	Corr / Uncorr	Uncertainty	Relative / Absolute	δA_{sys}^{source}
A_{π^-}	uncorr	0.0004	absolute	7.55×10^{-6}
A_{e^+}	uncorr	0.0099	absolute	2.1×10^{-4}
C_{π^-}	uncorr	100%	relative to C_{π^-}	2.4×10^{-4}
C_{e^+}	uncorr	100%	relative to C_{e^+}	1.24×10^{-3}
P_T	5%	corr	relative to P_T	3.4×10^{-4}
η_{N_2}	corr	0.029	absolute	2.32×10^{-4}
^{3}He$\rightarrow n$	corr	0.03	absolute	9.04×10^{-4}
A_{lumi}	uncorr	1.0×10^{-4}	absolute	1.0×10^{-4}
A_{LT}	uncorr	1.5×10^{-4}	absolute	1.5×10^{-4}
Rad. Corr.	corr	2.4%	relative to δA_y^{stat}	8.1×10^{-5}
			Correlated:	$\delta A_{sys}^{\text{corr}} = 9.9 \times 10^{-4}$
			Uncorrelated:	$\delta A_{sys}^{\text{uncorr}} = 1.3 \times 10^{-3}$
			Total:	$\delta A_{sys} = 1.31 \times 10^{-3}$

TABLE 5.16: Systematic Uncertainty in the LHRS

5.10 Target Single Spin Asymmetry Results

In this section, the target-normal single-spin asymmetries are presented. Shown first are the asymmetries of the contaminating particles, π^- and e^+. They are plotted versus momentum, as this is how they are incorporated into the final data. This is followed by electron asymmetries, which are plotted versus several kinematic variables. Plots include both BigBite and LHRS data. Because the LHRS is on the opposite side of the beam as BigBite, LHRS data has been multiplied by -1. All error bars represent statistical uncertainty. If systematic uncertainties are included, they are represented by boxes below the data.

Also shown are SSA's for transverse target. Here, transverse (denoted with an 'x' rather than 'y') indicates a target which is polarized perpendicular to beam momentum, but is still within the scattering plane defined by the incoming and outgoing electron. These results are interesting as a systematic check. Because the asymmetry is proportional to $\vec{S} \cdot \left(\vec{k} \times \vec{k}'\right)$, it is expected that $A_x = 0$.

5.10.1 Raw Electron Asymmetry

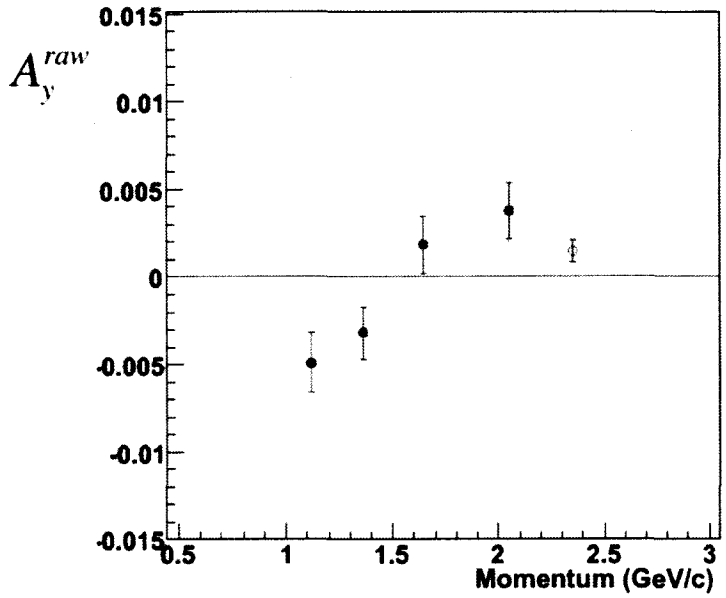

FIG. 5.19: Raw asymmetries for LHRS (open circle) and BigBite (closed circles).

BigBite		
p (GeV/c)	A_y^{raw}	δA_y^{raw}
1.12	-0.0049	0.0017
1.36	-0.0032	0.0015
1.64	0.0019	0.0016
2.05	0.0032	0.0016
LHRS		
2.35	-0.0015	0.0007

5.10.2 Negative Pion Asymmetry

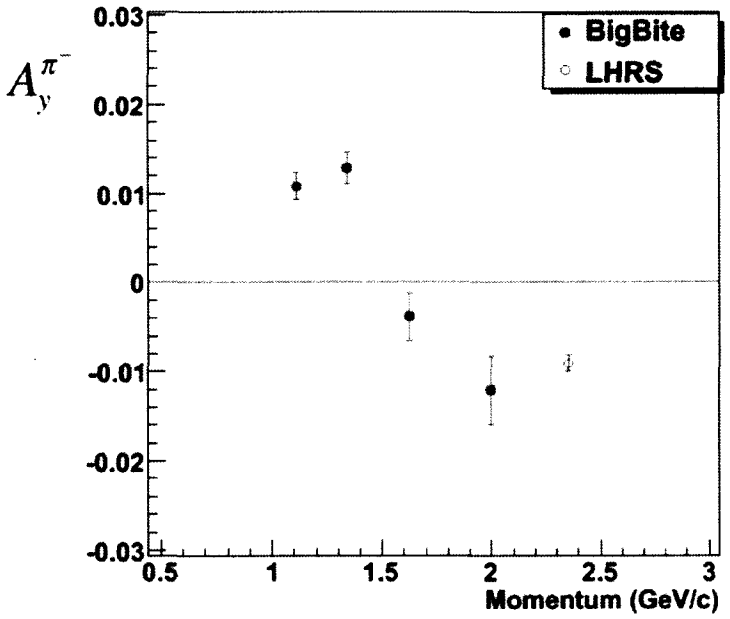

FIG. 5.20: Negative pion asymmetries for LHRS (open circle) and BigBite (closed circles).

BigBite		
p (GeV/c)	$A_y^{\pi^-}$	$\delta A_y^{\pi^-}$
1.12	0.0011	0.0015
1.36	0.0013	0.0018
1.64	-0.004	0.0027
2.05	-0.0121	0.0038
LHRS		
2.35	-0.0091	0.0005

5.10.3 Pair-Produced Electron Asymmetry

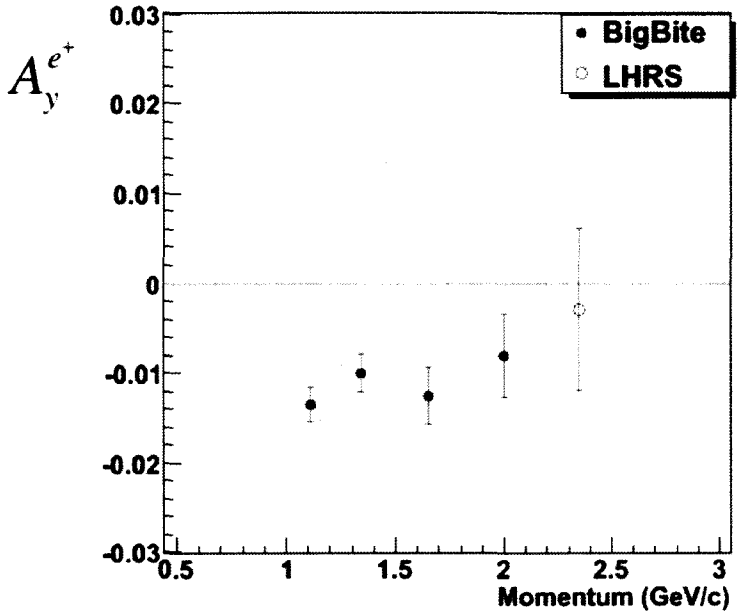

FIG. 5.21: Pair-produced e^- asymmetries for LHRS (open circle) and BigBite (closed circles).

BigBite		
p (GeV/c)	$A_y^{e^+}$	$\delta A_y^{e^+}$
1.12	-0.0135	0.0019
1.36	-0.0100	0.0021
1.64	-0.0125	0.0032
2.05	-0.0081	0.0047
LHRS		
2.35	-0.0029	0.0099

5.10.4 No-Track Events Asymmetry

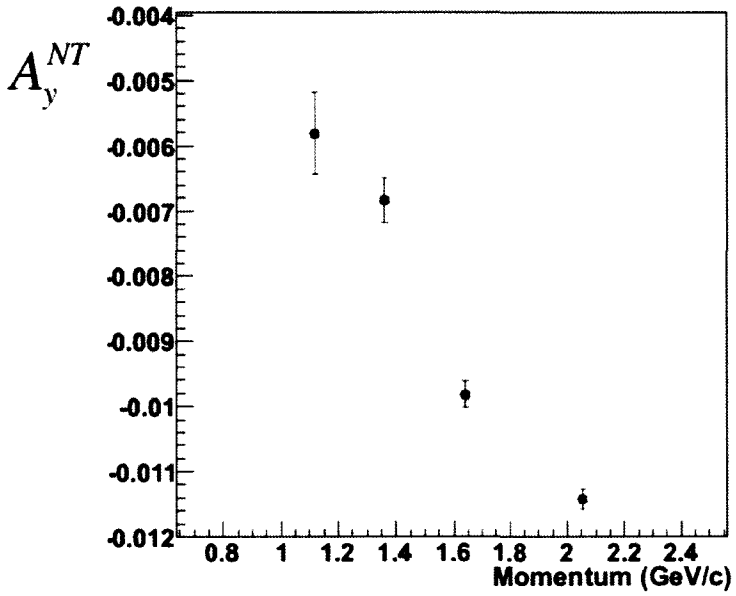

FIG. 5.22: Raw asymmetries for BigBite. The LHRS is not shown due to lack of statistics.

BigBite		
p (GeV/c)	A_y^{NT}	δA_y^{NT}
1.12	-0.0058	0.0007
1.36	-0.0068	0.0005
1.64	0.0097	0.0004
2.05	0.0114	0.0004

5.10.5 Electron Asymmetry

Target-Normal Data

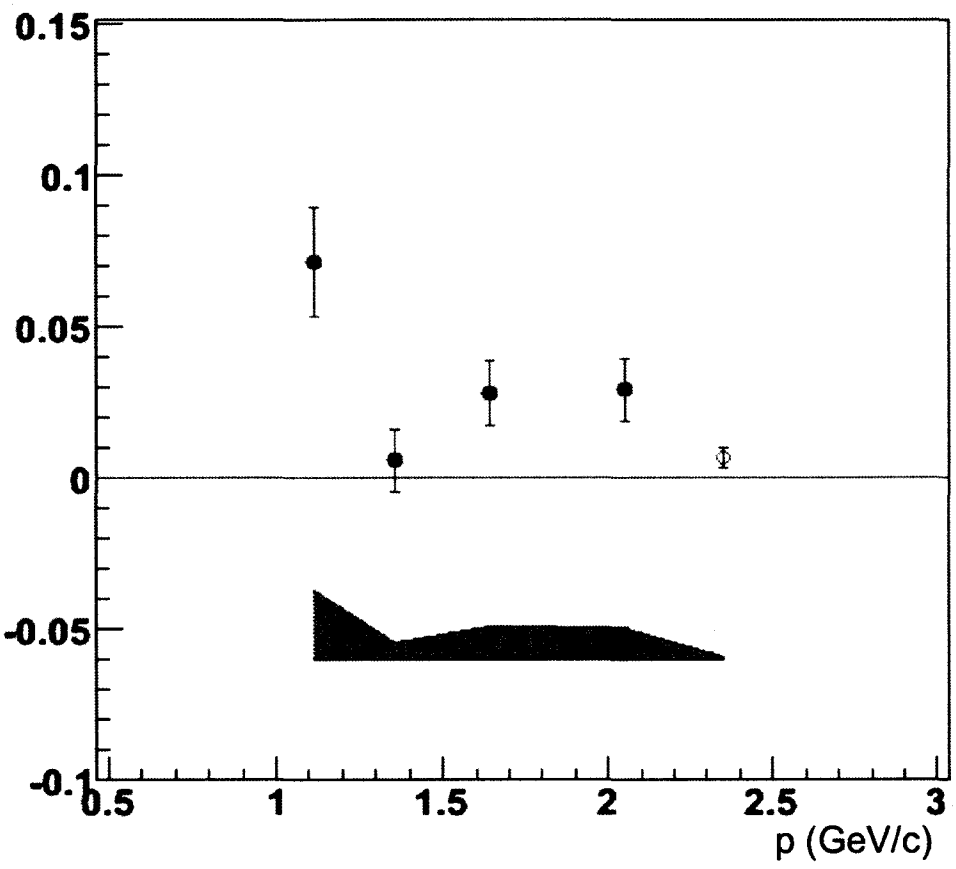

FIG. 5.23: A_y^n versus p. Closed (open) circles are data from BigBite (LHRS).

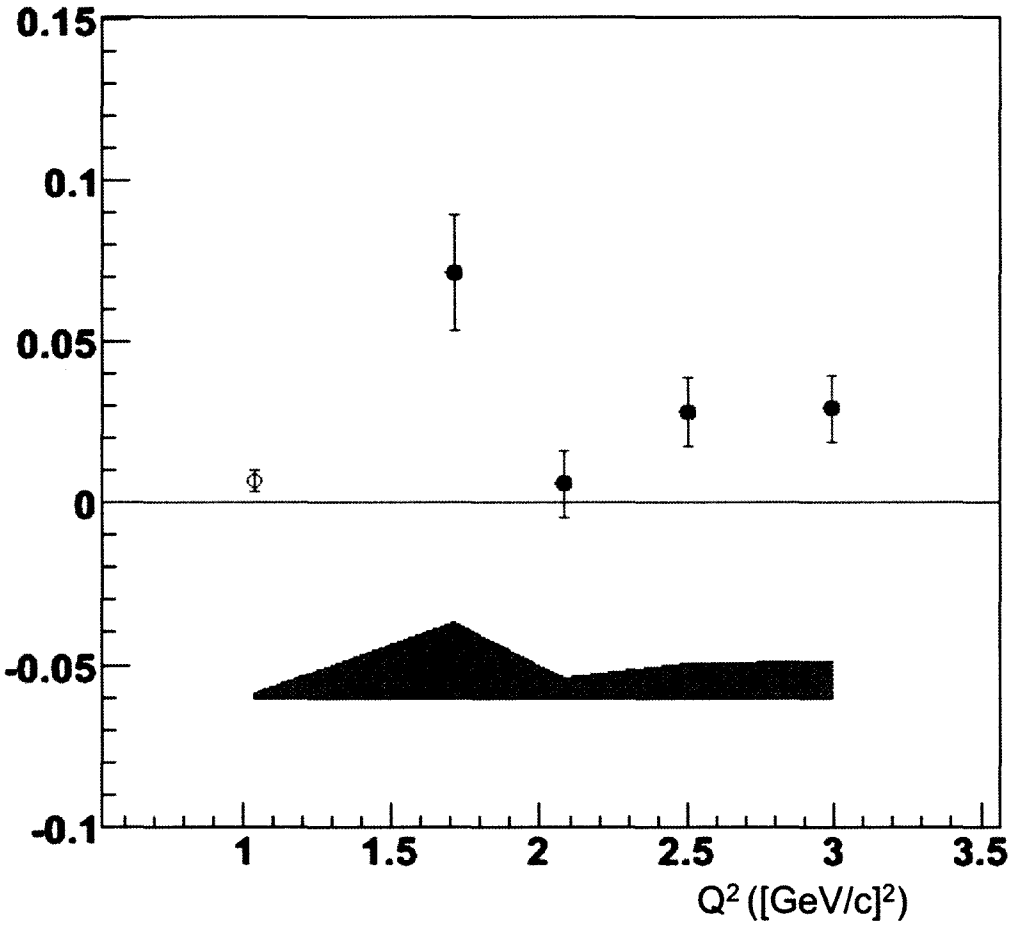

FIG. 5.24: A_y^n versus Q^2. Closed (open) circles are data from BigBite (LHRS).

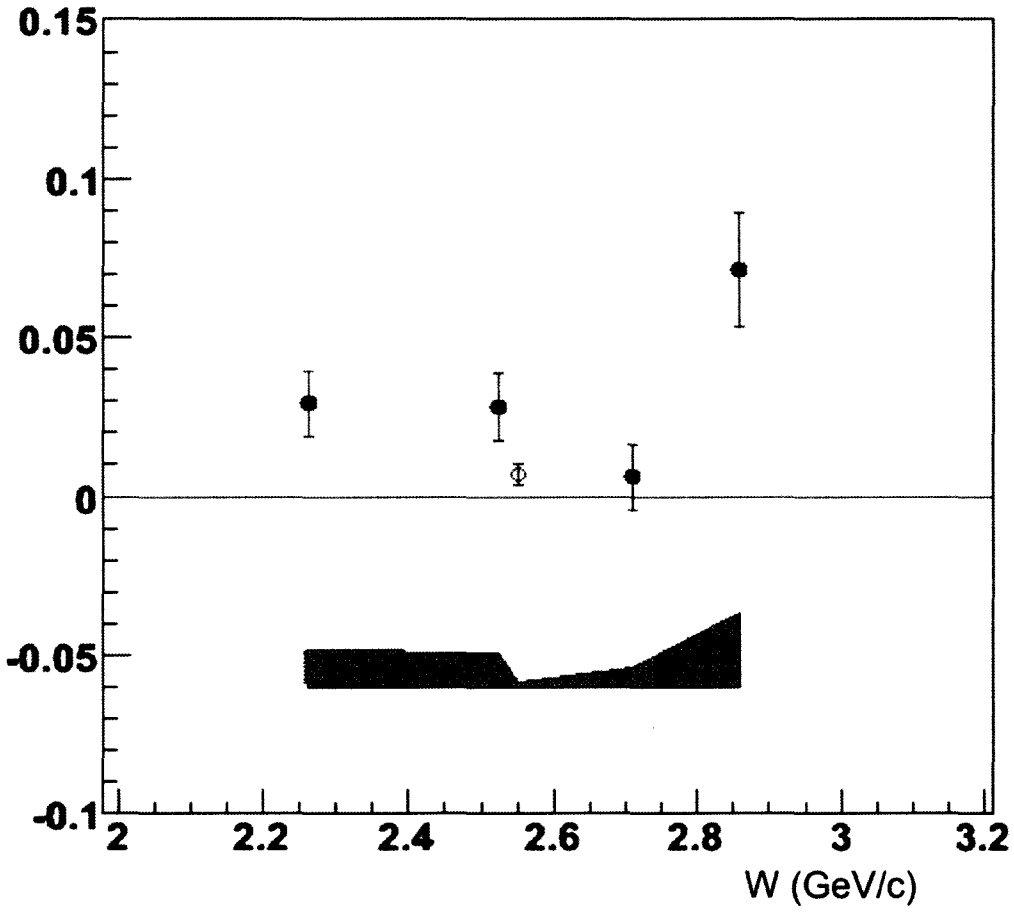

FIG. 5.25: A_y^n versus W. Closed (open) circles are data from BigBite (LHRS).

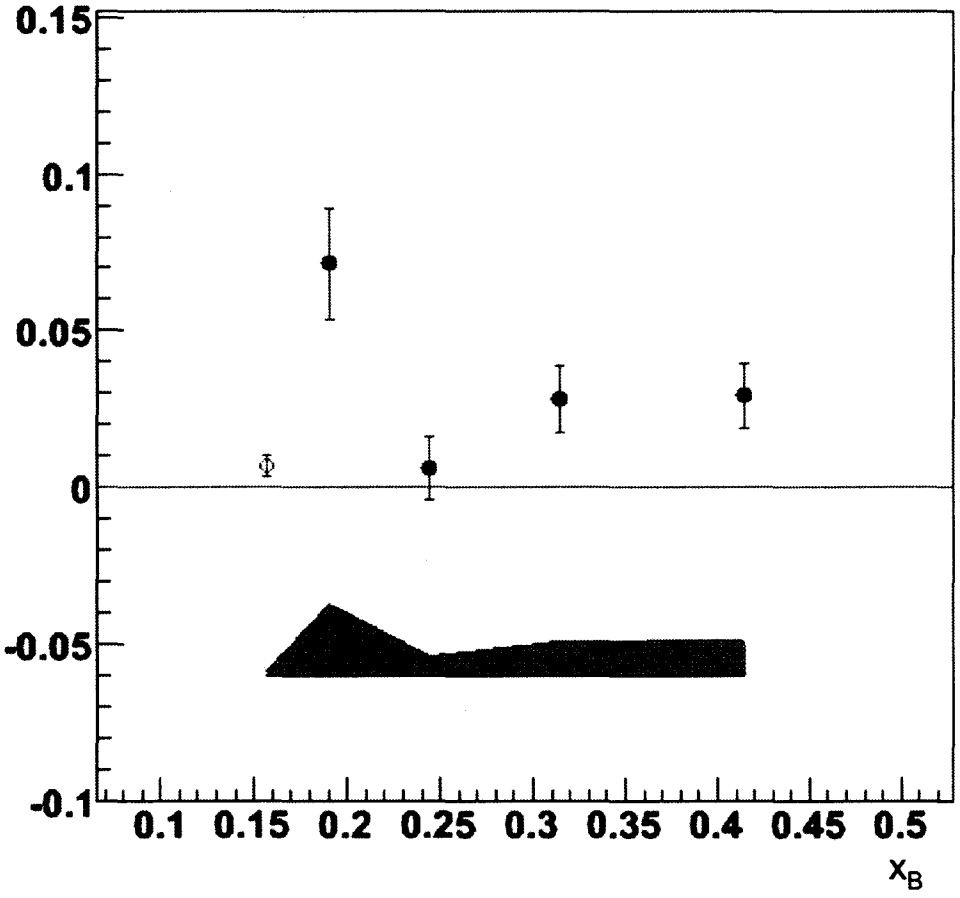

FIG. 5.26: A_y^n versus x_B. Closed (open) circles are data from BigBite (LHRS).

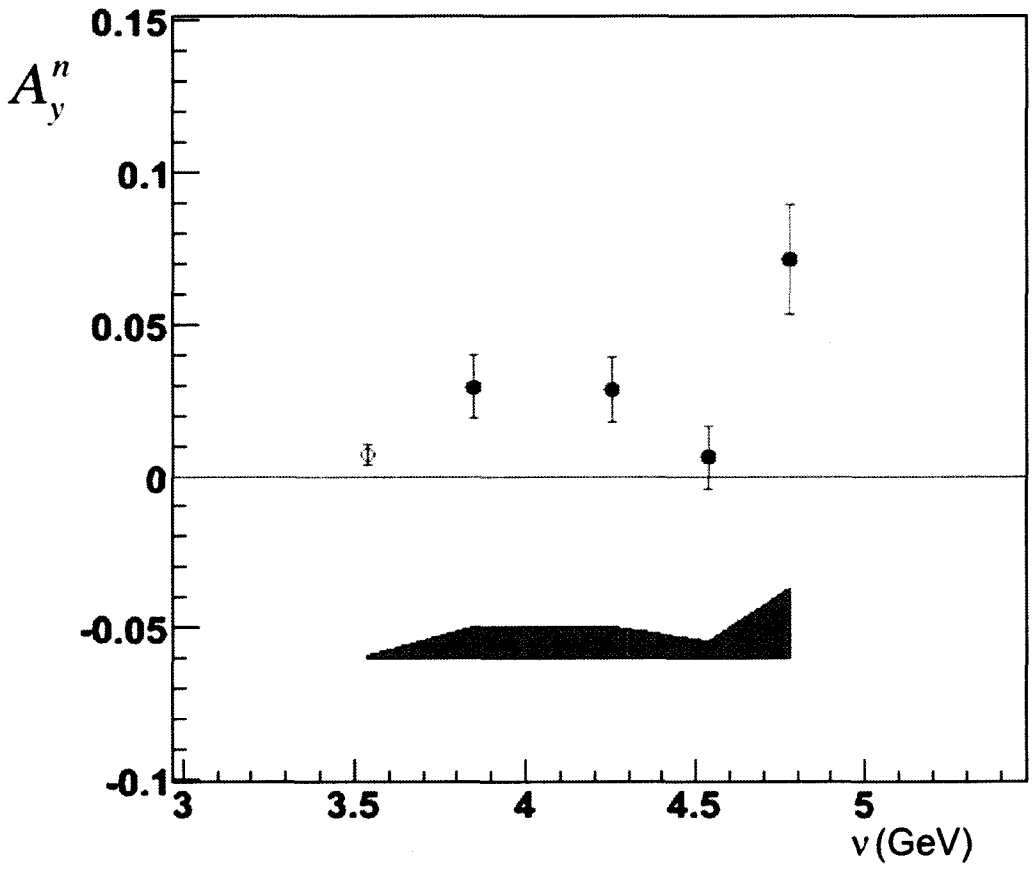

FIG. 5.27: A_y^n versus ν. Closed (open) circles are data from BigBite (LHRS).

BigBite								
p (GeV/c)	W (GeV)	ν (GeV)	θ	Q^2 (GeV/c)^2	x_b	A_y^n $(\times 10^{-2})$	δA_{stat} $(\times 10^{-2})$	δA_{sys} $(\times 10^{-2})$
1.12	2.86	4.77	30	1.71	0.191	7.14	1.79	2.30
1.36	2.71	4.35	30	2.08	0.244	0.61	1.03	0.53
1.64	2.52	4.25	30	2.50	0.314	2.84	1.06	0.92
2.05	2.26	3.84	30	2.99	0.413	2.93	1.05	0.94
LHRS								
2.35	2.55	3.54	15.9	1.04	0.157	0.68	0.34	0.13

TABLE 5.17: Summary of Final Target-Normal Single-Spin Asymmetry Results

Target-Transverse (in-plane) Data

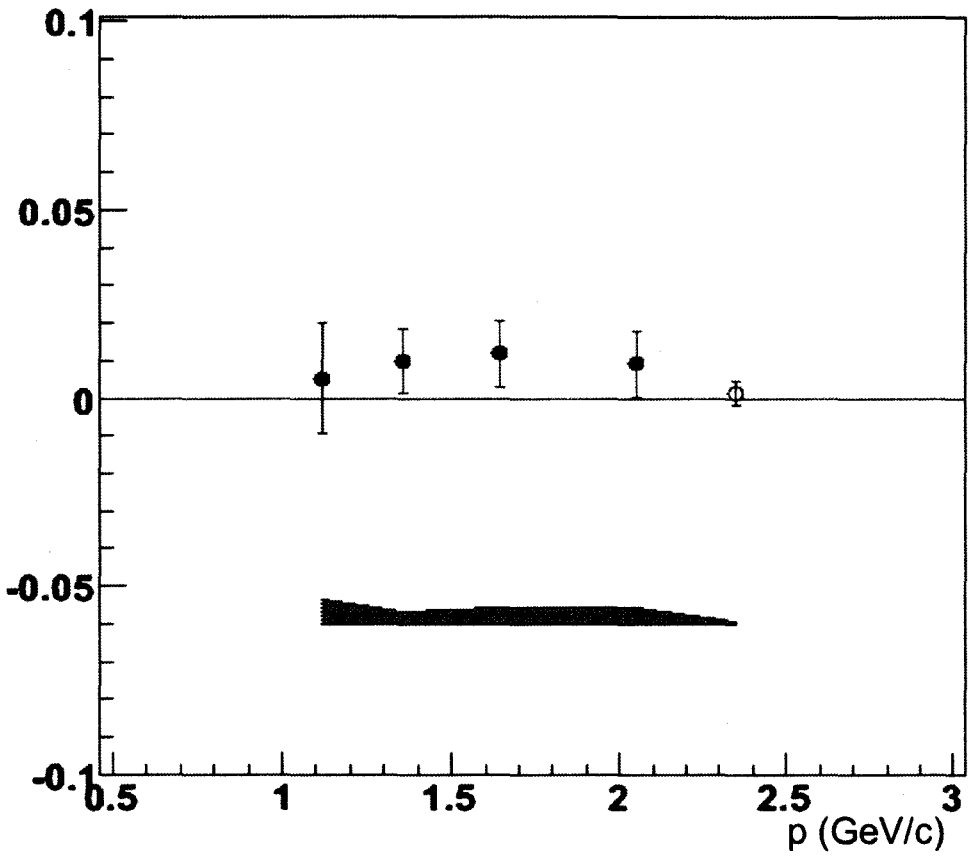

FIG. 5.28: A_x^n versus p.

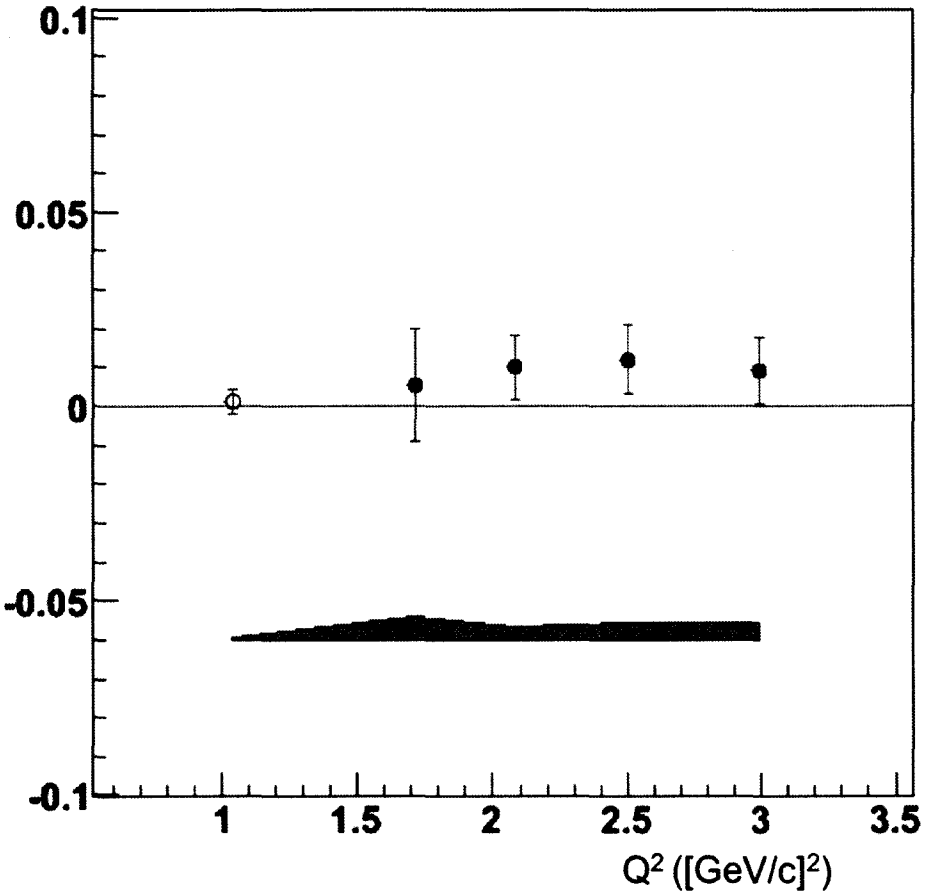

FIG. 5.29: A_x^n versus Q^2.

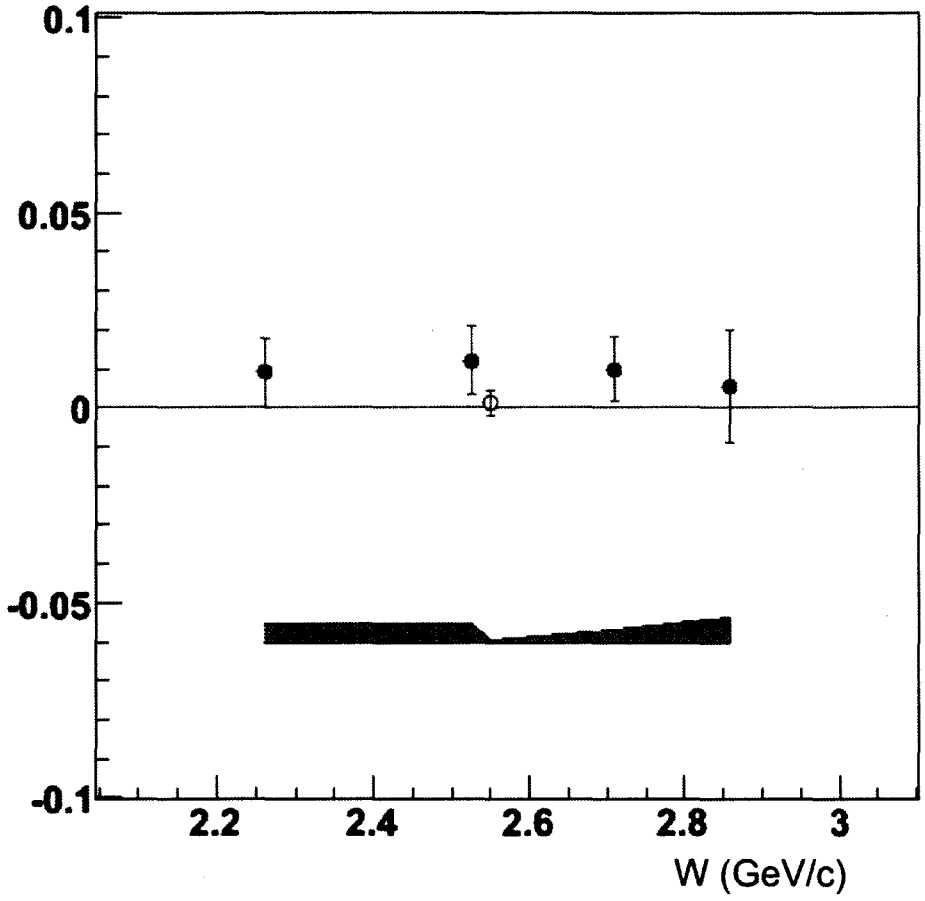

FIG. 5.30: A_x^n versus W.

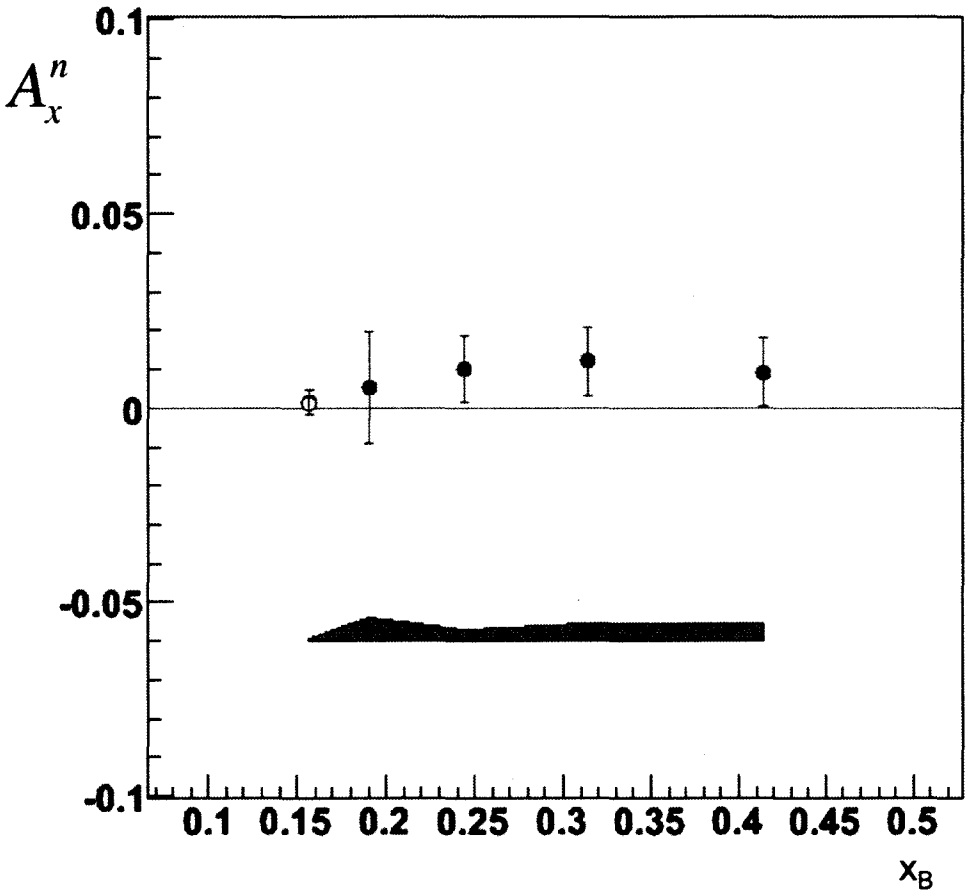

FIG. 5.31: A_x^n versus x_B.

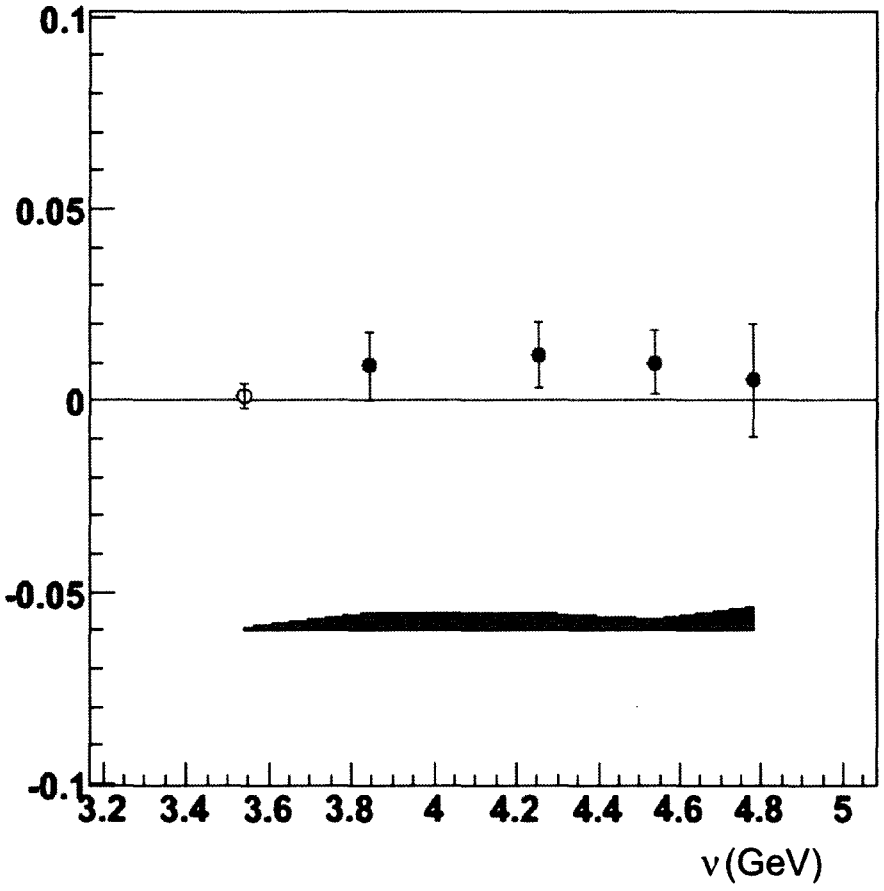

FIG. 5.32: A_x^n versus ν.

BigBite								
p (GeV/c)	W (GeV)	ν (GeV)	θ	Q^2 (GeV/c)^2	x_b	A_x^n ($\times 10^{-2}$)	δA_{stat} ($\times 10^{-2}$)	δA_{sys} ($\times 10^{-2}$)
1.12	2.86	4.77	30	1.71	0.191	0.53	1.5	0.61
1.36	2.71	4.35	30	2.08	0.244	1.00	0.85	0.29
1.64	2.52	4.25	30	2.50	0.314	1.19	0.88	0.42
2.05	2.26	3.84	30	2.99	0.413	0.91	0.88	0.43
LHRS								
2.35	2.55	3.54	15.9	1.04	0.157	0.13	0.32	0.05

TABLE 5.18: Summary of Final Target-Transverse, In-Plane Single-Spin Asymmetry Results

CHAPTER 6

Conclusion and Outlook

E07-013 has performed the first measurement of the target-normal single-spin asymmetry, A_y^n, in the deep inelastic region using a polarized neutron target. The overall uncertainty on the measurement is several times better than that of the previous SLAC proton data and an excellent complement to the recently acquired HERMES proton data. Further, this measurement significantly extends the kinematic range over which the target-normal SSA has been measured, with data points ranging between $0.19 < x_B < 0.41$ and $1.0 < Q^2 < 3.0$ (GeV/c)^2.

Data for A_y^n show an asymmetry ranging from 0.6 % to 7.0% which are on average 1.5 σ from zero. Transverse data, on the other hand, shows asymmetries ranging from 0.1% to 1.1% which are on average 0.7 σ from zero.

The systematic error on the BigBite data is larger than originally proposed, and dominated by issues with pair-produced electron contamination. However, the data point from the LHRS can be considered extremely clean, as it has less than 1% contamination from either pair-produced electrons and pions. This seems to strengthen the non-zero asym-

metry results seen in BigBite, as the LHRS shows a transverse data point that is easily consistent with zero, and a vertical data point that is 1.9σ from zero. Further, there is a sign change when comparing asymmetries in the LHRS and BigBite detectors.

It is a bit curious that the transverse data in the BigBite detector seems to show asymmetries that are consistently positive, having the same sign as the vertical data. This could be due to a large ϕ_S acceptance in the BigBite detector. Ideally, the entire detector would view the polarization vector as being at $90°$, i.e. normal to the scattering plane. However, the top and bottom of BigBite actually see the polarization as $90° \pm \delta\phi_S$. The distribution of ϕ_S is not symmetric about $90°$, and so this effect does not cancel out. Thus, it is possible that some vertical component could be enhancing our transverse signal. Further analysis could be carried out in which the vertical and transverse data are analyzed together, and binned by ϕ_S. One could then fit the A_{ϕ_S} to a sine wave. The amplitude of the fit would be interpreted as A_y^n.

The central values of A_y^n that are presented here are much larger than, and have the opposite sign of, the 10^{-4} prediction of Afanasev *et al.*, the only current prediction in the deep inelastic scattering region. For this reason, it is important to investigate possible culprits for the discrepency. The prediction is based on several assumptions. First, it is assumed that the transverse-spin dependent cross-section in DIS kinematics is well-described by a parton-like picture in which both the two-photon exchange couple to a single quark; the same quark that is hit with the interfering one-photon exchange process. Afanasev *et al.* admit that they "presently have no way of proving it...such as by way of formal twist-expansion in one-photon DIS" [26]. If one accepts the previous assumption, then there are two contributions to the cross-section which include a transverse spin-dependence. One involves conservation of the struck quark's helicity, the other a flip in helicity. The helicity-conserving contribution is of the order of $\langle k_T \rangle^2 / M_N$ multiplied by

the quark-helicity conserving transversely polarized twist-3 density, $g_{T,f}(x)$, with $\langle k_T \rangle^2$ being the transverse momentum of the quark and M_N the mass of the nucleon. The helicity-flip contribution's order is the constituent quark mass multiplied by the twist-2 quark transversity distribution, $\delta q_f(x)$. The comparison can then be made:

$$M_q \delta q_f(x) \leftrightarrow \frac{\langle k_T \rangle^2}{M_N} g_{T,f}(x) \tag{6.1}$$

where the left (right)-hand side is the helicity-flip (conserving) term. The $g_{T,f}$ term is proportional to both the longitudinally polarized twist-2 quark density, g_f and twist-3 quark-gluon correlations, the latter of which is deemed negligible. The authors conclude that the helicity-flip term dominates - a conclusion that is partially based on the constituent quark model, which assumes:

$$M_q \sim \frac{M_N}{3} \tag{6.2}$$

The further assumption that $\langle k_T \rangle^2 \ll M_q^2$ is also made, despite the fact that "in reality $|k_T| \sim$ a few 100 MeV i n the constituent quark model" [26]. One can easily see that a large quark-gluon correlation or transverse quark momentum could lead to a significant helicity-conserving contribution to the asymmetry. Moreover, the assumption in Equation 6.2 is only valid in the composite nucleon system where weak binding of the constituents is assumed. Thus, the author points out that Equation 6.2 should only be applied around $x \sim 0.3$.

The previous arguments against the 10^{-4} prediction are not intended to diminish the value of the predictive models laid forth by Afanasev *et al.*; rather it is simply to point out the lack of available rigorous theory that can be used to calculate a quantity such as A_y^n. To

date, appropriate models to estimate such an observable are widely speculative. Andreas Metz *et al.* [24] recently made an attempt to estimate A_y^n, but were unable to produce a quantitative result due to IR divergences. However, during a private communication with Metz, he indicated that an asymmetry on the order of 1% would not be surprising. This is simply due to the fact that $A_y^n \propto \frac{\alpha M_N}{Q^2}$. At the kinematics of E07-013, the $\frac{M_N}{Q^2}$ term does not give a strong suppression, and so the asymmetry can be expected to be on the order of α.

These data should serve as excellent motivation to propose further experiments to measure A_y^n. This should not be limited to the DIS region, as it is presently believed that the asymmetry in the quasi-elastic and resonance region could be much larger. Future experiments in the DIS region should especially focus on limiting pair-produced electron contamination. This could be as simple as using Hall A's HRS's to perform the measurement at high momentum, where the contamination is suppressed. One could also develop a more sophisticated trigger that is capable of measuring both electrons and positrons in coincidence such that photo-induced pairs could be tagged. The 12 GeV upgrade should serve as an excellent opportunity to extend the kinematic coverage of A_y^n even further. Combining further measurements with the present data, recent quasi-elastic data and HERMES data should begin to give a clear picture of the size of 2γ effects.

APPENDIX A

Proof of Equation 2.5

The full proof is given in reference [58].

Begin by defining T_{if} as the T-matrix element for the transition from initial state 'i' to final state 'f'. The relation between the S-matrix and T-matrix is defined as:

$$S = 1 + i(2\pi)^4\delta^4\left(\sum p_i - \sum p_f\right)$$

The unitarity condition is:

$$T_{if} - T_{if}^{\dagger} = i\mathcal{A}_{if}$$

with $\mathcal{A}_{if}$ being given as:

$$\mathcal{A}_{if} = \sum_{\Gamma} T_{i\Gamma}T_{\Gamma f}^{\dagger}(2\pi)^4\delta^4\left(\sum p_i - \sum p_{\Gamma}\right)$$

and the summation is extended to all possible on-shell intermediate states, Γ. The amplitude $\mathcal{A}_{if}$ is the *absorptive* (imaginary) part of the amplitude T_{if}.

Now, denote $\tilde{i}$ and $\tilde{f}$ as the initial and final states, but with spin and momenta reversed. Time-reversal invariance implies:

$$|T_{if}|^2 = |T_{\tilde{f}\,\tilde{i}}|^2$$

Define a T-odd effect as an observable which is proportional to the difference in probabilities:

$$|T_{if}|^2 - |T_{\tilde{i}\,\tilde{f}}|^2$$

When time-reversal invariance applies, the relation between T-odd effects and the absorptive part of the transition amplitude is:

$$|T_{if}|^2 - |T_{\tilde{i}\,\tilde{f}}|^2 = 2\mathcal{I}\left\{T_{if}\mathcal{A}_{fi}\right\} - |\mathcal{A}_{if}|^2 \tag{A.1}$$

Because the amplitudes are proportional to the small coupling constant, $\alpha = \frac{1}{137}$, equation A.1 can be expanded to various orders. The lowest order is:

$$|T_{if}|^2 - |T_{\tilde{i}\,\tilde{f}}|^2 = 0$$

meaning T-odd effects are non-existant. The next order is:

$$|T_{if}|^2 - |T_{\tilde{i}\,\tilde{f}}|^2 = 2\mathcal{I}\left\{T_{if}\mathcal{A}_{fi}\right\} \tag{A.2}$$

Here, T-odd effects have appears due to the interference of the Born approximation to the amplitude T_{if} and the lowest-order contribution to the absorptive amplitude $\mathcal{A}_{fi}$, which arises from 2γ exchange.

For a target single-spin asymmetry where the target is polarized normal to the scattering plane, the asymmetry is defined as:

$$A_y = \frac{N^{\uparrow} - N^{\downarrow}}{N^{\uparrow} + N^{\downarrow}}$$

and the number of events in each target state, $N^{\uparrow}$ and $N^{\downarrow}$, in terms of amplitudes are:

$$N^{\uparrow} \propto |T^{\uparrow}\left(\vec{k}, \vec{k}'\right)|^2 \equiv |T_{if}|^2$$

and

$$N^{\downarrow} \propto |T^{\downarrow}\left(\vec{k}, \vec{k}'\right)|^2$$

Now, the T-matrix describing the transition $\tilde{i} \rightarrow \tilde{f}$ is given as:

$$\left|T^{\downarrow}\left(-\vec{k}, -\vec{k}'\right)\right|^2 = |T_{\tilde{i}\ \tilde{f}}|^2$$

Because $T^{\downarrow}\left(-\vec{k}, -\vec{k}'\right)$ and $T^{\downarrow}\left(\vec{k}, \vec{k}'\right)$ are related, up to a phase, by a rotation of π around the $z - axis$, the asymmetry is proportional to $|T_{if}|^2 - |T_{\tilde{i}\ \tilde{f}}|^2$ and thus is a T-odd effect. Applying A.2, the asymmetry is given as:

$$A_y = \frac{2\mathcal{I}\left\{T_{if}\mathcal{A}_{fi}\right\}}{|T_{if}|^2} \tag{A.3}$$

APPENDIX B

Systematic Error on Transverse Data

BigBite Momentum Bin 1				
Source	Corr / Uncorr	Uncertainty	Relative / Absolute	δA_{sys}^{source}
A_{π^-}	uncorr	0.002	absolute	7.8×10^{-5}
A_{e^+}	uncorr	0.0028	absolute	5.8×10^{-3}
C_{π^-}	uncorr	100%	relative to C_{π^-}	3.38×10^{-4}
C_{e^+}	uncorr	20%	relative to C_{e^+}	1.5×10^{-3}
P_T	corr	5%	relative to P_T	2.7×10^{-4}
η_{N_2}	corr	0.03	absolute	5.9×10^{-5}
$^3\text{He} \rightarrow n$	corr	0.03	absolute	5.7×10^{-4}
A_{lumi}	uncorr	1.0×10^{-4}	absolute	1.0×10^{-4}
A_{LT}	uncorr	1.5×10^{-4}	absolute	1.5×10^{-4}
Rad. Corr.	corr	0.93%	relative to δA_y^{stat}	1.3×10^{-4}
			Correlated:	$\delta A_{sys}^{\text{corr}} = 8.2 \times 10^{-4}$
			Uncorrelated:	$\delta A_{sys}^{\text{uncorr}} = 6.0 \times 10^{-3}$
			Total:	$\delta A_{sys} = 6.1 \times 10^{-3}$

TABLE B.1: Systematic Uncertainty in the lowest BigBite momentum bin.

BigBite Momentum Bin 2				
Source	Corr / Uncorr	Uncertainty	Relative / Absolute	δA_{sys}^{source}
A_{π^-}	uncorr	0.0023	absolute	8.0×10^{-5}
A_{e^+}	uncorr	0.0032	absolute	2.0×10^{-3}
C_{π^-}	uncorr	100%	relative to C_{π^-}	3.5×10^{-4}
C_{e^+}	uncorr	58%	relative to C_{e^+}	1.58×10^{-3}
P_T	5%	corr	relative to P_T	5.0×10^{-4}
η_{N_2}	corr	0.011	absolute	1.23×10^{-4}
$^3\text{He} \rightarrow n$	uncorr	0.03	absolute	1.15×10^{-3}
A_{lumi}	uncorr	1.0×10^{-4}	absolute	1.0×10^{-4}
A_{LT}	uncorr	1.5×10^{-4}	absolute	1.5×10^{-4}
Rad. Corr.	corr	0.95%	relative to δA_y^{stat}	8.1×10^{-5}
			Correlated:	$\delta A_{sys}^{\text{corr}} = 1.3 \times 10^{-3}$
			Uncorrelated:	$\delta A_{sys}^{\text{uncorr}} = 2.6 \times 10^{-3}$
			Total:	$\delta A_{sys} = 2.9 \times 10^{-3}$

TABLE B.2: Systematic Uncertainty in the 2nd BigBite momentum bin.

BigBite Momentum Bin 3				
Source	Corr / Uncorr	Uncertainty	Relative / Absolute	δA_{sys}^{source}
A_{π^-}	uncorr	0.0034	absolute	8.0×10^{-5}
A_{e^+}	uncorr	0.0049	absolute	1.43×10^{-3}
C_{π^-}	uncorr	100%	relative to C_{π^-}	2.46×10^{-4}
C_{e^+}	uncorr	110%	relative to C_{e^+}	3.63×10^{-3}
P_T	corr	5%	relative to P_T	6.0×10^{-3}
η_{N_2}	corr	0.011	absolute	1.47×10^{-4}
^{3}He$\rightarrow n$	corr	0.03	absolute	1.56×10^{-3}
A_{lumi}	uncorr	1.0×10^{-4}	absolute	1.0×10^{-4}
A_{LT}	uncorr	1.5×10^{-4}	absolute	1.5×10^{-4}
Rad. Corr.	corr	0.42%	relative to δA_y^{stat}	3.7×10^{-5}
			Correlated:	$\delta A_{sys}^{\text{corr}} = 1.7 \times 10^{-3}$
			Uncorrelated:	$\delta A_{sys}^{\text{uncorr}} = 3.9 \times 10^{-3}$
			Total:	$\delta A_{sys} = 4.3 \times 10^{-3}$

TABLE B.3: Systematic Uncertainty in the 3rd BigBite momentum bin.

BigBite Momentum Bin 4				
Source	Corr / Uncorr	Uncertainty	Relative / Absolute	δA_{sys}^{source}
A_{π^-}	uncorr	0.0052	absolute	6.0×10^{-5}
A_{e^+}	uncorr	0.0067	absolute	7.35×10^{-4}
C_{π^-}	uncorr	100%	relative to C_{π^-}	1.16×10^{-4}
C_{e^+}	uncorr	350%	relative to C_{e^+}	4.0×10^{-3}
P_T	corr	5%	relative to P_T	4.55×10^{-4}
η_{N_2}	corr	0.011	absolute	1.1×10^{-4}
^{3}He$\rightarrow n$	corr	0.03	absolute	1.3×10^{-3}
A_{lumi}	uncorr	1.0×10^{-4}	absolute	1.0×10^{-4}
A_{LT}	uncorr	1.5×10^{-4}	absolute	1.5×10^{-4}
Rad. Corr.	corr	0.17%	relative to δA_y^{stat}	1.5×10^{-5}
			Correlated:	$\delta A_{sys}^{\text{corr}} = 1.4 \times 10^{-3}$
			Uncorrelated:	$\delta A_{sys}^{\text{uncorr}} = 4.0 \times 10^{-3}$
			Total:	$\delta A_{sys} = 4.2 \times 10^{-3}$

TABLE B.4: Systematic Uncertainty in the 4th BigBite momentum bin.

LHRS data point				
Source	Corr / Uncorr	Uncertainty	Relative / Absolute	δA_{sys}^{source}
A_{π^-}	uncorr	0.0004	absolute	7.56×10^{-6}
A_{e^+}	uncorr	0.01	absolute	1.9×10^{-4}
C_{π^-}	uncorr	100%	relative to C_{π^-}	5.5×10^{-5}
C_{e^+}	uncorr	100%	relative to C_{e^+}	3.9×10^{-4}
P_T	corr	5%	relative to P_T	6.5×10^{-5}
η_{N_2}	corr	0.029	absolute	4.4×10^{-5}
^{3}He$\rightarrow n$	corr	0.03	absolute	2.3×10^{-4}
A_{lumi}	uncorr	1.0×10^{-4}	absolute	1.0×10^{-4}
A_{LT}	uncorr	1.5×10^{-4}	absolute	1.5×10^{-4}
Rad. Corr.	corr	2.4%	relative to δA_y^{stat}	7.4×10^{-5}
			Correlated:	$\delta A_{sys}^{\text{corr}} = 2.5 \times 10^{-4}$
			Uncorrelated:	$\delta A_{sys}^{\text{uncorr}} = 4.7 \times 10^{-4}$
			Total:	$\delta A_{sys} = 5.3 \times 10^{-4}$

TABLE B.5: Systematic Uncertainty in the LHRS

BIBLIOGRAPHY

[1] F. Ernest Rutherford, Philosophical Magazine **21**, 669 (1911).

[2] F. J.J. Thomson, Philosophical Magazine **7**, 237 (1904).

[3] F. Ernest Rutherford, The London, Edinburgh and Dublin Philosophical Magazine and Journal of Science **37**, 581 (1919).

[4] F. James Chadwick, Proc. Roy. Soc. A **136**, 692 (1934).

[5] W. Heisenberg, Z. Phys. **77**, 1 (1932).

[6] D. Griffiths, *Introduction to Elementary Particles*, vol. 1 (John Wiley and Sons Inc, 1987).

[7] F. Halzen and A. Martin, *Quarks and Leptons: An Introductory Course in Modern Particle Physics* (John Wiley and Sons Inc, 1984), 1st ed.

[8] K. Slifer, Ph.D. thesis, Temple University (2004).

[9] X. Zheng, Ph.D. thesis, Massachusetts Institute of Technology (2002).

[10] K. G. Wilson, Phys. Rev. **179**, 1499 (1969).

[11] K. Allada, Ph.D. thesis, University of Kentucky (2010).

[12] C. Dutta, Ph.D. thesis, University of Kentucky (2010).

[13] C. E. Carlson and M. Vanderhaeghen, Annual Review of Nuclear and Particle Science **57**, 171 (2007).

[14] P. G. Blunden, W. Melnitchouk, and J. A. Tjon, Phys. Rev. Lett. **91**, 142304 (2003).

[15] P. Guichon and M. Vanderhaegen, Phys. Rev. Lett. **91** (2003).

[16] P. Guichon, European Physics Journal A **24**, 23 (2005).

[17] A. Kelleher, Ph.D. thesis, College of William and Mary (2009).

[18] J. Arrington, Phys. Rev. C **68**, 034325 (2003).

[19] R. C. Walker et al., Phys. Rev. **D49**, 5671 (1994).

[20] M. K. Jones et al., Phys. Rev. Lett. **84**, 1398 (2000).

[21] O. Gayou, K. A. Aniol, T. Averett, F. Benmokhtar, W. Bertozzi, L. Bimbot, E. J. Brash, J. R. Calarco, C. Cavata, Z. Chai, et al., Phys. Rev. Lett. **88**, 092301 (2002).

[22] N. Christ and T. D. Lee, Phys. Rev. **143**, 1310 (1966).

[23] M. Kobayashi and T. Maskawa, Progress of Theoretical Physics **49**, 652 (1973).

[24] A. Metz, M. Schlegel, and K. Goeke, Phys. Lett. B **643**, 319 (2006), ISSN 0370-2693.

[25] R. N. Cahn and Y. S. Tsai, Phys. Rev. D **2**, 870 (1970).

[26] A. Afanasev, M. Strikman, and C. Weiss, Phys. Rev. D **77**, 014028 (2008).

[27] J. R. Chen, J. Sanderson, J. A. Appel, G. Gladding, M. Goitein, K. Hanson, D. C. Imrie, T. Kirk, R. Madaras, R. V. Pound, et al., Phys. Rev. Lett. **21**, 1279 (1968).

[28] S. Rock, M. Borghini, O. Chamberlain, R. Z. Fuzesy, C. C. Morehouse, T. Powell, G. Shapiro, H. Weisberg, R. L. A. Cottrell, J. Litt, et al., Phys. Rev. Lett. **24**, 748 (1970).

[29] e. a. A. Airapetian, arXiv:0907.5369v3 (2009).

[30] T. M. R. Prepost, Ann. Rev. of Nucl. and Part. Sci. **45** (1995).

[31] M. Romalis, Ph.D. thesis, Princeton University (1997).

[32] T. H. A. Collaboration, *JLab Hall A General Operations Manual* (2005).

[33] D. J. J. de Lange, J. J. M. Steijger, H. de Vries, M. Anghinolfi, M. Taiuti, D. W. Higinbotham, B. E. Norum, and E. Konstantinov, Nuclear Instruments and Methods in Physics Research Section A: Accelerators, Spectrometers, Detectors and Associated Equipment **406**, 182 (1998), ISSN 0168-9002.

[34] X. Qian, Ph.D. thesis, Duke University (2010).

[35] K. Schreckenbach and W. Mampe, Journal of Physics G: Nuclear and Particle Physics **18**, 1 (1992).

[36] C. Ciofi degli Atti, S. Scopetta, E. Pace, and G. Salmè, Phys. Rev. C **48**, R968 (1993).

[37] J. L. Friar, B. F. Gibson, G. L. Payne, A. M. Bernstein, and T. E. Chupp, Phys. Rev. C **42**, 2310 (1990).

[38] F. D. Colegrove, L. D. Schearer, and G. K. Walters, Phys. Rev. **132**, 2561 (1963).

[39] K. Suchanek, Optica Applicata **XXXV**, 1 (2005).

[40] T. G. Walker, Phys. Rev. A **40**, 4959 (1989).

[41] A. Deur, Ph.D. thesis, Universite Blaise Pascal (2000).

[42] V. Sulkosky, Ph.D. thesis, College of William and Mary (2007).

[43] E. Babcock, B. Chann, T. G. Walker, W. C. Chen, and T. R. Gentile, Phys. Rev. Lett. **96**, 083003 (2006).

[44] E. Babcock, I. Nelson, S. Kadlecek, B. Driehuys, L. W. Anderson, F. W. Hersman, and T. G. Walker, Phys. Rev. Lett. **91**, 123003 (2003).

[45] W. C. Chen, T. R. Gentile, T. G. Walker, and E. Babcock, Phys. Rev. A **75**, 013416 (2007).

[46] B. Chann, E. Babcock, L. W. Anderson, and T. G. Walker, Phys. Rev. A **66**, 032703 (2002).

[47] E. Babcock, Ph.D. thesis, University of Wisconsin, Madison (2005).

[48] J. Singh, Ph.D. thesis, University of Virginia (2010).

[49] P. Solvignon, Ph.D. thesis, Temple University (2006).

[50] K. M. Kramer, Ph.D. thesis, College of William and Mary (2003).

[51] M. V. Romalis, E. Miron, and G. D. Cates, Phys. Rev. A **56**, 4569 (1997).

[52] A. Abragam, *Principles of Nuclear Magnetism* (Oxford University Press, 1961).

[53] F. Bloch and A. Siegert, Phys. Rev. **57**, 522 (1940).

[54] M. V. Romalis and G. D. Cates, Phys. Rev. A **58**, 3004 (1998).

[55] E. Babcock, I. A. Nelson, S. Kadlecek, and T. G. Walker, Phys. Rev. A **71**, 013414 (2005).

[56] M. V. Romalis and G. D. Cates, Phys. Rev. A **58**, 3004 (1998).

[57] L. W. MO and Y. S. TSAI, Rev. Mod. Phys. **41**, 205 (1969).

[58] E. D. R. A. De Rujula, J. M. Kaplan, Nuclear Physics B **35** (1971).

VITA

Joseph Katich

Joseph Katich was born on March 7, 1981 in New Castle, PA. He graduated from Mohawk Area High School, in Bessemer, PA, in June of 1999. The following academic year he enrolled in Westminster College in New Wilmington, PA where he majored in Physics and minored in Mathematics. He received his B.S. degree in May of 2003. In the fall of 2003 he entered the graduate program in Physics at the College of William and Mary in Williamsburg, VA. He received his M.S. in December 2004, shortly after joining the Hadronic Physics Group. Working under the advisement of Professor Todd D. Averett, Joe performed most of his thesis work at Jefferson Laboratory in Newport News, VA. He defended his thesis on September 3rd, 2010. He is now working for the University of Colorado in Boulder, CO as a Post-doctoral Associate.